

# **Model-based Analysis of an Electro-Enzymatic System for Glucose Oxidation**

Dissertation  
For the award of the degree

**Doktoringenieur  
(Dr.-Ing.)**

by M.Sc. Nga Thi Quynh Do

date of birth 17. September 1985  
in Quang Ngai, Viet Nam

acceptedd by the Faculty of Process and Systems Engineering of the Otto-von-Guericke University of Magdeburg

Reviewer: Prof. Dr.-Ing. Kai Sundmacher  
Prof. Dr.-Ing. Ulrike Krewer  
Prof. Dr. Mihai Christov

Head of the Colloquium: Prof. Dr. rer. nat. habil. Helmut Weiß

Submitted on 01. 03 2017  
Graduation Colloquium on: 16. 06 2017

# Declaration

I hereby declare that I prepared the work submitted without inadmissible assistance and without the use of any aids other than those indicated. Fact or ideas taken from other sources, either directly or indirectly have been marked as such.

In particular, I did not use the services of a commercial graduation consultation. Further, I have not made payments to third parties either directly or indirectly for any work connected with the contents of the submitted dissertation.

The work has not so far submitted either in Germany or abroad in same or similar form as a dissertation and has also not yet been published as a whole.

**Magdeburg, 29. June 2017**

A handwritten signature in black ink, appearing to read 'Nga, Thi Quynh, Do', with a long horizontal line extending to the right.

**Nga, Thi Quynh, Do**

# Zusammenfassung

Elektro-enzymatische Systeme (EES) können Bestandteile nachhaltiger Prozesse für die nächste Generation der Biotransformation und der Energieerzeugung sein. Derzeitige Grenzen eines EES werden durch die niedrige Leistung und kurze Lebensdauer gesetzt. Die in der Literatur genannten Ansätze, diese Schwachstellen zu beheben, beziehen sich im Wesentlichen auf experimentelle Arbeiten. Diese Beschränkung auf Verbesserungen im experimentellen Bereich hat die vorliegende Arbeit dahingehend motiviert, auch die Aspekte einer mathematischen Modellierung zu untersuchen. Diese Dissertation verfolgt zwei wesentliche Ziele. Das erste Ziel ist die Bestimmung der Reaktionsmechanismen von ausgewählten EES mit verlässlichen kinetischen Parametern, die anschließend an andere, entsprechende Systeme angekoppelt werden können. Das zweite Ziel ist die vollständige Prozessanalyse von EES.

Dynamische Modelle und stationäre Modelle auf der Makroskala wurden formuliert, um das Verhalten von EES zu interpretieren. Die Modellierungsdomäne wächst von einem Grenzflächenmodell (Elektrochemische Impedanzspektroskopie (EIS), Dünnschicht) zu einem örtlich verteilten Modell (mit Katalysatorschicht (CL) und Diffusionsschicht (DL)). Bei der Formulierung mathematischer Modelle enzymatischer Elektroden wurden zeitlich und räumlich veränderliche Stoff- und Ladungsbilanzen mit Transportgesetzen und mehrstufigen Reaktionskinetiken kombiniert. Diese Modelle basieren auf PDE, ODE, DAE und AE Gleichungssystemen. Sie wurden analytisch oder numerisch gelöst.

Für die Anode wurde das ortsverteilte Modell entwickelt, um das Verhalten von mit dem Enzym Glukose Oxidase (GOx) und dem Mediator tetrathiafulvalene (TTF) modifizierten porösen Elektroden zu beschreiben. Das ortsverteilte Modell wurde experimentell kalibriert mit Hilfe der PVDF-Prozedur parametrisiert. Es konnte gezeigt werden, dass das ortsverteilte Modell notwendig ist, um den Enzymatischen porösen Elektroden (EPE) quantitativ und qualitativ zu beschreiben. Anschließend wurde das Modell erfolgreich benutzt, um poröse GOx-Elektroden mit der Gelatine-Prozedur zu untersuchen.

Für die Kathode wurde die Meerrettichperoxidase (HRP) als Modellenzym ausgewählt. Die Reaktionskinetiken und die Parametrisierung des katalytischen Zyklus der HRP auf einer elektrisch leitenden Oberfläche wurden zuerst auf einer Dünnschichtelektrode ausgeführt. Es wurden drei mechanistische Modelle vorgeschlagen und mittels stationärer Modellansätze- und EIS- Analyse diskriminiert. Der EIS-Ansatz erwies sich als sensitiver für die Modellunterscheidung. Daher wurde das beste Modell ausgewählt, weiter parametrisiert und in das entsprechende ortsverteilte Modell eingefügt. Das letztgenannte Modell wurde ausgebaut, um das Verhalten der porösen Elektroden anhand der HRP und der enzymatischen Kaskade GOx-HRP zu untersuchen. Die Erweiterung des Grenzflächen- zum ortsverteilten Modell machte die Bestimmung zusätzlicher Strukturparameter möglich. Für die enzymatische Kaskade an der porösen Elektrode wurden die individuellen Parameter der GOx und des HRP-Systems verwendet.

Im Allgemeinen konnte die Bedeutung einer ortsverteilten Systembeschreibung für die Untersuchung des Verhaltens von EPE gezeigt werden. Es stellte sich heraus, dass der Stofftransport im CL für bestimmte Spezies wie z.B. Glukose,  $H_2O_2$  and  $O_2$  beschränkt ist. Die Korrelation des Konzentrationsprofils mit dem angelegten Potenzial ist entscheidend für die poröse GOx-Elektrode. Der Ausnutzungsgrad des aktiven Katalysators und des Mediators ist niedrig und sollte zukünftig verbessert werden. Die Immobilisierungsstrategie für die Enzyme kann jede Art von Elektronentransfer unterschiedlich beeinflussen. Darüber hinaus kann die Verschiebung des Anfangspotenzials aufgrund von Konzentrationsänderungen des aktiven Enzyms

und des Mediators sowohl in DET als auch in MET beobachtet werden. Die Beschränkung des Stofftransportes hinsichtlich des Substrates in CL kann durch die Verwendung alternativer Materialstrukturen verbessert werden, z.B. im Fall der porösen GOx-HRP-Elektrode.

## Abstract

Electro-enzymatic systems (EESs) can be considered as sustainable processes for the next biotransformation and energy generation due to the excellence of enzymes as biocatalysts. The main bottlenecks of EESs are low performance, and a short lifetime. To date, improvement efforts in the literature have been predominated in the experimental part. This has motivated the current work on the mathematical modelling aspect. The work had been focused on two main aims. The first is to determine adequate reaction mechanisms of selected EESs with reliable kinetic parameters which can be subsequently plugged into the other respective systems. The latter one is a comprehensive process analysis of the EESs for further improvement.

Dynamic and steady state macroscale models were formulated. The modelling domain increases from the interface models (electrochemical impedance spectroscopy (EIS), thin film) to the distributed model (with catalyst layer (CL) and diffusion layer (DL)). In the mathematical models of enzymatic electrodes, mass and charge balances changing over space/time were combined with transport laws and multi-step reaction kinetics. These models consist of PDEs, ODEs, DAEs and AEs which were solved analytically or numerically.

For the anode side, the distributed model was developed to describe the behaviour of the modified porous electrode using enzyme glucose oxidase (GOx) and mediator tetrathiafulvalene (TTF). The distributed model was calibrated experimentally and parameterized by using the PVDF procedure. It was proved the necessity of the distributed model in describing quantitatively and qualitatively the behaviour of the studied enzymatic porous electrode (EPE). The model was then applied effectively to study the porous GOx electrode using the Gelatin procedure.

Enzyme horseradish peroxidase (HRP) was chosen as a model enzyme in the cathode. The reaction kinetics and parameterization of the HRP catalytic cycle on a conductive surface were first performed on a thin film electrode. Three mechanistic models were proposed and discriminated using the steady state and EIS methodologies. The EIS approach proved to be more sensitive for models discrimination. Thus, the best kinetic model was selected, further parameterized and inserted into the respective distributed model. The distributed model was extended to investigate the behaviour of the porous electrode using HRP and the enzymatic cascade GOx-HRP. When upgrading the interface to the distributed model, structural parameters were additionally obtained by optimization. For the porous enzymatic cascade electrode, the individual parameters from the GOx and HRP systems were used.

In general, the distributed model demonstrated its importance in investigating the behaviour of the EPEs. It revealed the mass transport limitation inside the CL of different chemical species, i.e. glucose,  $\text{H}_2\text{O}_2$  and  $\text{O}_2$ . The correlation of concentration profile and applied potential is significant in the GOx porous electrode. The active catalyst and mediator utilization need to be improved. The immobilization strategies can disturb each type of electron transfer differently. In addition, the shift of onset potential can be seen in both DET and MET due to the change of active enzyme and mediator concentrations, respectively. The mass transport limitation of substrate in CL can be improved by using different supplying substance scenarios, i.e. in the case of porous GOx-HRP electrode.

# Acknowledgement

The work, presented in the dissertation, was performed during my PhD course within the framework of the International Max Planck Research School for Advanced Methods in Process and Systems Engineering (IMPRS ProEng), Magdeburg and in the Process System Engineering Department at Max Planck Institute Magdeburg from 15.11.2010 to 31.3.2016.

I would like to express my heartfelt gratitude to Prof. Kai Sundmacher who gave me an opportunity to pursue my PhD in his chair on a very interesting topic. I am grateful for his support, professional guidance, demanding and the fruitful discussions in PAC/PhD meetings along the PhD course which help me to be more targeted and grow up in an academic environment.

I would like to acknowledge the IMPRS ProEng Magdeburg, the Otto-von-Guericke University-Magdeburg and the Center for Dynamic Systems financed by the Federal State Saxony-Anhalt in Germany for financial support.

Specially, I would like to thank Dr. Tanja Vidaković-Koch for her detail guidance, patience, scientific discussions, and article/dissertation correction/suggestions, without her valuable help this work wouldn't be completed.

I acknowledge the great collaboration of Prof. Hanke Rauschenbach on porous electrode modelling following with the fruitful discussions and pragmatic advices. I also thank you Dr. Robert Flässig for the collaboration on the parameter optimization part. I thank you my colleagues Dr. Ivan Ivanov, Ms. Miroslava Varničić for providing me experimental data/ useful discussions to validate the mathematical model. I thank Bianka Stein for sending samples for SEM and her great support in the lab.

This work has also benefited from contributions of several students who worked as a research assistant i.e. Das Tamal, Xiaoci Hu, Nhut Minh Nguyen, Aditya Bhattacharjee, Arutha Paul or performed a master thesis Siva Rama Krishna Gullapalli under my supervisions. It was a pleasure to work with all of you.

I thank my colleagues and friends from my lovely office, the PSE group, the university, MPI, Vietnamese friends for sharing great time on variety of interesting/joyful discussions. I thank you Dr. Barbara Witter, Dr. Jürgen Koch, Mrs. Stephanie Geyer and administration team for great support regarding to the paper work, family care and support.

I thank Prof. Helmut Weiß for acting as head of the Commission for the Ph.D defense colloquium. I thank the professors taking part as the peer reviewers of this work.

At this point, I would like to enormously thank my big family for the never ending support and being understanding/together of all the time. I would like to thank my life partner for his love, sharing, understanding, and encouraging me pursuing the PhD and the academia career. To my dearest Anh Thy and Hong Anh, I am so blessed to have you in my life so that I have the greatest motivation for everything.

Con cảm ơn ba má, anh chị em và gia đình đã nuôi nấng, luôn ủng hộ, đồng hành và chia sẻ trong các chặng đường con đã đi. Em cảm ơn anh đã cùng em chia sẻ những niềm vui cũng như nỗi buồn, luôn động viên và cho em cái nhìn tích cực trong cuộc sống. Cảm ơn hai con Hồng Anh, Anh Thy đã đến bên đời mẹ và là nguồn động lực lớn để mẹ luôn cố gắng.

Nga Thi Quynh Do

# Table of content

Declaration .....	
Zusammenfassung.....	
Abstract .....	
Acknowledgement .....	
Table of content .....	i
List of symbols.....	iv
<b>1 Introduction .....</b>	<b>1</b>
1.1 Motivation .....	1
1.2 Aims of the study .....	6
1.3 The dissertation structure .....	7
<b>2 State of the art .....</b>	<b>9</b>
2.1 Enzymes in electrochemical processes .....	9
2.1.1 Enzymes as biocatalysts.....	9
2.1.2 Enzymes as an electron donor/acceptor on a conductive surface .....	10
2.1.3 How are enzymes embedded into electro-enzymatic electrodes?.....	12
2.1.4 Application of enzymatic electrodes .....	13
2.2 Mathematical modelling of a porous electrode .....	15
2.2.1 Catalyst layer physical structure.....	16
2.2.2 Governing equations .....	17
2.2.2.1 Potential field-charge balance .....	17
2.2.2.2 Mass balances .....	19
2.2.2.3 Reduced 1-D model.....	20
2.3 Application of the distributed model into an electro-enzymatic system .....	20
2.4 Finite volume method for partial differential equation.....	22
2.5 Electrochemical impedance spectroscopy.....	26
2.6 Model discrimination (model calibration) and parameterization .....	31
<b>3 Mathematical modelling.....</b>	<b>33</b>
3.1 Modelling domains and physical phenomena .....	33
3.2 Facts and main assumptions .....	34

3.3	Enzymatic anode .....	35
3.3.1	Potential field- charge balance.....	37
3.3.2	A single substrate .....	37
3.3.3	Competitive substrates.....	40
3.4	Enzymatic cathode .....	43
3.4.1	Interface model .....	46
3.4.1.1	Mass balance equations.....	46
3.4.1.2	Electrochemical impedance spectroscopy derivation .....	47
3.4.2	Porous electrode with HRP.....	48
3.4.3	Porous electrode with an enzymatic cascade .....	49
<b>4</b>	<b>Experimental validation .....</b>	<b>53</b>
4.1	Materials .....	53
4.2	Electrode preparation .....	53
4.2.1	Enzymatic anode.....	53
4.2.2	Enzymatic cathode.....	55
4.2.2.1	Thin film electrode preparation .....	55
4.2.2.2	Porous electrode with single enzyme .....	55
4.2.2.3	Porous electrode with enzymatic cascade.....	56
4.3	Measurements .....	56
4.3.1	Enzymatic anode.....	57
4.3.2	Cathode.....	57
4.3.2.1	Thin film electrode .....	57
4.3.2.2	Porous electrode .....	57
4.3.3	Scanning electron microscopy.....	57
<b>5</b>	<b>Results and discussion .....</b>	<b>58</b>
5.1	Model parameters.....	58
5.2	Enzymatic anode .....	59
5.2.1	Porous electrode with a single substrate .....	60
5.2.1.1	PVDF porous electrode .....	60
5.2.1.1.1	Steady state polarization .....	60
5.2.1.1.2	Concentration profiles.....	64



5.2.1.1.3	Parameter study .....	65
5.2.1.2	Gelatin porous electrode .....	67
5.2.1.3	Influence of thickness on electrode performance .....	72
5.2.1.4	Influence of enzyme and mediator on electrode performance using the Gelatin procedure.....	73
5.2.2	Porous electrode with O <sub>2</sub> supply .....	77
5.3	Enzymatic cathode .....	80
5.3.1	Thin film electrode.....	81
5.3.1.1	Steady state polarization.....	81
5.3.1.2	Electrochemical impedance spectroscopy.....	86
5.3.2	DET porous electrode with a single enzyme .....	90
5.3.2.1	PVDF porous procedure .....	91
5.3.2.2	Gelatin porous procedure .....	94
5.3.2.3	Higher range of concentration .....	97
5.3.3	Porous electrode with the enzymatic cascade GOx-HRP .....	100
<b>6</b>	<b>Concluding remarks and outlook.....</b>	<b>106</b>
6.1	Conclusions.....	106
6.2	Outlook.....	109
	<b>List of figures.....</b>	<b>111</b>
	<b>List of tables.....</b>	<b>115</b>
	<b>Bibliography.....</b>	<b>117</b>
	<b>Appendix 1: Derivation of the reduced 1-D model.....</b>	<b>129</b>
	<b>Appendix 2: Derivation of steady state expressions of the interface model .....</b>	<b>130</b>
	<b>Appendix 3: The derivation of electrochemical impedance spectroscopy of Model 3 .....</b>	<b>133</b>

# List of symbols

Latin symbols	Name	Unit
a	internal active surface area	$m_{\text{act}}^2 m_{\text{geo}}^{-3}$
$A_{\text{geo}}$	geometrical surface area of electrode= $0.28 \times 10^{-4}$	$m_{\text{geo}}^2$
C	volumetric concentration	$\text{mol m}^{-3}$
D	diffusion coefficient of species in bulk	$\text{m}^2 \text{s}^{-1}$
E	electrode potential	V
$E_r$	reversible potential	V
F	Faraday's constant=96485	$\text{C mol}^{-1}$
I	total current	A
j	total cell current density	$\text{A m}_{\text{geo}}^{-2}$
$k, K$	reaction constants of enzyme substrate and enzyme mediator reactions	$\text{m}^3 \text{mol}^{-1} \text{s}^{-1}, \text{s}^{-1}$
$k_{e0}, k_{e1}, k_{e2}$	electrochemical kinetic constants	$\text{ms}^{-1}, \text{s}^{-1}, \text{s}^{-1}$
L	catalyst layer thickness	$m_{\text{geo}}$
$R_{\text{ohm}}$	electrolyte resistance	$\Omega$
r	reaction rate	$\text{mol m}^{-3} \text{s}^{-1}$
R	universal gas constant=8.314	$\text{J mol}^{-1} \text{K}^{-1}$
T	temperature	K
U	voltage	V

Greek symbols	Name	Unit
$\alpha$	transfer coefficient of the electrochemical step	-
$\Gamma$	surface concentration	$\text{mol m}_{\text{act}}^{-2}$
$\delta$	diffusion layer thickness	$m_{\text{geo}}$
$\varepsilon$	void fraction	$\text{m}^3 m_{\text{geo}}^{-3}$
$\zeta$	charge number	-
$\eta$	overpotential	V
$\iota$	local current density	$\text{A m}_{\text{act}}^{-2}$
$\kappa_E, \kappa_I$	electron-and ion conductivities	$\text{S m}_{\text{geo}}^{-1}$

$\Phi_E, \Phi_I$	potentials of electron-and ion- conducting phases respectively	V
$\omega$	rotation rate of rotating disc electrode	rad s <sup>-1</sup>

---



---

### Super- and Sub-scripts

---

RB, LB	right boundary and left boundary respectively
I, E	ion and electron conducting phase respectively
sim, exp	simulation and experiment respectively
red, ox	reduced and oxidized respectively
CL, DL	catalyst layer and diffusion layer respectively
S	substrate
Et/Mt	total enzyme and total mediator respectively
e0	electrochemical reaction step
act, geo	active and geometrical respectively
Ohm	Ohmic

---



---

### Abbreviations

---

3D	three-dimensional
AE	algebraic equation
AS	analytical solution
BES	bioelectrochemical system
BET	Brunauer–Emmett–Teller
BOD	bilirubin oxidase
BV	Butler-Vomer
BC	boundary condition
CNTs	carbon nanotubes
CTC	charge transfer complex
DAE	differential algebraic equation
DET	direct electron transfer
EES	electro-enzymatic system
EFC	enzymatic fuel cell
EIS	electrochemical impedance spectroscopy

EPE	enzymatic porous electrode
ES	enzyme substrate
E	enzyme
FC	fuel cell
FAD	flavin adenine dinucleotide
IC	initial condition
GDH	glucose dehydrogenase
GDL	gas-diffusion layer
GOx	glucose oxidase
HRP	hoseradish peroxidase
MEA	membrane electrode assembly
MET	mediated electron transfer
M	mediator
MWCNTs	multi-walled carbon nanotubes
NAD	nicotinamide adenine dinucleotide
NMR	nuclear magnetic resonance
NS	numerical solution
OCV	open circuit voltage
ODE	ordinary differential equation
PQQ	pyrroloquinoline quinone
PDE	partial differential equation
PVDF	poly(vinylidene fluoride)
QCM	quartz crystal microbalance
RDE	rotating disc electrode
SAM	self-assembled monolayer
SCE	saturated calomel electrode
SEM	scanning electron microscopy
SS	steady state
SWCNTs	single-walled carbon nanotubes
TCNQ	tetracyanoquinodimethane
TTF	tetrathiafulvalene

# 1 Introduction

*"We neither fear complexity nor embrace it for its own sake, but rather face it with the faith that simplicity and understanding are within reach"*

---

Frederick R. Adler

## 1.1 Motivation

Finding novel efficient and sustainable processes for chemical production and energy conversion is one of the biggest motivations of today's advanced technology. Electro-enzymatic processes can be one of the potential candidates due to the utilization of redox enzymes as biocatalysts in close combination with electrochemistry. Enzymes utilized in these electrochemical processes require mild working conditions (optimal at pH 4-8,  $T < 100\text{ }^{\circ}\text{C}$ , and atmospheric pressure), the use of renewable bio educts, and are highly selective to substrates. The working conditions and selectivity of enzymes can restrict the number of side reactions, which, in turn, can potentially exclude the membrane utilization inside the studied systems [1-2], avoid the use of environmentally unattractive organic solvents [3], and reduce the number of separation steps in downstream processes. In addition, a zero-operating energy cost system can be obtained when combining enzymes and electrochemistry due to the parallel running as a fuel cell (FC) and chemical conversion system.

The very first publication on electro-enzymatic system (EESs) dates back to the 1960s [4], but intensified research began in earnest during the last decade. To date, the electro-enzymatic systems (EESs) were very successful in biosensor applications due to the selectivity feature of enzymes [5-8]. They have been also employed as power sources, such as enzymatic fuel cells (EFCs), and bio-batteries [1, 7-9]. EESs were also exploited as biotransformation process for chemicals [10-19]. The most recent examples of the co-operating mode of energy and chemical conversion are gluconic acid production from glucose oxidation process in an electro-enzymatic reactor using GOx and HRP [20], and D-fructose production in multi-walled carbon nanotubes (MWCNT) anode containing D-sorbitol dehydrogenase immobilized in a silica matrix and an

oxygen gas-flow cathode [19]. Among the substrates using in EESs, the most common and intuitive substrate is glucose due to its huge availability in nature and essential role in human body. Glucose is also known as a renewable chemical platform for many other chemical synthesis processes [156-160]. Enzymes in EESs can be immobilized in a conductive matrix (so-called a catalyst layer (CL)) or freely diffused in a solution phase. The free moving enzyme operation mode was applied mostly in biosensors, while the immobilized enzyme configurations have more applications in fuel cells or reactors because enzymes dissolved in solution can create a complicated downstream process [21].

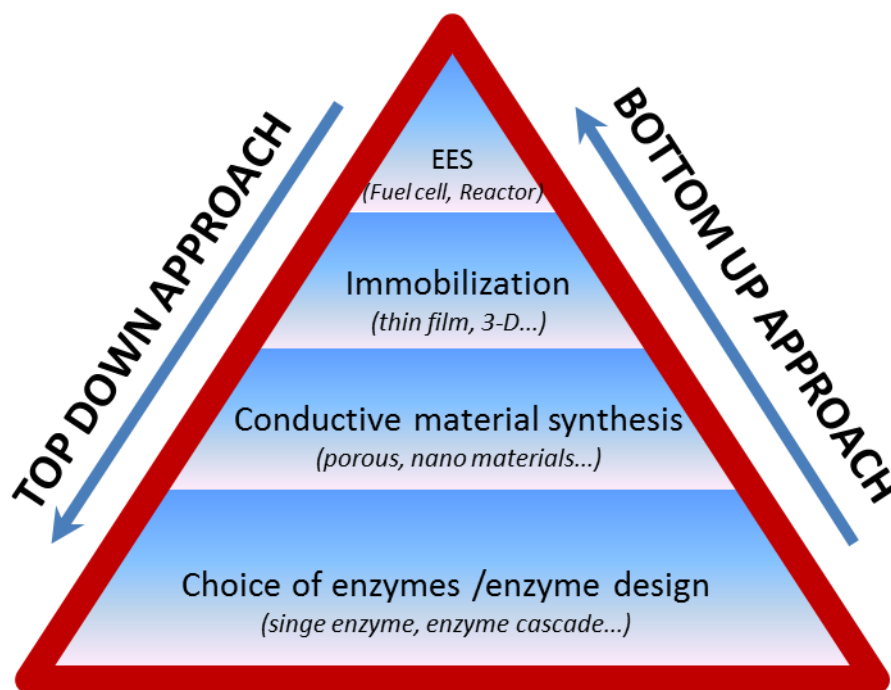


Figure 1-1: Different approaches in designing electro-enzymatic systems

The different research fields in EESs can be seen in Figure 1-1. They cover from enzyme selection, material design, and the immobilization technique, to the complete EES. Research-wise, the bottom up or top down approaches can be selected depending on the interests. Despite significant progress in the last 30 years, the applications of EESs are still restricted at the lab stage due to a low catalyst density, low current density and short system life time [7-9, 22]. The low catalyst density is constrained by the enzyme properties (charged or neutral, hydrophilic or hydrophobic, size), and the enzyme compatibility to conductive matrix. The low current density relates to the electron communication of enzyme active sites to an electron

conductive surface or the oxidation level of fuels to obtain higher number of electron transfer. The short system life time is due to the working environment, support and immobilization conditions [23]. Depending on the selected applications, different optimization strategies can be realized. For most research the experimental approach was taken to tackle these problems. The focus was either on a detailed understanding of the enzymes in EES or on engineering aspects with reports of incremental increases in performance from EESs with advanced designs. These engineering aspects may focus on finding a suitable enzymatic catalyst, high electrochemical active surface materials and the immobilization technique to maximize the electrode performance. Finding a catalyst relates mostly to a product to be converted, the turn-over number, stability, and the electron transfer pathway. Protein engineering can contribute significantly to the design of small enzyme molecules which allow an enzyme electronic charge being accessible into a conductive surface [24]. It can touch on shape, size, isoelectric points and the orientation of active sites of enzymes. However, it needs great effort and remains relatively unexplored. From the point of completed/partial oxidation of chemicals/fuels, an enzymatic cascade has been considered as an exciting perspective [25-26]. Among the above efforts, the different immobilization techniques, focused mainly on finding materials, using different binders, and preparation procedures, have been found widely in the literature [27]. Proper/optimized enzyme immobilization can also resolve problems related to enzyme instability and low activity under certain conditions, which could replace the need for extensive protein engineering [28].

An immobilization technique can result in a thin film electrode or a three dimensional (3-D) electrode depending on the application and preparation procedure. For a system requiring a higher number of enzymes or a high current density, the 3-D immobilization technique is commonly used. In the 3-D structure, enzymes are immobilized in electron conductive materials with the help of additional additives such as mediators, and binders [29]. The consequence of the electrode fabrication using different materials is that the performance depends greatly on the physicochemical interactions of these components. These are of importance; for example, enzyme orientation on conductive materials and the material arrangement inside the conductive matrix. To design, improve and optimize the efficiency of these bio(electrochemical)

systems, detailed knowledge and understanding of the involved processes (enzyme kinetics, electron transfer kinetics, mass transfer and charge transfer) and their interactions are crucial. In this respect, beside advanced experimental approaches, mathematical modelling plays an important role in accelerating and evaluating the processes toward real applications. The mathematical model is likely to provide useful information via the process analysis, parameterization, and investigation of the interactions of different physicochemical processes. As an output, it can propose the feasible operating range to optimize the system in a suitable working time frame.

To date, the number of mathematical modelling and simulation works in this area is still modest, and far beyond real applications. The focuses can be found similarly as the experimental approach presented in Figure 1-1. The main activities in modelling of EESs beyond the molecular level are summarized in Table 1-1. In the electrode configurations, the simple designs for the mediated electron transfer (MET) systems (for example, the free moving enzymes/mediators in contact with a conductive surface, entrapped enzymes/mediators behind a membrane, and physical absorbed enzymes on conductive supporting materials) have been focused on more in the literature. The major works on the interface models presented in the literature are based on the assumption of neglecting the dimension of the CL or the morphology of an electrode [5]. Many works on the interface model are referred to the Bartlett's review on the mathematical modelling of biosensor electrodes [5]. These models are helpful for kinetic determination and single process analysis, since other factors such as mass and charge transports are negligible in these systems. The mathematical modelling becomes more complicated in higher dimensional electrodes due to the significant contribution of the spatial distribution of species inside the conductive matrix. Therefore, the structural parameters, electrode morphology and the behaviour of different processes inside the CL need to be incorporated into the model. Researchers have not treated the CL in much detail and only few relevant works can be found in the literature; for example, the works of Lyons [30], Baronas et al [31], Barton [32], and Chan et al [33](Table 1-1). These works showed the importance of the distributed model in the process analysis, for instance, pointing out the substantial contribution of the mass transport limitation, lower enzyme utilization, and



significant influence of structural parameters, i.e porosity and thickness on the electrode response.

**Table 1-1: Summary of enzyme electrode models in the literature**

Configuration	Purpose	Operation type	Involved process	Method	Ref
Thin film model	- Kinetic modelling - Determining controlling step	- Steady state - Transient	-Multi-step enzyme/mediator kinetics -Diffusion	- AS - NS	[5,44]
Distributed model	- Parameter sensitivity - Process analysis	- Steady state - Transient	- Multi-step enzyme/mediator kinetics -Diffusion	- AS - NS	[30-33]
EES	- Parameter sensitivity - Process analysis	- Steady state - Transient	- Multi-step enzyme/mediator kinetics -Diffusion	- AS - NS	[33,43]

*AS: analytical solution NS: Numerical solution*

At the whole EES level i.e a reactor or a FC, the simulation work is even more challenging in comparison to the traditional chemical process due to the level of complexity of the model and the numerical feasibility for a dynamic modelling. In the EESs, the rate process can be very complex bringing together biochemical, chemical, surface reactions, electron exchange, charge transport, adsorption, desorption and mass transport of different species. Subsequently, the rate processes are not only dependent on parameters such as temperature, pressure, concentration, surface characteristic, structural parameters and pH, but also the potential at the solid-solution interface. Therefore, modelling and optimization should be carried out carefully in the simplest way and combined closely with the experimental work. Only a few records of the mathematical modelling of complete EESs can be found in the literature. Examples of such works can be tracked in previous reports [34-42]. In these studies, EES models were combined with experimental data, concentrated on the modelling of for example fuel utilization, oxygen mass transport limitations [43], optimum electrolyte composition, the constraint of enzyme utilization, mediator diffusion/depletion and interplay of enzymatic/electrochemical processes; kinetic study; and the influence of pH and porosity. In

the chemical conversion systems, the focus has been on pure modelling works providing numerical simulation tools [17], and detecting the feasible working zone of a reactor [40].

Furthermore, parametrization and experimental calibration are essential in the mathematical modelling. However, in most of the previous modelling works on EESs the parameters used in the simulation were normally adopted from different sources or were assumed. A systematic approach to obtaining reliable parameters for further use is rarely found in the literature.

The specific contributions of this dissertation are mainly on the mathematical modelling aspect at the electrode level. A significant effort has been made on determination of the reaction mechanism, and reliable kinetics parameters by optimization with experimental data. A systematic modelling approach to understand reaction mechanism and system behaviour from single enzyme to the enzymatic cascade is presented in this work.

## **1.2 Aims of the study**

An understanding of the complex interaction in an electro-enzymatic process is the prerequisite for rational improvement of a system. This requires realistic and thus physically interpretable mathematical model and appropriate targeted measurement techniques. The aims of this work are mainly to provide an insight into the selected systems with the help of mathematical modelling. The systems vary from a thin film electrode to 3-D electrodes. The model calibration with experimental data and parameterization is also considered. In particular, this involves the consideration of the following questions:

1. With given experimental data and a set of rival plausible mathematical models, which methodology can be used to discriminate between these models and to select the best model for further analysis, prediction and design?
2. For a given enzymatic porous electrode, which mathematical modelling approach is suitable for describing the system behaviour and how will the model be developed? How do preparation procedures impact on the system performance and selection of electrode for different applications?

3. How will the major differences between the mediated electron transfer (MET) and the direct electron transfer (DET) mechanisms influence the system performance?
4. Can the optimized parameters from previous relevant systems be justified for use in subsequent related systems?

These research questions are also systematically presented in Figure 1-2. The answers to these questions would also contribute to an improved understanding of the fundamental and practical problems governing EES design. To ensure the validity of the mathematical predictions, experimental calibration is required. The selected examples of EESs for modelling in this work were motivated by the development of EFCs and the bioreactor for gluconic acid production making use of glucose and oxygen ( $O_2$ ) as fuels.

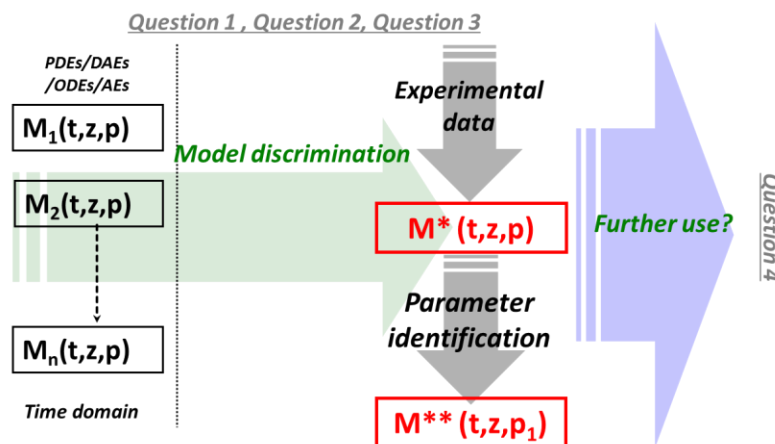


Figure 1-2: Schematic representation of the process system engineering (PSE) modelling approach which includes the steps in finding answers to the research questions

Obviously, there are numerous other questions in the understanding of the electro-enzymatic process which are not addressed here; for example, are the influence of an enzyme orientation distance, and the enzyme agglomeration on the reaction kinetic constants. These topics, which are out of the scope of this dissertation, can be of relevance for future research.

### 1.3 The dissertation structure

In this dissertation, the related theoretical background of enzymes in electrochemical processes, enzymatic electrode applications and the challenge of EES, and a general macroscale mathematical modelling of electrodes are addressed in Chapter 2. The details of the

mathematical model equations of the selected systems are formulated in Chapter 3. The special focuses of this chapter lie in the mathematical description of enzymatic electrodes utilizing horseradish peroxidase (HRP), glucose oxidase (GOx), and the enzymatic cascade of GOx-HRP. These enzymes are specifically interested in the BES producing gluconic acid from glucose oxidation [20]. The mathematical equations vary from partial differential equations (PDEs), ordinary differential equations (ODEs), differential algebraic equations (DAEs) to algebraic equations (AEs). The mathematical equation systems, including balancing equations incorporated with specific kinetics and transport laws, are presented in a sequence as shown in Figure 1-3. The distributed model, including charge balance, mass balance incorporated with kinetics and all necessary boundary conditions, is firstly applied to the enzymatic porous anode using GOx as the model enzyme and tetrathiafulvalene (TTF) as the mediator. After this, the mathematical models on the cathode side using HRP and the enzymatic cascade of GOx-HRP, are presented. The details of the experimental validation for reference and calculation convenience are provided in Chapter 4. A similar sequence as in the mathematical modelling section to present the outcomes of the simulation follows in Chapter 5. The dissertation concludes with the research contributions and discussion for future works.

**Continuous lines: parameter extraction**    **SS: Steady State, TS: Transient State**  
**Dash lines**    : **Substrate supply**    **EIS: Electrochemical impedance spectroscopy**

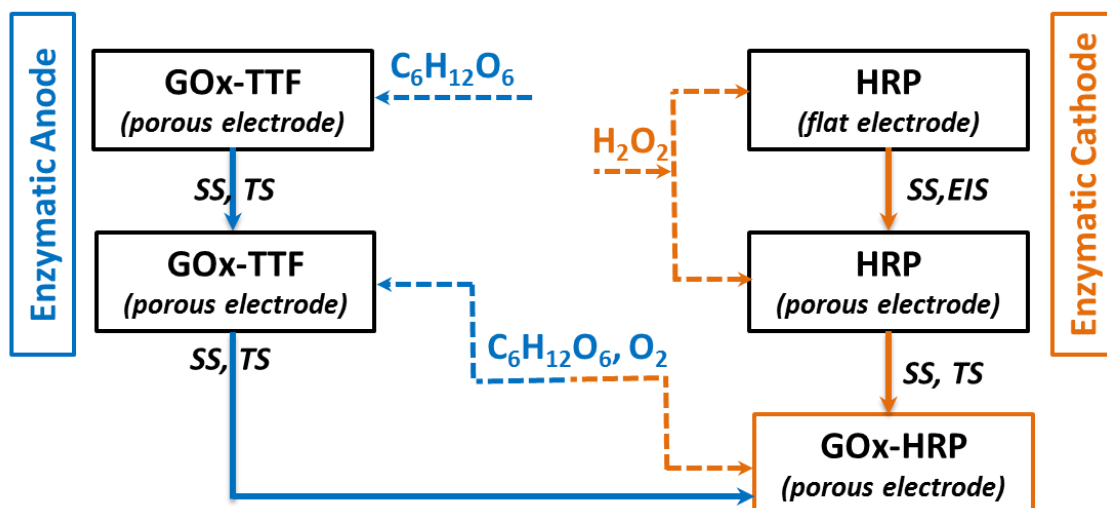


Figure 1-3: Schematic representation of the different steps of modelling to obtain parameters subsequently used for the GOx-HRP cascade

## 2 State of the art

### 2.1 Enzymes in electrochemical processes

#### 2.1.1 Enzymes as biocatalysts

Enzymes are crucial for the life and functions of the human body and microorganisms. To catalyse correctly the metabolic pathway in a single cell, an average of 3000 different enzymes is needed [45]. These enzymes are proteins functioning as natural bio-catalysts, accelerating chemical transformation without altering the equilibrium. For the catalytic function, the catalytic active centre of an enzyme is the most important part, where a chemically and spatially congruent substrate is converted into a product (Figure 2-1). This conversion follows the so called lock and key mechanism model proposed by Emil Fischer in 1894 [46]. In this model, a reactant (substrate) as ‘a key’ fits only into a specific active enzyme centre (‘lock’). In the induced-fit model proposed by Daniel E. Koshland, Jr., in 1958, the active site of enzymes can undergo a conformational change to fit the substrate to some extent. Alternatively, the enzyme may distort the substrate, forcing it into a conformation similar to that of the transition state [47].

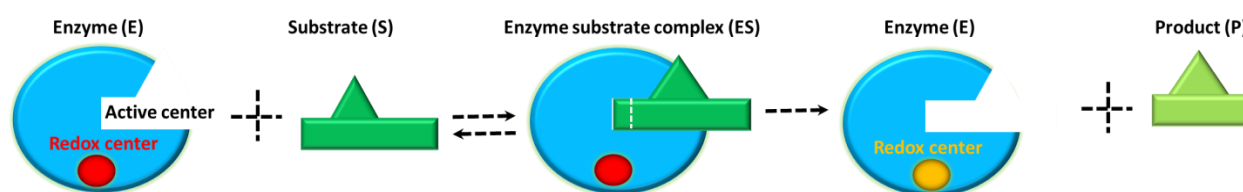


**Figure 2-1: Schematic representation of the “lock-and-key” mechanism for an enzyme substrate reaction (particularly for oxidoreductases)**

Enzymes can be produced by the expression methods from bacteria, moulds, yeasts, plants and animals. They are categorized into six major groups namely oxidoreductases, transferases, hydrolases, lyases, isomerases, and ligases depending on particular reactions which they can catalyse [45]. Among them, the oxidoreductases group, which catalyse oxidation-reduction reactions by exchanging hydrogen atom or an electron, is particularly

important and relevant in electro-enzymatic applications. The fundamental structure of these redox enzymes consists of catalytic sites connected by a redox centre (Figure 2-1). The redox centre(s) (or cofactors) can be tightly or loosely bound to the enzyme and act as sinks and sources of electrons. Cofactors can be a single inorganic ion or more than one inorganic ion (e.g. Cu, or Fe-Ni), or a complex organic compound (FAD, NAD) or a metalloorganic molecule.

In various electrochemical applications, either a single enzyme or an enzymatic cascade of different enzymes can be used. For example, a single enzyme is used to detect a specific chemical in biosensor applications or several enzymes can be cascaded to obtain the completed oxidation of a fuel in chemical and energy conversion systems. The enzymatic cascade is inspired by the natural metabolic pathway in which many enzymes are in charge of a sequence of chemical reactions. An example of a cascade is the use of enzyme couple consisting of GOx and HRP in order to increase the performance and selectivity of GOx biosensors [48-49]. Under the O<sub>2</sub> supply condition, H<sub>2</sub>O<sub>2</sub> is produced by GOx and it is subsequently reduced by HRP. The bi-enzyme system is also used to increase glucose conversion in an electro-enzymatic reactor [20]. Plamore et al. employed a cascade consisting of three enzymes (NAD<sup>+</sup>-dependent alcohol- (ADH), aldehyde- (AldDH), and formate-(FDH) dehydrogenases) for the complete oxidation of methanol to carbon dioxide [50]. Zhiguang Zhu and co-workers used an enzymatic cascade consisting of 13 enzymes in their sugar biobattery [51]. Nearly 24 electrons per glucose unit were produced through the synthetic metabolic pathway.

### **2.1.2 Enzymes as an electron donor/acceptor on a conductive surface**

Enzymes, belonging to oxidoreductases in EESs, can exchange electrons on a conductive surface in two pathways, namely DET and MET, depending on the distance between redox centres to a conductive surface (the so called electron tunnelling distance) (Table 2-1). In general, if the distance is smaller than 2 nm, enzymes are capable of DET and are able to pass electrons directly to a conductive surface [8, 52-53]. Otherwise, the presence of a suitable redox-active molecule (mediator) is required. Accordingly, the enzyme regeneration step can be either a DET or enzyme-mediator related step (Eq. (4)).

Table 2-1: Survey of DET and MET

	Direct Electron Transfer (DET)	Mediated Electron Transfer (MET)
Schematic representation		
Typical reaction steps	$E_{ox} + S \xrightleftharpoons[k_-]{k_+} ES \xrightarrow{k_{cat}} P + E_{red} \quad (1)$ $E_{red} \xrightarrow{k_e} E_{ox} + H^+ + e^- \quad (2)$	$E_{ox} + S \xrightleftharpoons[k_-]{k_+} ES \xrightarrow{k_{cat}} P + E_{red} \quad (3)$ $E_{red} + M_{ox} \xrightarrow{k_M} E_{ox} + M_{red} \quad (4)$ $M_{red} \xrightarrow{k_{e0}} M_{ox} + H^+ + e^- \quad (5)$
Advantages	-Fewer reaction steps	-Higher current density in comparison to DET
Disadvantages	-Requirement of proper orientation of enzymes to have a short tunnelling distance, -Requirement of a high enough number of active enzymes.	-More reaction steps, -More chemicals introduced to the system, -Lower open circuit voltage (OCV).

*In the table, the subscripts 'ox, red' stands for oxidation and reduction respectively, 'cat' for catalyst, '+, -' for forward and backward reactions, 'e' for electrochemical.*

The number of enzymes featuring DET is less than 1000 redox enzymes [54]. The majority of these are redox proteins containing metalcenters (e.g. heme, copper, nickel or iron–sulfur clusters...) and an organic cofactor (flavin adenine dinucleotide (FAD), pyrroloquinoline quinone (PQQ)) in their active sites. However, for most enzymes, a mediator/polymer is required as an electron carrier because a redox unit is deeply buried into the protein periphery, non-associated and isolated with a thick carbohydrate shell [6]. The crucial requirements of mediator species include stability and selectivity of both oxidized and reduced forms, reversible redox chemistry, and operating at low over-potential. The mediators can be metal-based or organic. They can be immobilized or freely supplied from a solution [55-56].

### 2.1.3 How are enzymes embedded into electro-enzymatic electrodes?

For EESs, enzymes are known as non-electron or low conductive catalysts. Therefore, they are usually incorporated with other electron conducting supports such as carbon nanomaterials or conductive polymers. Other materials, for example, binders, stabilizers, conducting materials and additionally mediators are also introduced into the electrode. Enzymes can be attached into a conductive surface matrix employing different immobilization procedures as reported in the literature, which result in different electrode configurations (Figure 2-2). These procedures include simple physical adsorption, covalent attachment, cross-linking and entrapment in polymeric gels [27]. The physical adsorption and covalent attachment normally result in a thin film electrode which has a basic 2-D configuration. The introduction of additional materials in the cross-linking and entrapment results in a 3-D electrode structure. Thus, 3-D configuration is more favourable for practical applications because of a higher number of catalysts per geometry surface area and the possibility of a longer period of activity. However, the 3-D structure can cause different problems; for example, mass transport of substances, the interaction of different processes, and complicated chemistry inside the CL.

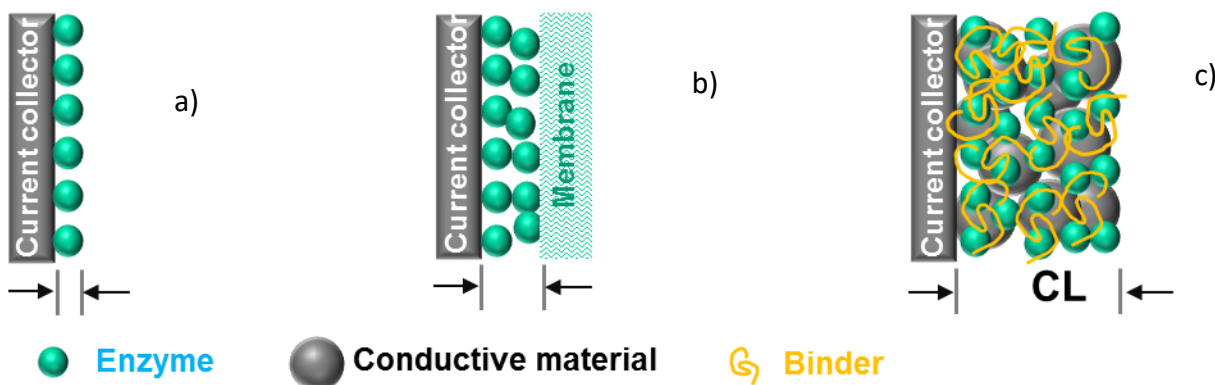


Figure 2-2: Schematic representation of different electrode configurations: a) a monoenzyme layer, b) multi-enzyme layers entrapped behind a membrane and c) a porous enzymatic electrode

The conductive materials, used in the 3-D electrode, are normally the carbon-based and/or nanostructured materials i.g. spectrographic graphite electrodes [57-58] or carbon nanotubes (CNTs) [59- 61]. In the case of MET enzymes, mediators can be freely diffusive or immobilized [56]. Immobilized enzyme-mediator electrodes are usually preferred because of



their higher electron transfer efficiency and stability. Therefore, numerous efforts have been made to gain an efficient immobilization procedure of mediators and enzymes in a conductive porous structure. These include the use of 3-D matrices such as polymers, lipids and CNTs or the combinations of these to incorporate enzymes and mediators, Os-based redox hydrogels as mediators [56]. Beside these efforts, a meso-ordered porous structure has recently drawn attention as it can overcome the mass transport, and agglomeration problems [62-63].

#### 2.1.4 Application of enzymatic electrodes

The first electro-enzymatic system was conducted by Yahiro *et al.* in 1964. Since then, numerous publications evaluating the performance and applicability of enzymatic electrodes and electro-enzymatic systems such as biosensors, EFC, enzymatic batteries and enzymatic reactors have been reported [7, 51, 63-64]. In these applications, the biocatalysts can be immobilized on either one electrode or both in a complete EES [7, 65].

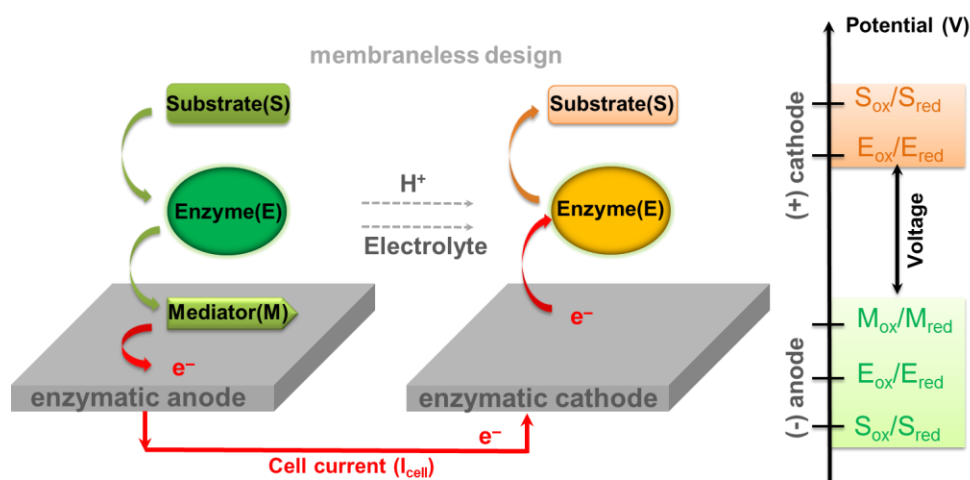


Figure 2-3: Schematic presentation and working principle of an enzymatic biofuel cell

Due to several properties of enzymes, the systems using enzymatic electrodes allow the use of inexpensive components or a membrane-less design system. Difficulties arise mainly from establishing the electrical communication of enzymes/mediators to a conductive surface, the stability of catalyst electrode assembly, the oxidation level of fuels, resistances and mass transport [8, 7]. In the case of MET (Figure 2-3), additional problems can be lower cell voltage, higher operating costs, the downstream process and the complicated interaction with other chemicals [7, 56]. In biotransformation applications, the selectivity of enzymes can eliminate

the by-products formed by side reactions, still the complicated catalytic activity can still also generate other products. The conversion of educts can be highly correlated to the cell current density and cell voltage as if the electrochemical step relates directly to the conversion of desired educts.

As a power system, EFCs can be used as a power source for implantable devices or general power devices. In 2007, Sakai et al. reported a prototype of an enzymatic battery which is being trialled by Sony® [66]. Theoretically, the utilization of a biocatalyst provides the accessibility of EFC as a miniaturized power source used in small implantable device such as the cardiac pacemakers, neurostimulators, hearing and vision devices, drug pumps, glucose sensors, and bladder-control valves [1, 67-68]. The possibility of their applications as power sources in implantable devices has been demonstrated by the implantation of a bio-FC in a living rat [64, 69]. Nevertheless, the competition with metal-based FCs is low due to the power output and long term stability. Great effort has been made recently to increase the power of EFCs. An example is the utilization of 13 enzymes to gain complete oxidation of a glucose unit in a maltodextrin/sugar bio-battery. It can provide a current density of  $6 \text{ mA cm}^{-2}$  and power output of  $0.8 \text{ mWcm}^{-2}$  [51]. A system containing a 15% (wt/v) maltodextrin solution has an energy-storage density of  $596 \text{ Ah kg}^{-1}$ , which is one order of magnitude higher than that of lithium-ion batteries.

To date, several electroenzymatic processes for commodity production are still in the lab development stage. In these works, the reactor configuration may greatly differ, but there is a clear trend towards electro-enzymatic membrane reactor utilization. The commonly used membranes can be dialysis membranes [14, 70] or filtration membranes, e.g. ion-exchange membrane [71-72]. In respect to electrochemical/membrane system configuration, there are two different set-ups that can be found in the literature; namely, split and compact configurations. In the first system, the electrochemical and membrane reactors are two separate apparatuses incorporated in a solution loop. The membrane reactor removes the product continuously and keeps the enzyme in the recycling loop [73]. In the latter case, the electrochemical and enzymatic reactors are integrated in the same apparatus and therefore, the electrochemical and enzymatic reactions occur in the same place. A theoretical study has

demonstrated that the compact configuration provided a higher performance than the split process [74]. In compact equipment, enzymes are confined to a CL, near to the electrode surface. This allows the use of a minimal quantity of enzymes for a maximal volume of solution to be processed, retaining enzyme activity, preventing the use of pumps or pipes for enzyme circulation, and eliminating  $O_2$  as natural electron acceptor. Up till now, these reactor configurations are running non-spontaneously; i.e. they require external input of electrical energy for continuous operation. The other type of reactor configuration is the membraneless electroenzymatic reactor [20]. An example of this system is the gluconic acid production in an EFC, coupling a GOx porous anode and the enzymatic cascade of GOx-HRP porous cathode in the same device. The electroenzymatic reactor, operated in the mode of co-generating chemicals and electrical energy, has shown potential in exploring a gluconic production system [20]. The space time yield of gluconic acid achieved at a glucose conversion of 47% was  $18.2 \text{ g h}^{-1} \text{ cm}^{-2}$ . Further improvement in glucose conversion can be realized by correlation of its performance to applied potential and other operating conditions.

## **2.2 Mathematical modelling of a porous electrode**

In general, the porous electrode is more preferable for practical electrochemical systems which require higher performance. The porous part immobilized with catalysts is called a CL. It is a compact conductive matrix consisting of three main elements: catalysts, electron- and ion-conducting matrixes. An optimized electrode design should offer a harmonized interconnection of the three components to offer a pathway for reactants, electrons and ions to be transported inside the CL and to offer a high electrochemical conductive surface for an electrochemical reaction taking place. A detailed simulation of such a structure requires enormous computational power. Depending on the area of interest, CLs have been modelled with varying degrees of complexity such as an interface, homogeneous or inhomogeneous layers in 1-D, 2-D or 3-D, or in microscopic and macroscopic scales. Among the models, macroscale ones are the most practical predictive models to provide a straightforward relationship with experimental measurable quantities i.e polarization curves. Moreover, the reaction and diffusion processes and other phenomena rarely happen in spatially distinct regions in a porous electrode. For a detailed reference of the porous model theory, readers are recommended to refer to the book

of Newman [75], in which the theory has been applied broadly in porous batteries, and a CL of a gas diffusion electrode in a polyelectrolyte membrane fuel cell (PEMFC). Special attention in this section is given to macroscopic CL models of a porous electrode used reduced model formulations.

### 2.2.1 Catalyst layer physical structure

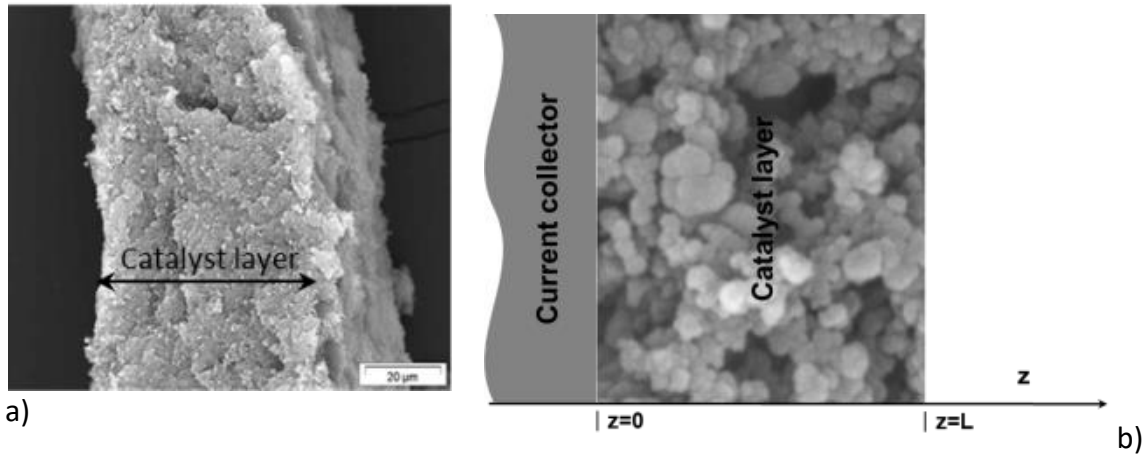


Figure 2-4: Schematic representation of: a) SEM image of CL; b) typical modelling domains

A typical representation of a porous enzymatic system is presented in Figure 2-4. The pore networks are created during the synthesis process among the used components. The porous mathematical model approach treats the CL as a continuum, introducing effective transport properties e.g. diffusion coefficients, and ionic and electric conductivities, as a function of CL morphology such as porosity. The exact geometrical details of the electrode are usually ignored. All reactions take place only in a CL. Electrochemical consumption/production happens only at the electron-conducting interface. The electron- and ion-conducting phases are considered as distinct phases and void fraction “ $\epsilon$ ” is used to characterise these phases. The other parameter defined further for CL is the internal active surface area “ $a=A_{act}/(A_{geo}L)$ ” (in  $m^2_{act} m_{geo}^{-3}$ ), where  $A_{act}$  is the active surface area,  $A_{geo}$  the geometrical surface area and  $L$  the thickness of the porous electrode. The mathematical formulations in the CL include the balances of potential distributions in the electron- ( $\phi_E^{CL}(z, t)$ ) and ion- ( $\phi_I^{CL}(z, t)$ ) conducting phases as well as the potential distribution  $E(z, t)$  at the interface. In the CL modelling domain, all mass balance equations for species involved in reactions have been introduced. During the

operation, the Nernst diffusion layer (DL) forms in front of the CL. The second diffusive flux is usually used to approximate the mass transfer in the DL. For the sake of simplicity, this section ignores the contribution of the DL.

### 2.2.2 Governing equations

Consider the following representative electrochemical reaction inside the CL



in which ox/red are the oxidized/reduced forms of a chemical, respectively.

The rate of the above electrochemical reaction  $r_k(z, t)$  is dependent on time and spatial coordinates and can be described by the following expression:

$$r_k(z, t) = f(\eta(z, t), c_\alpha(z, t), T(z, t) \dots) \quad (7)$$

where  $c_\alpha(z, t)$  is the concentration field,  $T(z, t)$  the temperature field and  $\eta(z, t)$  the overpotential.

The spatial profile of the overpotential  $\eta_k(z, t)$  is calculated from the potential field within the electron conductor  $\phi_E(z, t)$ , the ionic conductor  $\phi_I(z, t)$  and the equilibrium potential difference  $\Delta\phi_0(z, t)$  of the  $k^{\text{th}}$  reaction.

$$\eta(z, t) = \underbrace{\phi_E(z, t) - \phi_I(z, t)}_{E(z, t)} - \Delta\phi_0(z, t) \quad (8)$$

where subscript  $I$  is for the ion,  $E$  for the electron.

The spatial profiles of the relevant variables i.e  $c_\alpha(z, t)$ ,  $T(z, t)$ ,  $\eta(z, t)$ ,  $\phi_E(z, t)$ ,  $\phi_I(z, t)$  on the macro-scale are specified in porous-electrode models [75-76]. The following section is the general balancing of these quantities and consequently the model reduction is presented.

#### 2.2.2.1 Potential field-charge balance

The charge balance for the electron conducting and the ion conducting phases and the interface inside the CL are presented in Table 2-2, Table 2-3, and Table 2-4.

Table 2-2: Charge balance of the electron conducting phase

Charge balance	Mathematical equation	Boundary conditions (BCs)
Electron conducting phase $\phi_E(z, t)$	$0 = -\frac{\partial}{\partial z} \left( \underbrace{-\kappa_E^{\text{eff}} \frac{\partial \phi_E}{\partial z}}_{j_E} \right) + a \iota \quad (9)$	<ul style="list-style-type: none"> <li>• <math>-\kappa_E^{\text{eff}} \frac{\partial \phi_E(z, t)}{\partial z} \Big _{z=L} = 0 \quad (10)</math></li> <li>• <math>\phi_E(0, t) = \phi_E^{LB}(t) \quad (11)</math></li> </ul>

In the Table 2-2, the first BC of the electron conducting phase represents the fact that the potential at  $z=0$  is known while the second one ensures that no current leaves the electron conductor at the end of the CL.

**Table 2-3: Charge balance of the ionic conducting phase**

Charge balance	Mathematical equation	BCs
the ionic conductor $\phi_I(z, t)$	$0 = -\frac{\partial}{\partial z} \left( \underbrace{-\kappa_I^{\text{eff}} \frac{\partial \phi_I}{\partial z}}_{j_I} \right) - a \iota \quad (12)$	<ul style="list-style-type: none"> <li>• <math>-\kappa_I^{\text{eff}} \frac{\partial \phi_I(z, t)}{\partial z} \Big _{z=0} = 0 \quad (13)</math></li> <li>• <math>\phi_I(L, t) = \phi_I^{\text{RB}}(t) \quad (14)</math></li> <li>• <math>-\kappa_I^{\text{eff}} \frac{\partial \phi_I(z, t)}{\partial z} \Big _{z=0} = -j(t) \quad (15)</math></li> </ul>

where  $\kappa_E^{\text{eff}}, \kappa_I^{\text{eff}}$  refer to the effective conductivities of the electron conducting phase and the ion-conducting phase respectively, " $\iota$ " to the local current density and " $a$ " to the internal active surface area and, subscript 'eff', 'LB' to effectiveness, and left boundary respectively.

Table 2-3 represents the fact that the potential at  $z=L$  is known and there is no charge moving out at  $z=0$ . Alternatively, if the system is operated galvanostatically, the BC can be provided by the potential gradient (Eq. (15)).

**Table 2-4: Charge balances at the electrochemical interface inside the CL**

Charge balance	Mathematical equation
At the interface $E(z, t) = \phi_E(z, t) - \phi_I(z, t)$	$c_{dl} \frac{\partial}{\partial t} (\phi_E - \phi_I) = -\iota + F \sum_k n_k r_k \quad (16)$
The total current density of CL	$j(t) = \int_{z=0}^{z=L} a \iota(t, z) dz \quad (17)$

Table 2-4 shows the charge balance at the electron conductive interface. The final solutions of equations (9, 12, 16) are the local profiles of  $\phi_E(z, t)$ ,  $\phi_I(z, t)$  and  $\iota(z, t)$ , respectively. From the known  $\phi_E(z, t)$ ,  $\phi_I(z, t)$ , the spatial profile of the overpotential can be calculated based on Eq. (8), which is necessary to evaluate the rate expression for  $r_k$  (Eq. (7)). The current ( $j(t)$ ) produced in the whole CL is presented in Eq. (17). Alternatively, it can be achieved by integrating Eq. (12) over the whole CL thickness to obtain:

$$j(t) = - \underbrace{\left( -\kappa_E^{\text{eff}} \frac{\partial \phi_E}{\partial z} \Big|_{t, z=L} \right)}_{j_E(t, z=L)} \quad (18)$$

$$j(t) = - \underbrace{\left( -\kappa_I^{\text{eff}} \frac{\partial \phi_I}{\partial z} \right)_{t, z=L}}_{j_I(t, z=0)} \quad (19)$$

The effective conductivities ( $\kappa_E^{\text{eff}}, \kappa_I^{\text{eff}}$ ) of the electron- and ion-conducting phases appearing in Eqs. (18, 19) are defined as the effective conductivities related to the conductivities of the pure phases in accordance to Bruggemann's correlation:

$$\kappa_E^{\text{eff}} = \kappa_E (1 - \varepsilon)^{1.5} \quad (20)$$

$$\kappa_I^{\text{eff}} = \kappa_I \varepsilon^{1.5} \quad (21)$$

The charge balance of an electrochemical double layer is usually considered under quasi-stationary conditions in the system in which the contribution of the time constant of this equation is smaller than the others. As a consequence, the local current density  $i(z, t)$  has a straight-forward expression (Table 2-5).

**Table 2-5: Charge balance at quasi-stationary conditions**

Charge balance	Mathematical equation	BCs
Electron conducting phase $\phi_E(z, t)$	$\frac{\partial j_E}{\partial z} = aF \sum_k n_k r_k$ (22) $\frac{\partial \phi_E}{\partial z} = -\frac{j_E}{\kappa_E^{\text{eff}}}$ (23)	• $j_E(L, t) = 0$ (24) • $\phi_E(t, z = 0) = \phi_E^{LB}(t)$ (25)
Ionic conducting phase $\phi_I(z, t)$	$\frac{\partial j_I}{\partial z} = -aF \sum_k n_k r_k$ (26) $\frac{\partial \phi_I}{\partial z} = -\frac{j_I}{\kappa_I^{\text{eff}}}$ (27)	• $j_I(0, t) = 0$ (28) • $\phi_I(t, z = L) = \phi_I^{RB}(t)$ (29)
At the interface $E(z, t) = \phi_E(z, t) - \phi_I(z, t)$	$i(z, t) = F \sum_k n_k r_k(z, t)$ (30)	

### 2.2.2.2 Mass balances

The general mass balance equations of different species is presented in Eq. (31) with two BCs (Eqs. (32, 33)). The convection and migration terms are neglected. This works well with a system using a rotating disk electrode (RDE). The first BC is based on the fact that the concentration at  $z = L$  is known. The second BC ensures that no mass leaves the CL at  $z=0$ .

**Table 2-6: General mass balance equation**

Mathematical equation	BCs
$\varepsilon \frac{\partial C_\alpha}{\partial t} = -\frac{\partial}{\partial z} \left( -D_\alpha^{\text{eff}} \frac{\partial C_\alpha}{\partial z} \right) + a \sum_k \nu_{\alpha,k} r_k$ (31)	• $c_\alpha(z = L, t) = c_\alpha^{RB}(t)$ (32) • $-D_\alpha^{\text{eff}} \frac{\partial C_\alpha}{\partial z} \Big _{z=0} = 0$ (33)

Where " $r_k$ " refers to the reaction rate,  $\nu_{\alpha,k}$  to reaction stoichiometry

The diffusion coefficient  $D_{\alpha}^{\text{eff}}$  in the porous CL is an effective one, expressed in accordance with Bruggemann's correlation

$$D_{\alpha}^{\text{eff}} = D_{\alpha} \varepsilon^{1.5} \quad (34)$$

where  $i$  stands for reactants and  $D_i$  is the substance diffusivity in water.

### 2.2.2.3 Reduced 1-D model

The 1-D model can be reduced by integration of the distributed model equations along the thickness of the CL, and incorporation of all the corresponding boundary conditions. By doing this, the information on concentration distribution in the CL gets lost, but the structural information of the CL, including the void fraction, the thickness of the CL and the internal active surface area is preserved. The resulting equations are presented in Table 2-7. The derivation detail is referred in Appendix 1.

**Table 2-7: Mathematical expressions of a reduced 1-D model (Appendix 1)**

Charge balance	Mathematical equation
electron conductor $\phi_E^{\text{CL}}(t)$	$0 = -\kappa_E^{\text{eff}} \frac{\phi_E^{\text{CL}}(t) - \phi_E^{\text{LB}}(t)}{L/2} + j(t)$ (35)
ionic conductor $\phi_I^{\text{CL}}(t)$	$0 = \kappa_I^{\text{eff}} \frac{\phi_I^{\text{RB}}(t) - \phi_I^{\text{CL}}(t)}{L/2} - j(t)$ (36)
At the interface $E(t) = \phi_E^{\text{CL}}(t) - \phi_I^{\text{CL}}(t)$	$aL C_{dl} \frac{dE(t)}{dt} = -j(t) + F r_e(t) aL$ (37)
Material balance	$\varepsilon \frac{dC_{\alpha}^{\text{CL}}(t)}{dt} L = D_{\alpha}^{\text{eff}} \frac{C_{\alpha}^{\text{RB}}(t) - C_{\alpha}^{\text{CL}}(t)}{L/2} - aL \sum_k \nu_{\alpha,k} r_k(t)$ (38)

For a very thin electrode or vanishing of charge and mass transport resistances (i.e.  $C_{\alpha}^{\text{RB}}(t) = C_{\alpha}^{\text{CL}}(t)$ ), the reduced model can be approximated as an interface model.

## 2.3 Application of the distributed model into an electro-enzymatic system

As regarded in previous sections, enzymes in different applications can be immobilized on a conductive surface in different ways. As a consequence, the geometrical configuration of the electrode may vary due to the distinct material arrangement in different preparation procedures. Common examples for modelling domains of the enzymatic electrode configurations are presented in Figure 2-5 and can also be found in the literature (i.e [44, 77-78] for configuration Figure 2-5a, [79-81] for configuration Figure 2-5b, [82-84], for configuration Figure 2-5c.



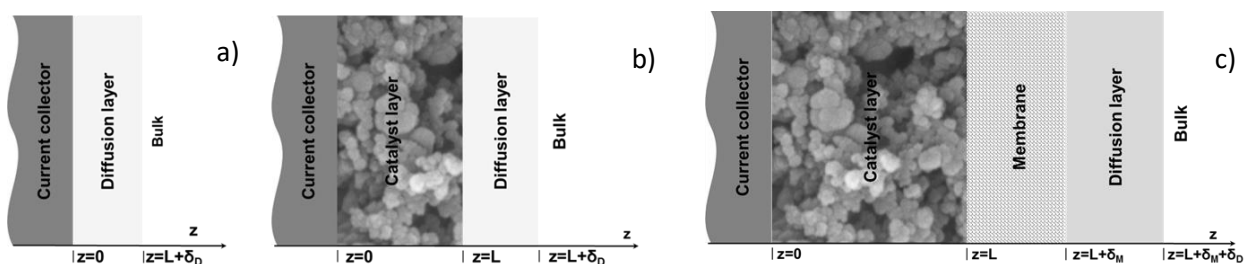


Figure 2-5: Schematic representation of the physical modelling domain: a) an interface model b) a spatial distributed model c) a spatial distributed model with enzyme layer trapped behind a membrane

Table 2-8: Interface and distributed models

Interface models	Distributed models
<ul style="list-style-type: none"> <li>➤ No consideration of spatial distribution of potential field</li> <li>➤ No CL modelling domain</li> <li>➤ useful for kinetic determination</li> <li>➤ Disregarding the influence of the structural parameters of the electrode</li> <li>➤ Practical for flat/interface electrodes</li> </ul>	<ul style="list-style-type: none"> <li>➤ Consideration of spatial distribution of related quantities; e.g. potential, concentration</li> <li>➤ Taking into account the concentration distribution of involved species in all different layers; for example, the diffusion layer and CL</li> <li>➤ Considering the interplay between reaction kinetics as well as other phenomena e.g. mass, charge and heat transports</li> <li>➤ Incorporating the influence of the structural parameters of the electrode, such as porosity and electrode thickness</li> <li>➤ Applicable for porous electrodes</li> </ul>

In the literature, the interface film models have been applied broadly in bioelectrochemical systems [5] and are useful for kinetic determination since they have no spatial coordinate of the CL, and disregard the structure, thickness and composition in the CL. In this approach, the zone diagram has been normally used to obtain a detailed explanation of the relationship between the parameters and to propose suitable experiments to disentangle the contributions from different parameters [5]. More detail about the modelling of electro-enzymatic systems can be found in the book chapter 8 of Bartlett presented in [5]. The distributed model has not been used widely in EESs and the distribution of charge species has

usually been neglected in the literature. Table 2-8 gives a brief summary of the interface and distributed model.

## 2.4 Finite volume method for partial differential equation

The equation system of the mathematical model (for example the dynamic balances of mass and charge) contains PDEs with non-linear bio-catalytic reaction rate terms and a complex initial/boundary conditions. These non-linear terms raise the complications in finding an appropriate solution. Two general approaches to deal with the problem have been employed: the use of approximate analytical solutions, and numerical simulation methods. The numerical solutions are usually used since analytical solutions are restricted to specific conditions. The restriction is that these numerical approaches do not provide a straightforward expression and as much insight into the behaviour of the electrode. The combination of two approaches can be more powerful, particularly for a complex situation [79]. There are several numerical methods for PDE reported in the literature in enzymatic electrode modelling i.e hopscotch method [86, 87], the orthogonal collocation method [88, 89], the relaxation method [90, 91], the finite difference (FD) method [87, 92], and the Crank–Nicholson Method [93]. The below part briefly summarizes the finite volume method (FVM) due to its popularity and simplicity. This method is specifically used to discretize PDEs to ODEs in this work.

Table 2-9: A typical PDE with IC and BCs

PDE equations	IC BCs
$\frac{\partial C(z,t)}{\partial t} = a_2 \frac{\partial}{\partial z} \left( \frac{\partial C(z,t)}{\partial z} \right) + a_1 \frac{\partial C(z,t)}{\partial z} + a_0 C(z,t) + b \quad (39)$	$C(z, t_0) = C_0(z) \quad (40)$
$t \in [t_i, t_e], z \in [z_i, z_e], a_1, a_2, a_0, b = \text{const}$	$C(z_0, t) = C_0(z) \quad (41)$
	$\frac{\partial C(z_e, t)}{\partial z} = C'_e(t) \quad (42)$

The FVM method is used to simplify a typical second order PDE (Eq. 39), in which the relevant variable changes with time and space (Table 2-9). A typical example of the above PDE in chemical process is the dynamic mass balance of chemical species considering diffusion ( $a_2=D$ ), convection ( $a_1=v$ ) and reaction kinetic ( $a_0=k$ ) terms. In this method, the calculation domain in its space variables is first discretized by dividing the space into  $n$  intervals. The following quantities are being defined in Table 2-10.

Table 2-10: Defined quantities for FVM discretization

Interval boundaries	$z_0 = z_1 < z_i < z_{i+1} = z_e$ (43)
Interval width	$\Delta z_i = z_{i+1} - z_i$ (44)
Interval midpoint, supporting point	$z_{m,i} = \frac{z_i + z_{i+1}}{2}$ (45)
Distance between supporting points	$(\delta z)_i = z_{m,i+1} - z_{m,i}$ (46)
Approximated function value at the interval midpoint	$C_i = C(z_{m,i})$ (47)

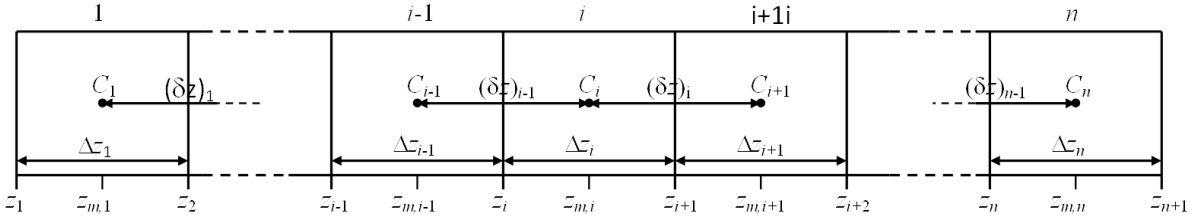


Figure 2-6 : Illustration of the discretization in the spatial domain

The interval of discretization can have the same size (equidistant) or different size. The next step would be the integration Eq. (39) over the space element. The equation of the  $i^{\text{th}}$  element is obtained as follows:

$$\underbrace{\int_{z_i}^{z_i+\Delta z_i} \frac{\partial C(z,t)}{\partial t} dz}_{T_1} = \underbrace{\int_{z_i}^{z_i+\Delta z_i} a_2 \frac{\partial}{\partial z} \left( \frac{\partial C(z,t)}{\partial z} \right) dz}_{T_2} + \underbrace{\int_{z_i}^{z_i+\Delta z_i} a_1 \frac{\partial C(z,t)}{\partial z} dz}_{T_3} + \underbrace{\int_{z_i}^{z_i+\Delta z_i} a_0 C(z,t) dz}_{T_4} + \underbrace{\int_{z_i}^{z_i+\Delta z_i} b dz}_{T_5} \quad (48)$$

The relation between supporting points  $C_i$  can be constant, linear or non-linear (i.e. polynomials). For the sake of simplicity, a simple assumption on a piecewise constant between neighboring points  $C_i$  was chosen and the time derivative of  $C$  is also a constant over the interval.

The integration of the different terms of Eq. (48) is approximated as following:

The 1<sup>st</sup> term ( $T_1$ )

$$\int_{z_i}^{z_i+\Delta z_i} \frac{\partial C}{\partial t} dz = \frac{d}{dt} \int_{z_i}^{z_i+\Delta z_i} C dz = \frac{d}{dt} [CZ]_{z_i}^{z_{i+1}} = \frac{dC_i}{dt} (z_{i+1} - z_i) = \frac{dC_i}{dt} \Delta z_i \quad (49)$$

The 2<sup>nd</sup> term ( $T_2$ )

$$\int_{z_i}^{z_i+\Delta z_i} a_2 \frac{\partial}{\partial z} \left( \frac{\partial C}{\partial z} \right) dz = a_2 \left[ \frac{\partial C}{\partial z} \right]_{z_i}^{z_i+\Delta z_i} = a_2 \left( \frac{C_{i+1} - C_i}{(\delta z)_i} - \frac{C_i - C_{i-1}}{(\delta z)_{i-1}} \right) \quad (50)$$

The 3<sup>rd</sup> term ( $T_3$ )

$$\int_{z_i}^{z_i+\Delta z_i} a_1 \frac{\partial C(z,t)}{\partial z} dz = a_1 [C]_{z_i}^{z_i+\Delta z_i} = \begin{cases} a_1 (C_i - C_{i-1}) & \text{for backward difference} \\ a_1 (C_{i+1} - C_i) & \text{for forward difference} \end{cases} \quad (51)$$

The backward option is suitable for a system with a flow in positive z-direction, whereas the second suits a flow in negative z-direction. An alternative way to approximate the first derivative is to predict the slope within the interval via the function values at the neighboring supporting points and to keep it constant over the space. Only one of all options is shown here. Between the two neighboring supporting points of the supporting point  $i$  the slope is taken from the so called central difference:

$$\left. \frac{\partial C}{\partial z} \right|_{zm,i} \approx \frac{C_{i+1} - C_{i-1}}{(\delta z)_{i-1} + (\delta z)_i} \quad (52)$$

Substituting the result into the integral we get

$$\int_{z_i}^{z_i + \Delta z_i} a_1 \frac{\partial C(z,t)}{\partial z} dz = a_1 \frac{C_{i+1} - C_{i-1}}{(\delta z)_{i-1} + (\delta z)_i} \Delta z_i \quad (53)$$

The 4<sup>th</sup> term (T<sub>4</sub>)

$$\int_{z_i}^{z_i + \Delta z_i} a_0 C dz = a_0 C_i [z_i]_{z_i}^{z_i + \Delta z_i} = a_0 C_i \Delta z_i \quad (54)$$

The 5<sup>th</sup> term (T<sub>5</sub>)

$$\int_{z_i}^{z_i + \Delta z_i} b dz = b_i \Delta z_i \quad (55)$$

Hence, from the differential equation we have deduced the discretized difference equation with the central difference:

$$\frac{dC_i}{dt} \Delta z_i = a_2 \left( \frac{C_{i+1} - C_i}{(\delta z)_i} - \frac{C_i - C_{i-1}}{(\delta z)_{i-1}} \right) + a_1 \frac{C_{i+1} - C_{i-1}}{(\delta z)_{i-1} + (\delta z)_i} \Delta z_i + a_0 C_i \Delta z_i + b_i \Delta z_i \quad (56)$$

Re-arranging Eq. (56) and in the case of a equidistant discretization:

$$\frac{dC_i}{dt} = \frac{C_{i+1} - 2C_i + C_{i-1}}{(\Delta z_i)^2} + a_1 \frac{C_{i+1} - C_{i-1}}{2\Delta z_i} + a_0 C_i + b_i \quad (57)$$

Applying the backward difference the difference equation is

$$\frac{dC_i}{dt} = a_2 \frac{C_{i+1} - 2C_i + C_{i-1}}{(\Delta z_i)^2} + a_1 \frac{C_i - C_{i-1}}{2\Delta z_i} + a_0 C_i + b_i \quad (58)$$

At the boundaries, the boundaries of the calculation domains, slightly modified equations, have to be chosen. At the left boundary at  $z_a$  a boundary condition of the first kind is given with function value  $C_0$ . Instead of  $C_{i-1}$ , which does not exist for  $i=1$ , the boundary condition has to be used. Consequently, the supporting point distance must be adjusted. The discretized equation for the first control volume is therefore expressed:

$$\frac{dC_1}{dt} = a_2 \left( \frac{C_2 - C_1}{(\Delta z_1)^2} - \frac{C_1 - C_0}{\Delta z_1 \Delta z_1 / 2} \right) + a_1 \frac{C_2 - C_0}{\Delta z_1 + \Delta z_1 / 2} + a_0 C_1 + b_1 \quad (59)$$

At the boundary on the right hand side

$$\frac{dC_n}{dt} = a_2 \left( \frac{C_n - C_{n-1}}{(\Delta z_{n-1})^2} - \frac{\partial C(z,t)}{\partial z} \Big|_{z_e} \right) + \frac{a_1}{2} \left( \frac{C_n - C_{n-1}}{(\Delta z_{n-1})} + \frac{\partial C(z,t)}{\partial z} \Big|_{z_e} \right) + a_0 C_1 + b_1 \quad (60)$$

The PDE is now spatially discretized. From one PDE a system of  $n$  ordinary differential equations which already include the boundary conditions is obtained. The detailed discretization of the initial and boundary conditions and within volume intervals are transformed as below:

$$\frac{dC_1}{dt} = \underbrace{C_0 \left( \frac{2a_2}{(\Delta z_1)^2} - \frac{2a_1}{3\Delta z_1} \right)}_{X_1} + \underbrace{C_1 \left( -\frac{a_2}{(\Delta z_1)^2} - \frac{2a_2}{(\Delta z_1)^2} + a_0 \right)}_{Y_1} + \underbrace{C_2 \left( \frac{a_2}{(\Delta z_1)^2} + \frac{2a_1}{3\Delta z_1} \right)}_{U_1} + b_1 \quad (61)$$

$$\frac{dC_i}{dt} = \underbrace{C_{i-1} \left( \frac{a_2}{(\Delta z_i)^2} - \frac{a_1}{\Delta z_i} \right)}_{X_i} + \underbrace{C_i \left( -\frac{2a_2}{(\Delta z_i)^2} - \frac{a_2}{\Delta z_i} + a_0 \right)}_{Y_i} + \underbrace{C_{i+1} \frac{a_2}{(\Delta z_i)^2}}_{U_i} + b_i \quad (62)$$

$$\frac{dC_n}{dt} = \underbrace{C_{n-1} \left( -\frac{a_2}{(\Delta z_n)^2} - \frac{a_1}{2\Delta z_n} \right)}_{X_n} + \underbrace{C_n \left( \frac{a_2}{(\Delta z_n)^2} - \frac{a_1}{2\Delta z_n} + a_0 \right)}_{Y_n} + \underbrace{\frac{\partial C(z,t)}{\partial z} \Big|_{z_e} \left( -\frac{a_2}{\Delta z_n} + \frac{a_1}{2} \right)}_{U_n} + b_1 \quad (63)$$

and in final ODE matrix form:

$$\begin{pmatrix} \frac{dC_1}{dt} \\ \vdots \\ \frac{dC_{i-1}}{dt} \\ \frac{dC_i}{dt} \\ \frac{dC_{i+1}}{dt} \\ \vdots \\ \frac{dC_n}{dt} \end{pmatrix} = \underbrace{\begin{pmatrix} Y_1 & U_1 & & & & & \\ \ddots & \ddots & \ddots & & & & 0 \\ & X_{i-1} & Y_{i-1} & U_{i-1} & & & \\ & & X_i & Y_i & U_i & & \\ & & & X_{i+1} & Y_{i+1} & U_{i+1} & \\ & 0 & & & \ddots & \ddots & \ddots \\ & & & & & Y_n & U_n \end{pmatrix}}_A \begin{pmatrix} C_1 \\ \vdots \\ C_{i-1} \\ C_i \\ C_{i+1} \\ \vdots \\ C_n \end{pmatrix} + \underbrace{\begin{pmatrix} b_1 + X_1 C_a \\ \vdots \\ C_{i-1} \\ b_i \\ b_{i+1} \\ \vdots \\ b_n + U_n C_e' \end{pmatrix}}_{b^*} \quad (64)$$

Or in short

$$\frac{dC}{dt} = AC + b^* \quad (65)$$

At the steady state condition, Eq. (65) becomes

$$0 = AC + b^* \quad (66)$$

Where  $b^*$  represents the source term being extended by the boundary conditions. The set of ODEs can be solved via a numerical method using in commercial soft-wares e.g. Matlab, Mathematica, Maple.

## 2.5 Electrochemical impedance spectroscopy

Electrochemical impedance spectroscopy (EIS) is a well-established diagnostic tool that can be used to characterize different processes and analyse the critical limitations of electrochemical systems. In this method, a small sinusoidal perturbation of an input (either current or potential) is applied and the response signal is measured (Figure 2-7). Due to the small amplitude of the perturbation (usually  $\Delta E < 8/n$  mV peak to peak [94],  $n$  being the number of electrons transferred), the system is approximated to be quasi linear in the perturbation range and the linear impedance is analysed. Classical EIS uses physically-sound equivalent circuit models in which different electrical elements, for example, resistors, capacitors and inductors are introduced to catch the physical-chemical phenomena. Within the range of the perturbation frequency, processes with different time constants can be separated; for example, Ohmic resistance at the high frequency end. One of the shortcomings of the EIS is that sometimes physically-sound equivalent circuit models for different processes can be similar under certain operating conditions [95]. Similarity of the spectra would occur if the processes have similar time constants and are therefore measured in the same frequency range. Additionally, a masking effect due to the high double layer capacity can occur. This brings difficulties in certain cases in distinguishing between for example thin film diffusion and agglomerate diffusion of oxygen at the cathode [96].

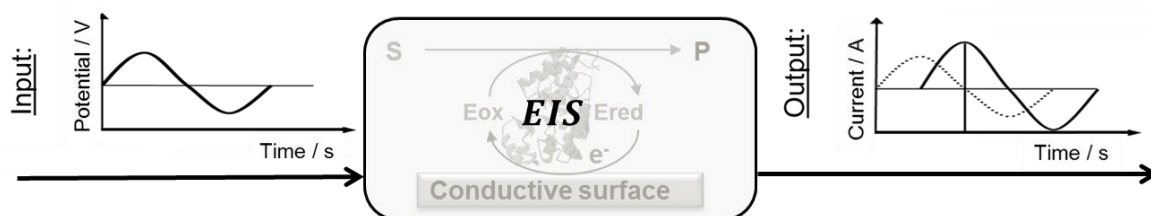


Figure 2-7: Schematic representation of the EIS methodology

The other approach to derive EIS mathematically is based on physio-chemical processes. The derivation follows the below steps:

- Definition of important processes contributing to the system performance,
- Definition of the mathematical model, including kinetic, mass/charge transport equations as well all balance equations,

- c) Definition of input and output variables,
- d) Taylor approximation of the current density and potential around the steady state value,
- e) Finding the related terms i.e concentrations oscillation in the Taylor approximation,
- f) Substitution of the input and outputs as  $Z=E/j$  to obtain the EIS expression.

The following gives a detailed EIS derivation of a Faradaic reaction in the presence of semi-infinite linear diffusion. Consider a reversible electrochemical reaction on the surface as below:



The Butler-Vomer formulation is utilized to count the change in current density on a conductive surface.

$$j(t) = nFk_0 \left( C_{Ox}(t) e^{\left[ \frac{-\alpha nF}{RT} (E - E_{r0}) \right]} - C_{Red}(t) e^{\left[ \frac{-(1-\alpha)nF}{RT} (E - E_{r0}) \right]} \right) \quad (68)$$

where  $k_0$  is the rate constant of electrochemical step,  $E_{r0}$  is the reversible potential,  $n$  is number of electron,  $\alpha$  is the transfer coefficient.

When a small perturbation of potential  $\Delta E(t) = E_0 \exp(i\omega t)$  is applied, the current density and the concentrations would oscillate around the steady state (ss) value (i.e  $j(t) = j_{ss} + \Delta j(t)$ ,  $C_{Ox}(t) = C_{Ox,ss} + \Delta C_{Ox}(t)$ ,  $C_{Red}(t) = C_{Red,ss} + \Delta C_{Red}(t)$ ). These oscillations may also be written as:  $\Delta E(t) = \tilde{E} \exp(i\omega t)$ ,  $\Delta j(t) = \tilde{j} \exp(i\omega t)$ ,  $\Delta C_{Ox}(t) = \tilde{C}_{Ox} \exp(i\omega t)$ ,  $\Delta C_{Red}(t) = \tilde{C}_{Red} \exp(i\omega t)$  where  $\tilde{E}$ ,  $\tilde{j}$ ,  $\tilde{C}_{Ox}$ ,  $\tilde{C}_{Red}$  are the phasors of the voltage, current and concentrations, respectively.

Since  $j = f(E, C_{Ox}, C_{Red})$ , the current density may be represented as an infinite Taylor series:

$$\Delta j(t) = \left( \frac{\partial j}{\partial E} \right) \Delta E(t) + \left( \frac{\partial j}{\partial C_{Ox}} \right) \Delta C_{Ox} + \left( \frac{\partial j}{\partial C_{Red}} \right) \Delta C_{Red} + \frac{1}{2} \left( \frac{\partial^2 j}{\partial E^2} \right) (\Delta E)^2 + \frac{1}{2} \left( \frac{\partial^2 j}{\partial^2 C_{Red}} \right) (\Delta C_{Red})^2 + \frac{1}{2} \left( \frac{\partial^2 j}{\partial^2 C_{Ox}} \right) (\Delta C_{Ox})^2 + \dots \quad (69)$$

As can be seen from (Eq. (69)), higher order terms appear and therefore higher harmonics analysis has also been introduced. As noticed from Eq. (68) that the current density has a linear dependence with respect to the concentrations of Ox and Red. Therefore, it is an appropriate approximation to keep only the linear terms for a small perturbation. The derivatives of (Eq. (68)) corresponding to stationary conditions may be obtained as follows

$$\frac{\partial j}{\partial E} = -n^2 \frac{F}{RT} k_0 \left( \alpha C_{Ox}(t) e^{\left[\frac{-\alpha nF}{RT}(E-E_0)\right]} + (1-\alpha) C_{Red}(t) e^{\left[\frac{-(1-\alpha)nF}{RT}(E-E_0)\right]} \right) \quad (70)$$

$$\frac{\partial j}{\partial C_{Ox}} = nF k_0 e^{\left[\frac{-\alpha nF}{RT}(E-E_0)\right]} \quad (71)$$

$$\frac{\partial j}{\partial C_{Red}} = -nF k_0 e^{\left[\frac{-(1-\alpha)nF}{RT}(E-E_0)\right]} \quad (72)$$

To find the concentrations of Red and Ox, the diffusion effect of these species should be specified as

$$\frac{\partial \Delta C_{Ox}}{\partial t} = D_{Ox} \frac{\partial^2 C_{Ox}}{\partial x^2} \quad \text{and} \quad \frac{\partial \Delta C_{Red}}{\partial t} = D_{Red} \frac{\partial^2 C_{Red}}{\partial x^2} \quad (73)$$

From the oscillation definition, one obtains

$$D_{Ox} \frac{\partial^2 \tilde{C}_{Ox}}{\partial z^2} = \tilde{C}_{Ox} i\omega \quad \text{and} \quad D_{Red} \frac{\partial^2 \tilde{C}_{Red}}{\partial z^2} = \tilde{C}_{Red} i\omega \quad (74)$$

with the boundary conditions at the surface ( $x=0$ ) and ( $z=\infty$ )

$$D_{Ox} \frac{\partial \tilde{C}_{Ox}}{\partial z} \Big|_{z=0} = -D_{Red} \frac{\partial \tilde{C}_{Red}}{\partial z} \Big|_{z=0} = \frac{j}{nF} \quad (75)$$

$$\tilde{C}_{Ox} \Big|_{x=\infty} = \tilde{C}_{Red} \Big|_{x=\infty} = 0 \quad (76)$$

It is necessary to solve the system of (Eqs. 74-76) to find the expressions of  $\tilde{C}_{Ox}$  and  $\tilde{C}_{Red}$ . These values expressions are substituted into (Eq. (69)) to obtain the final faradaic impedance

$$\hat{Z}_{Fa} = \frac{RT}{n^2 F^2} \frac{1 + k_0 e^{\left[\frac{-\alpha nF}{RT}(E-E_0)\right]} + k_0 e^{\left[\frac{-\alpha nF}{RT}(E-E_0)\right]}}{\alpha k_0 C_{Ox}(0,t) e^{\left[\frac{-\alpha nF}{RT}(E-E_0)\right]} + (1-\alpha) k_0 C_{Red}(0,t) e^{\left[\frac{-(1-\alpha)nF}{RT}(E-E_0)\right]}} \sqrt{i\omega D_{Ox}} + \sqrt{i\omega D_{Red}}} \quad (77)$$

As can be observed from (Eq. (77)), the total faradaic impedance,  $\hat{Z}_{Fa}$ , consists of three components. The first comes from the derivative of  $\frac{\partial j}{\partial E}$  and is called the charge-transfer resistance,  $R_{ct}$ , and the two others, contributed by  $\frac{\partial j}{\partial C_{Ox}}$ ,  $\frac{\partial j}{\partial C_{Red}}$ , are called impedances of mass transfer, or semi-infinite Warburg impedance  $\hat{Z}_W$ .

The other way to extract EIS is based on the frequency response function. At the small excitation value around the steady state value, the evolution of the output signal (current density) is dependent on the convolution of the time evolution of the input signal  $E(t)$  and the impulse response of the system  $g(t)$

$$\Delta j(t) = \int_{-\infty}^{+\infty} g(\tau) \Delta E(t - \tau) d\tau \quad (78)$$

where  $j$  and  $\tilde{E}$  are defined as



$$\Delta j = j - j_{ss} \text{ and } \Delta E = E - E_{ss} \quad (79)$$

In a harmonic input signal

$$\Delta E(t) = A \cos(\omega t) = \frac{A}{2}(e^{i\omega t} + e^{-i\omega t}) \quad (80)$$

It follows from (Eq. (78)) that

$$\Delta j(t) = \frac{A}{2} \left( e^{i\omega t} \underbrace{\int_{-\infty}^{\infty} g(\tau) e^{-i\omega\tau} d\tau}_{H_1(\omega)=Z^{-1}(\omega)} + e^{-i\omega t} \underbrace{\int_{-\infty}^{\infty} g(\tau) e^{i\omega\tau} d\tau}_{H_1(-\omega)=Z^{-1}(-\omega)} \right) \quad (81)$$

In (Eq. (81)),  $H_1(\omega)$  is the Fourier transformation of the impulse response. This function is also called the frequency response function of the system. It is identical to the reciprocal of the EIS ( $Z(\omega)$ ). At linear response, this method is also used to derive analytical solutions and deal with different complex models and mechanisms. The higher order of frequency response function can also be defined for a non-linear system with a larger perturbation. The derivation of the EIS from the frequency response function follows the following steps:

- a) Definition of major processes which can be influential on the system response,
- b) Definition of mathematical models including kinetic, mass/charge transport and mass balance equations,
- c) Definition of input and output variables,
- d) Taylor approximation of the reaction rate expressions around the steady state,
- e) Substitution of the Taylor polynomials into the mass balance equations,
- f) Substitution of the inputs and outputs into the equations gained in step “e” and application of harmonic probing,
- g) Solution of the equations derived in step “f”.

In the FRA, the input/output and other state variables are defined as in Table 2-11 [100] and Figure 2-7 [97-99].

**Table 2-11: Definition of input and output variables**

Variable	Definition
The theoretical input potential $\Delta E_{input}$	$\Delta E_{input}(t) = \Delta E(t) + A_{geo}R_{Ohm}\Delta j(t) \quad (82)$ <p>If <math>R_{Ohm} \rightarrow 0</math></p> $\Delta E_{input}(t) = \Delta E(t) \quad (83)$
The cosinusoidal input signal $\Delta E_{input}$	$\Delta E_{input}(t) = E_{input}(t) - E_{input,ss}$ $= A \cos \omega t = \frac{A}{2} (e^{i\omega t} + e^{-i\omega t}) \quad (84)$
The cell current $\Delta j(t)$	$\Delta j(t) = j(t) - j_{ss}(t)$ $= \frac{A}{2} (H_1(\omega) e^{i\omega t} + H_1(-\omega) e^{-i\omega t}) + \dots \quad (85)$
The electrode potential $\Delta E(t)$	$\Delta E(t) = \frac{A}{2} (H_1(\omega) e^{i\omega t} + H_1(-\omega) e^{-i\omega t}) + \dots \quad (86)$
Concentrations of all species $\Delta C_k(t)$	$\Delta C_k(t) = \frac{A}{2} (H_{1,k}(\omega) e^{i\omega t} + H_{1,k}(-\omega) e^{-i\omega t}) + \dots \quad (87)$

where  $A$  is the input amplitude,  $\Delta E$ ,  $\Delta j$  the deflections of the ‘real’ electrode potential and the cell current density from their steady state values, respectively,  $A_{geo}$  the geometrical electrode surface area,  $R_1$  is the Ohmic drop in the solution,  $H_1(\omega)$  is the 1<sup>st</sup> order FRF, and  $H_{1,k}(\omega)$  is the 1<sup>st</sup> order auxiliary FRF, and with “ $k$ ” referring to the related substances.

In this work, we use the FRA to derive the EIS. The detail derivation steps to final expressions for steady state current and theoretical electrochemical admittance (reciprocal of impedance) on a specific system is presented in section 3.6 and appendix 3.

It can be seen from above approaches that

- The input and output variables are deflected only slightly from their quasi steady state (Figure 2-7),
- In addition to the cell current density as the “main” output signal, the electrode potential (overpotential) and the concentrations of all species are defined as auxiliary outputs,
- The analytical solutions are feasible which can avoid problems with the numerical treatment (for instance, numerical stability, convergence, error).

In EESs, the EIS was demonstrated as a useful tool in analysis of the immobilization of enzymes on conductive surface. The Faradic EIS was combined with cyclic voltammetry to probe the electron-transfer resistance on a conductive material based on the accumulation of an insoluble product on the electrode conductive surface [101], and to explore electrochemical behaviour of myoglobin incorporated on multi-walled carbon nanotubes [102]. EIS was also used to characterize the immobilization of heme proteins, e.g. myoglobin, hemoglobin, and cytochrome c on the Au-colloid/Au-modified surface [103], to probe the reconstitution of apo-enzymes on cofactor-functionalized electrodes and the formation of cofactor-enzyme affinity complexes on electrodes [104]. The data evaluation in these examples was mainly phenomenological and the equivalent circuit is used in [104].

## **2.6 Model discrimination (model calibration) and parameterization**

For a studied system, different mathematical models can be proposed, depending on the assumptions made; the most plausible model should be selected for parameterization, process analysis and system prediction. A challenge in model development is that not all parameters are accessible experimentally or can be taken from the literature. In general, this challenge can be circumvented by fitting the model to the experimental data. The problems usually happened from the complicated models (e.g. a 3-D model with PDEs or a high number of fitting parameters). In these cases, the fitting is time consuming; the optimization may fall into a local minimum and provide a non-physical correct set of parameters. Therefore, it is important to extract unknown parameters experimentally in order to increase the reliability of the mathematical model.

Model fitting with experimental data is subject to optimality constraints (all related and objective functions). Qualitative and quantitative fits are commonly used as standards for model selection. The most plausible model with optimized parameters later serves as a tool for process analysis and system prediction. The optimized parameters are very important, because if they are identifiable the model can serve the purpose of supporting experimental analysis by looking deeper into the system's model details. The following equation is the least square function which is commonly used to minimize the difference of experimental and simulation data.

$$\chi^2(p) = \min \sum_{l=1}^n \left( \frac{Y_{sim}(X_l, p) - \hat{Y}_{exp}}{\sigma_l} \right)^2 \quad (88)$$

where  $\hat{Y}_{exp}$  is the experimental output and  $Y_{sim}$  is the simulated output for a set of parameters  $(p)$ ,  $\sigma_l$  is the estimated measurement error, and  $n$  is the number of points at different time intervals.

The optimization to obtain fitted parameters usually requires initial parameter values. Therefore, a careful comparison with the literature sources was first made and the parameters of comparable systems are used as input parameters in the present cases.

# 3 Mathematical modelling

## 3.1 Modelling domains and physical phenomena

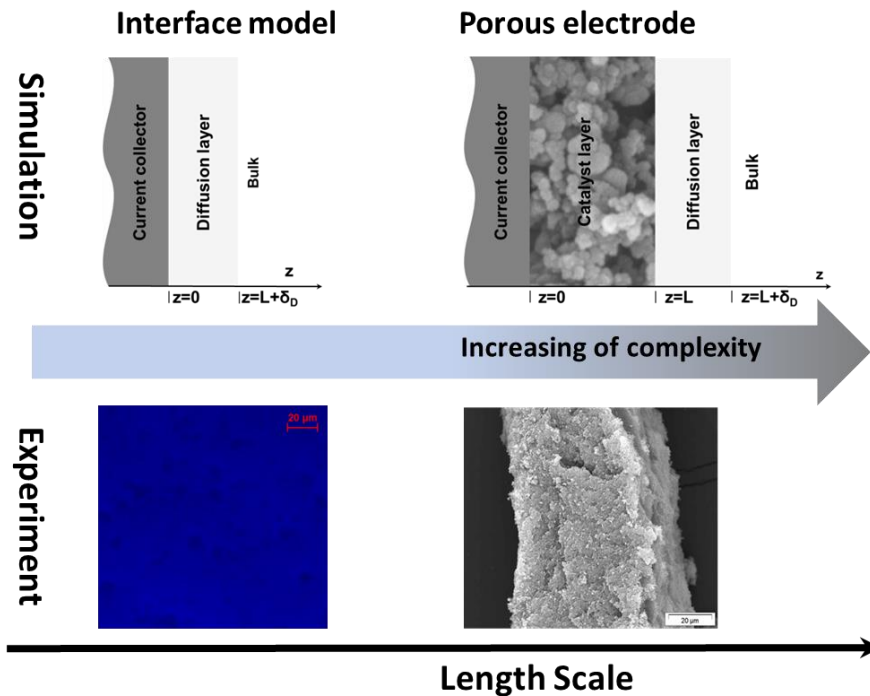


Figure 3-1: Overview of the physical modelling domain corresponding to the respective experimental setup of the thin film and the porous electrode organized by length scale

Figure 3-1 shows the physical modelling domain corresponding to the studied experimental setup of a thin film electrode and a porous enzymatic electrode organized by length scale. The complexity of mathematical modelling increases with the length scale. A reasonable physical model in each domain should be developed in order to achieve reliable parameters, and obtain better insight into the single process, as well as the interplay between the different processes. The steady state interface model and the EIS are applied for the thin film electrode while the distributed model is used in the case of the porous electrode. The systematic modelling approach is shown in Figure 1-2 (section 1), in which the development of a model from kinetics determination, model selection, and process analysis is illustrated. The first step is to obtain a quantitative and qualitative model for describing the experimental data. The selected model

with the optimized parameters is used further in the subsequent corresponding system i.e the porous electrode enzymatic cascade. The details of the modelling steps of the studied system are presented in Figure 1-3. The mathematical model equations can vary between linear PDEs, ODEs, DAEs and AEs. The PDEs appeared mostly in porous electrode models and were discretised to ODE using the finite volume method (FVM). The analytical solution of the proposed models can be derived for the interface models, i.e. steady state and EIS. The solution to the ODE equations was performed and obtained in Matlab® using the inbuilt commands ode45 and ode15s.

### **3.2 Facts and main assumptions**

This section presents the global assumptions applied in this work. The additional assumptions for each selected system are specified accordingly in each section.

- a) A quasi-steady state approximation is applied for the charge balance equations of the ionic conducting phase and electron conducting phase. This assumption is well justified, bearing in mind that the ion-conducting phase can reach the local electro-neutrality condition (for a binary mixture) and the electron transfer process in the electron conducting phase is relatively fast compared to the time constants of other processes (diffusion, enzymatic and electrochemical reactions) [105].
- b) Enzymes, mediators and supporters (Vulcan, binders) are assumed to be uniformly distributed on the conductive surface and throughout the porous matrix. The total amount of nominal enzyme remains constant in the CL during the simulation/experimental course. These assumptions were reported in [105] and allow us to directly argue the utilization factor of related species or the comparison of different cases.
- c) In the case of DET, enzyme activity is not influenced by the distance/orientation of redox centre(s) to a conductive surface.
- d) All reactions only take place in the CL or at the interface of the electron conducting phase and ionic conducting phase.
- e) The kinetic constants of the enzymatic and electrochemical steps are unaffected by the electrode structural parameters.

- f) Upon an immobilization procedure using the same prepared catalyst ink, the porosity of the enzymatic electrodes remains constant.
- g) The system is isothermal.
- h) For the interface electrode, the roughness factor is not taken into account.
- i) The species concentrations in the bulk are constant. The bulk solution distant from the electrode remains well-stirred by the convection induced by rotation in a rotating disc electrode system.
- j) In addition, no chemical or electrochemical reaction takes place in the DL or bulk solution, but only at the electrode surface. We also assume in the presence of sufficient supporting electrolytes that migration can be neglected.
- k) For the BCs, the concentration adjacent to the bulk solution is usually known and no flux leaves the CL or the current collector ( $z=0$ ).

The following sections present the mathematical model of each selected system (as demonstrated in Figure 1-3). The workflow is shown in the sequence that parameters from previous system are extracted and used for the next system.

### 3.3 Enzymatic anode

As presented in Figure 3-1, the mathematical modelling approach should start with the thin film electrode, with the porous electrode following in the next step. This corresponds, however, more to the DET electrodes due to the possibility in designing a very thin film electrode. In the anode side employing GOx and the mediator TTF immobilized in a porous matrix, the thin film electrode becomes challenging. In addition, as can be seen in Figure 1-3 (section 1), some of the parameters from the anode side are applied further in the cathode side. Therefore, the porous mathematical model is first applied to the GOx-TTF electrode. The MET system was selected due to the broad applications of GOx in different bioelectrochemical systems (i.e biosensors, EFCs, electro-enzymatic reactors). GOx is well known as a MET enzyme; therefore, different mediators have been reported in the literature for GOx i.e CTC, TTF, and TCNQ [65], benzyl viologen, and methylene blue [106-107], ferrocenecarboxaldehyde, and ferrocenemethanol [27,104]. Among these, TTF was reported as having negligible electron conductivity and it is usually integrated into the electron conductive matrix or combined with

tetracyanoquinodimethane (TCNQ) [108-109]. These combinations provide a porous electrode with high performance.

The mathematical equations are formulated in the porous electrode for two modelling domains, namely the CL and DL (Figure 3-1). Diffusion is governed in the DL, while the CL is controlled by charge transfer, reactions, and species transport. The detailed features of CL are presented in section 2.2.1. The main assumptions presented in section 3.2 are applied and the following additional assumptions are made:

- The so-called two-substrate ping-pong mechanism is applied to define the reaction kinetics of the MET system [7,110-112]. The intermediate step, forming an enzyme substrate complex, was neglected. This assumption has been widely used in the literature to describe the reaction steps of the enzyme-mediator reaction system and can reduce the number of fitted kinetic parameters. The assumption is well justified under steady state operation.
- $\text{TTF}^+$ , after dissolving electrochemically at the interface of the electron conducting phase, can move freely in CL and DL. The experimental evidence, i.e using a quartz crystal microbalance, has been justified well for this assumption [113-115].
- The accumulation of  $\text{TTF}^+$  in the bulk solution during the experimental course is neglected. To validate this assumption, nuclear magnetic resonance (NMR) spectroscopy analysis was used to analyse the TTF compounds in the remaining solution after 7 hours of operation at potential 0.3844 vs. SHE /V. As a result, no TTF compounds were detected [20].

The following parts show the balance equations for potential fields in the electron- and ionic-conducting phases in the CL and DL (Table 3-1). The mass balances of all related substances for each case study are then presented. Model reduction of the full 1-D model to a reduced 1-D model has been performed. This step is essential to justify the necessity of the distributed model in describing the behaviour of the porous electrode. The main goal of the work in this section is to obtain more insight into the interplay between enzymatic, mediator kinetics and mass-transfer processes inside the porous electrode structure and to point out the major limitations under different operating conditions using the mathematical model.



### 3.3.1 Potential field- charge balance

The charge balance for the electron conductor, the ion conductor and the interface inside the CL and DL are presented in Table 3-1 [76, 116-117].

Table 3-1: Mathematical equations of charge balances inside the CL and DL

Charge balance	Mathematical equation	BCs
electron conductor $\phi_E^{CL}(z, t)$	$0 = \frac{\partial}{\partial z} \left( \kappa_E^{CL} \frac{\partial \phi_E^{CL}(z, t)}{\partial z} \right) + a \iota(z, t) \quad (89)$	<ul style="list-style-type: none"> <li>• <math>\kappa_E^{CL} \frac{\partial \phi_E^{CL}(z, t)}{\partial z} \Big _{z=L} = 0 \quad (90)</math></li> <li>• <math>\phi_E^{CL}(0, t) = \phi_E^{LB}(t) \quad (91)</math></li> </ul>
ionic conductor $\phi_I^{CL}(z, t)$ $\phi_I^{DL}(z, t)$	<p>in CL:</p> $0 = \frac{\partial}{\partial z} \left( \kappa_I^{CL} \frac{\partial \phi_I^{CL}(z, t)}{\partial z} \right) - a \iota(z, t) \quad (92)$ <p>In DL:</p> $0 = \frac{\partial}{\partial z} \left( \kappa_I^{DL} \frac{\partial \phi_I^{DL}(z, t)}{\partial z} \right) \quad (93)$	<ul style="list-style-type: none"> <li>• <math>\kappa_I^{CL} \frac{\partial \phi_I^{CL}(z, t)}{\partial z} \Big _{z=0} = 0 \quad (94)</math></li> <li>• <math>\phi_I^{CL}(L^-, t) = \phi_I^{DL}(L^-, t) \quad (95)</math></li> <li>• <math>\kappa_I^{CL} \frac{\partial \phi_I^{CL}(z, t)}{\partial z} \Big _{z=L^-} =</math></li> <li style="text-align: right;"><math>\kappa_I^{DL} \frac{\partial \phi_I^{DL}(z, t)}{\partial z} \Big _{z=L^+} \quad (96)</math></li> <li>• <math>\phi_I^{DL}(L + \delta_i, t) = \phi_I^{RB}(t) \quad (97)</math></li> </ul>
at the interface $E(z, t)$ $= \phi_E^{CL}(z, t) - \phi_I^{CL}(z, t)$	$C_{dl} \frac{\partial E(z, t)}{\partial z} = \iota(z, t) - nFr_e(z, t) \quad (98)$	

where “ $\kappa_i$ ”  $i=E, I$  refer to conductivities of electron- and ion- conducting phases, “ $\iota$ ” to local current density and “ $a$ ” to the internal active surface area

### 3.3.2 A single substrate

Figure 3-2 shows the schematic representation of the reaction mechanism of glucose ( $S_2$ ) oxidation using GOx ( $E_{2ox}$ ) as a biocatalyst in the presence of TTF as a mediator in a porous conductive matrix (using Vulcan). The detailed reaction steps are listed in Table 3-2. The first step in the reaction mechanism is substrate diffusion from the bulk to the CL (Eq. (99)). In the CL enzyme ( $E_{2ox}$ ) reacts with glucose ( $S_2$ ) forming the reduced form of enzyme ( $E_{2red}$ ) and the product (gluconolactone). This reaction step follows the lumped kinetic description (Eq. (100)). In the next step the oxidized form of enzyme is regenerated by an oxidized mediator ( $M_{ox}$ ) (Eq. 101). The oxidized form of the mediator ( $M_{ox}$ ) is then electrochemically regenerated by the electron donation steps of the reduced mediator ( $M_{red}$ ) on a conductive surface. The oxidized mediator ( $M_{ox}$ ) can be utilized again for the enzyme regeneration (Eq. (101)) and might diffuse

to a bulk solution. In the literature,  $M_{ox}$  can even be oxidized further [114-115]. In this work, the diffusion of  $M_{ox}$  out of CL is considered and the applied potential is restricted to the range of [-0.2, 0.2]/V vs. SCE to minimize the further oxidation of TTF.

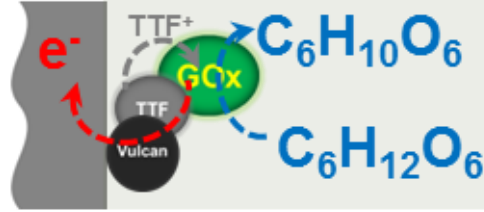


**Figure 3-2: Schematic representation of the reaction mechanism of the glucose oxidation using GOx - TTF in a porous conductive matrix**

The necessary general equations of the system are charge balances and mass balances combined with kinetics. The mathematical expressions of the charge balances are presented in section 3.4.1; the following is the detail of the reaction mechanism, reaction rates and mass balances of all the related species.

**Table 3-2: Reaction mechanism and reaction rate of GOx-TTF in the presence of glucose**

Reaction mechanism	Reaction rate expressions
$S_2^{bulk} \xrightleftharpoons{D_{S_2}^{DL}} S_2^{DL} \xrightleftharpoons{D_{S_2}^{CL}} S_2$ (99)	$r_{11}(z, t) = K_{11} C_{S_2}^{CL}(z, t) C_{E_{2ox}}(z, t)$ (104)
$E_{2ox} + S_2 \xrightleftharpoons{K_{11}} P + E_{2red}$ (100)	$r_{22}(z, t) = K_{22} C_{Mox}(z, t) C_{E_{2red}}(z, t)$ (105)
$E_{2red} + 2M_{ox} \xrightleftharpoons{K_{22}} E_{2ox} + 2M_{red} + 2H^+$ (101)	$r_e(z, t) =$
$M_{red} \xrightleftharpoons{k_{e0}} M_{ox} + e^-$ (102)	$k_{e0} [C_{Mred}(z, t) e^{\alpha F(E(z,t)-E_r)/(RT)} -$ $C_{Mox}(z, t) e^{-(1-\alpha)(E(z,t)-E_r)F/(RT)}]$ (106)
$M_{ox} \xrightleftharpoons{D_{Mox}^{CL}} (M_{ox})^{CL} \xrightleftharpoons{D_{Mox}} (M_{ox})^{bulk}$ (103)	$E(z, t) = E_{applied}(z, t) - j(t) A_{geo} R_{\Omega}$ (107)

In the reaction mechanism  $M_{red}$  stands for TTF and  $M_{ox}$  for TTF<sup>+</sup>,  $S_2$  for glucose,  $E_{2red}$  for reduced enzyme,  $E_{2ox}$  for oxidized enzyme,  $P$  for product. In the reaction rate expression:  $C_{E_{2v}}$ ,  $C_{E_{2ox}}$ ,  $C_{Mv}$ ,  $C_{Mox}$ ,  $C_{E_{2red}}$  are the total active enzyme, oxidized enzyme, active mediator, oxidized mediator and reduced enzyme concentration respectively,  $A_{geo}$  for the geometrical surface area of the working electrode.

In order to quantify the influence of  $M_{ox}$  diffusion out of CL, two model variants are proposed and presented in Table 3-3. The full model (FM1) considers the diffusion of the oxidized form of the mediator out of CL while the second one neglects this influence.

**Table 3-3: Model variants of the MET(GOx-TTF) system**

Model variants	Eqs.
FM1(including mass transport of the oxidized mediator)	96-103, $D_{Mox} \neq 0$
FM2(without including mass transport of the oxidized mediator)	96-99, 101-102, $D_{Mox} = 0$

**Table 3-4: Mass balance of all related species of the system: glucose oxidation using GOx -TTF in a porous conductive matrix [117]**

Mass Balance	Mathematical equation	BCs
substrate S	<p>In CL</p> $\varepsilon \frac{\partial C_{S_2}^{CL}(z,t)}{\partial t} = \frac{\partial}{\partial z} \left( D_{S_2}^{CL} \frac{\partial C_{S_2}^{CL}(z,t)}{\partial z} \right) - r_{11}(z,t) \quad (108)$ <p>In DL</p> $\frac{\partial C_{S_2}^{DL}(z,t)}{\partial t} = \frac{\partial}{\partial z} \left( D_{S_2}^{DL} \frac{\partial C_{S_2}^{DL}(z,t)}{\partial z} \right) \quad (109)$	<ul style="list-style-type: none"> <li>• <math>D_{S_2}^{CL} \frac{\partial C_{S_2}^{CL}(z,t)}{\partial z} \Big _{z=0} = 0 \quad (110)</math></li> <li>• <math>C_{S_2}^{DL}(z = L + \delta_{S_2}, t) = C_{S_2}^{bulk}(t) \quad (111)</math></li> <li>• <math>-D_{S_2}^{CL} \frac{\partial C_{S_2}^{CL}(z,t)}{\partial z} \Big _{z=L^-} =</math></li> <li style="padding-left: 2em;"><math>-D_{S_2}^{DL} \frac{\partial C_{S_2}^{DL}(z,t)}{\partial z} \Big _{z=L^+} \quad (112)</math></li> <li>• <math>C_{S_2}^{CL}(L^-, t) = C_{S_2}^{DL}(L^+, t) \quad (113)</math></li> </ul>
oxidized mediator $M_{Ox}$	<p>In CL</p> $\varepsilon \frac{\partial C_{M_{Ox}}^{CL}(z,t)}{\partial t} = \frac{\partial}{\partial z} \left( D_{M_{Ox}}^{CL} \frac{\partial C_{M_{Ox}}^{CL}(z,t)}{\partial z} \right) + ar_e(z,t) - 2r_{22}(z,t) \quad (114)$ <p>In DL</p> $\frac{\partial C_{M_{Ox}}^{DL}(z,t)}{\partial t} = \frac{\partial}{\partial z} \left( D_{M_{Ox}}^{DL} \frac{\partial C_{M_{Ox}}^{DL}(z,t)}{\partial z} \right) \quad (115)$	<ul style="list-style-type: none"> <li>• <math>D_{M_{Ox}}^{CL} \frac{\partial C_{M_{Ox}}^{CL}(z,t)}{\partial z} \Big _{z=0} = 0 \quad (116)</math></li> <li>• <math>C_{M_{Ox}}^{DL}(z = L + \delta_{M_{Ox}}, t) = 0 \quad (117)</math></li> <li>• <math>-D_{M_{Ox}}^{CL} \frac{\partial C_{M_{Ox}}^{CL}(z,t)}{\partial z} \Big _{z=L^-} =</math></li> <li style="padding-left: 2em;"><math>-D_{M_{Ox}}^{DL} \frac{\partial C_{M_{Ox}}^{DL}(z,t)}{\partial z} \Big _{z=L^+} \quad (118)</math></li> <li>• <math>C_{M_{Ox}}^{CL}(L^-, t) = C_{M_{Ox}}^{DL}(L^+, t) \quad (119)</math></li> </ul>
reduced form of enzyme $E_{red}$	$\frac{\partial C_{E_{2red}}(z,t)}{\partial t} = r_{11}(z,t) - r_{22}(z,t) \quad (120)$	
conservation of total mediator and enzyme concentration	$C_{Mt}(z,t) = C_{Mred}(z,t) + C_{Mox}(z,t) \quad (121)$	
	$C_{E_{2t}}(z,t) = C_{E_{2red}}(z,t) + C_{E_{2ox}}(z,t) \quad (122)$	

The reaction rates appearing in Table 3-4 are presented in Table 3-2

### 3.3.3 Competitive substrates

The glucose oxidation on the enzymatic electrode using GOx-TTF is presented in Figure 3-3. Glucose is popularly used as a fuel for the anode of a bio-FC system and is an essential substance for the human metabolism [7]. It can make the application of EES miniaturization as a power source in the human body feasible. However, the presence of  $O_2$  in the system may create a negative impact on the utilization of enzymes in the oxidation process due to its high reactivity to GOx. In the catalytic cycle of GOx,  $O_2$  as a natural electron acceptor participates in the regeneration steps of GOx to produce an intermediate  $H_2O_2$  ( $S_1$ ) [20, 118-119]. The presence of  $H_2O_2$  can be an inhibitor to GOx due to the reaction with the reduced form of GOx ( $E_{2ox}$ ) forming an irreversible inhibition substance ( $E_{2I}$ ) [120-121] and it can oxidise other components inside the electrode structure [20]. All of these drawbacks can consequently cause a decrease in anodic current density. In the study framework, the kinetics of the system is limited in some certain steps and is shown in Table 3-5.

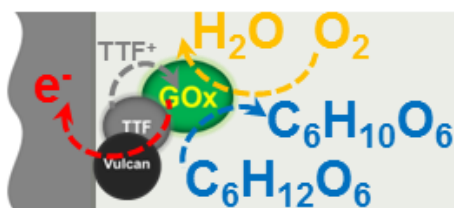


Figure 3-3: Schematic representation of the reaction mechanism of the glucose oxidation using GOx -TTF in a porous conductive matrix with additional oxygen supply

**Table 3-5: Detailed reaction mechanism and rate expression of the system: glucose oxidation using GOx - TTF in a porous conductive matrix with additional O<sub>2</sub> supply**

Reaction mechanism	Reaction rate expressions
$O_2^{bulk} \xrightarrow{D_{S_2}^{DL}} O_2^{DL} \xrightarrow{D_{S_2}^{CL}} O_2$ (123)	$r_{11}(z, t) = K_{11} C_{S_2}^{CL}(z, t) C_{E_{2ox}}(z, t)$ (131)
$S_2^{bulk} \xrightarrow{D_{S_2}^{DL}} S_2^{DL} \xrightarrow{D_{S_2}^{CL}} S_2$ (124)	$r_{22}(z, t) = K_{22} C_{Mox}(z, t) C_{E_{2red}}(z, t)$ (132)
$E_{2ox} + S_2 \xrightarrow{K_{11}} P + E_{2red}$ (125)	$r_{33}(z, t) = K_{33} C_{O_2}(z, t) C_{E_{2red}}(z, t)$ (133)
$E_{2red} + O_2 \xrightarrow{K_{33}} S_1 + E_{2ox}$ (126)	$r_{44}(z, t) = K_{44} C_{S_1}(z, t) C_{E_{2red}}(z, t)$ (134)
$E_{2red} + S_1 \xrightarrow{K_{44}} E_2I$ (127)	$r_e(z, t) = k_{e0} [C_{Mred}(z, t) e^{\alpha F(E(z,t)-E_r)/(RT)} - C_{Mox}(z, t) e^{-(1-\alpha)(E(z,t)-E_r)F/(RT)}]$ (135)
$E_{2red} + 2M_{ox} \xrightarrow{K_{22}} E_{2ox} + 2M_{red} + 2H^+$ (128)	$E(z, t) = E_{applied}(z, t) - j(t) A_{geo} R_{\Omega}$ (136)
$M_{red} \xrightleftharpoons{k_{e0}} M_{ox} + e^-$ (129)	
$M_{ox} \xrightarrow{D_{Mox}^{CL}} (M_{ox})^{CL} \xrightarrow{D_{Mox}} (M_{ox})^{bulk}$ (130)	

The mass balance of related species is shown in Table 3-6.

Table 3-6: Mass balance of related species of the system: glucose oxidation using GOx -TTF in a porous conductive matrix with additional O<sub>2</sub> supply

Mass Balance	Mathematical equation	BCs
substrate S <sub>2</sub>	In CL $\varepsilon \frac{\partial C_{S_2}^{CL}(z,t)}{\partial t} = \frac{\partial}{\partial z} \left( D_{S_2}^{CL} \frac{\partial C_{S_2}^{CL}(z,t)}{\partial z} \right) - r_{11}(z,t) \quad (137)$	<ul style="list-style-type: none"> <li>• <math>D_{S_2}^{CL} \frac{\partial C_{S_2}^{CL}(z,t)}{\partial z} \Big _{z=0} = 0 \quad (139)</math></li> <li>• <math>C_{S_2}^{DL}(z = L + \delta_{S_2}, t) = C_{S_2}^{bulk}(t) \quad (140)</math></li> </ul>
	In DL $\frac{\partial C_{S_2}^{DL}(z,t)}{\partial t} = \frac{\partial}{\partial z} \left( D_{S_2}^{DL} \frac{\partial C_{S_2}^{DL}(z,t)}{\partial z} \right) \quad (138)$	<ul style="list-style-type: none"> <li>• <math>-D_{S_2}^{CL} \frac{\partial C_{S_2}^{CL}(z,t)}{\partial z} \Big _{z=L^-} =</math></li> <li style="padding-left: 2em;"><math>-D_{S_2}^{DL} \frac{\partial C_{S_2}^{DL}(z,t)}{\partial z} \Big _{z=L^+} \quad (141)</math></li> <li>• <math>C_{S_2}^{CL}(L^-, t) = C_{S_2}^{DL}(L^+, t) \quad (142)</math></li> </ul>
oxidized mediator M <sub>Ox</sub>	In CL $\varepsilon \frac{\partial C_{Mox}^{CL}(z,t)}{\partial t} = \frac{\partial}{\partial z} \left( D_{Mox}^{CL} \frac{\partial C_{Mox}^{CL}(z,t)}{\partial z} \right) + ar_e(z,t) - 2r_{22}(z,t) \quad (143)$	<ul style="list-style-type: none"> <li>• <math>D_{Mox}^{CL} \frac{\partial C_{Mox}^{CL}(z,t)}{\partial z} \Big _{z=0} = 0 \quad (145)</math></li> <li>• <math>C_{Mox}^{DL}(z = L + \delta_{Mox}, t) = 0 \quad (146)</math></li> </ul>
	In DL $\frac{\partial C_{Mox}^{DL}(z,t)}{\partial t} = \frac{\partial}{\partial z} \left( D_{Mox}^{DL} \frac{\partial C_{Mox}^{DL}(z,t)}{\partial z} \right) \quad (144)$	<ul style="list-style-type: none"> <li>• <math>-D_{Mox}^{CL} \frac{\partial C_{Mox}^{CL}(z,t)}{\partial z} \Big _{z=L^-} =</math></li> <li style="padding-left: 2em;"><math>-D_{Mox}^{DL} \frac{\partial C_{Mox}^{DL}(z,t)}{\partial z} \Big _{z=L^+} \quad (147)</math></li> <li>• <math>C_{Mox}^{CL}(L^-, t) = C_{Mox}^{DL}(L^+, t) \quad (148)</math></li> </ul>
O <sub>2</sub>	In CL $\varepsilon \frac{\partial C_{O_2}^{CL}(z,t)}{\partial t} = \frac{\partial}{\partial z} \left( D_{O_2}^{CL} \frac{\partial C_{O_2}^{CL}(z,t)}{\partial z} \right) - 2r_{33}(z,t) \quad (149)$	<ul style="list-style-type: none"> <li>• <math>D_{O_2}^{CL} \frac{\partial C_{O_2}^{CL}(z,t)}{\partial z} \Big _{z=0} = 0 \quad (151)</math></li> <li>• <math>C_{O_2}^{DL}(z = L + \delta_{O_2}, t) = C_{O_2}^{bulk} \quad (152)</math></li> </ul>
	In DL $\frac{\partial C_{O_2}^{DL}(z,t)}{\partial t} = \frac{\partial}{\partial z} \left( D_{O_2}^{DL} \frac{\partial C_{O_2}^{DL}(z,t)}{\partial z} \right) \quad (150)$	<ul style="list-style-type: none"> <li>• <math>-D_{O_2}^{CL} \frac{\partial C_{O_2}^{CL}(z,t)}{\partial z} \Big _{z=L^-} =</math></li> <li style="padding-left: 2em;"><math>-D_{O_2}^{DL} \frac{\partial C_{O_2}^{DL}(z,t)}{\partial z} \Big _{z=L^+} \quad (153)</math></li> <li>• <math>C_{O_2}^{CL}(L^-, t) = C_{O_2}^{DL}(L^+, t) \quad (154)</math></li> </ul>
reduced form of enzyme E <sub>2red</sub>	$\frac{\partial C_{E2red}(z,t)}{\partial t} = r_{11}(z,t) - r_{22}(z,t) - r_{33}(z,t) - r_{44}(z,t) \quad (155)$	
oxidized form of enzyme E <sub>2ox</sub>	$\frac{\partial C_{E2ox}(z,t)}{\partial t} = -r_{11}(z,t) + r_{22}(z,t) + r_{33}(z,t) \quad (156)$	
Conservation of total mediator and enzyme concentration	$C_{Mt}(z,t) = C_{Mred}(z,t) + C_{Mox}(z,t) \quad (157)$	
	$C_{E2t} = C_{E2red}(z,t) + C_{E2ox}(z,t) + C_{E2l}(z,t) \quad (158)$	

The reaction rates appearing in Table 3-6 are presented in Table 3-5. To analyse the contribution of the inhibition effect from  $H_2O_2$  on the reduced form of GOx at the studied conditions, two model variants are also made with details shown in Table 3-7.

**Table 3-7: Model variant of MET (GOx-TTF) system with  $O_2$  supply**

Variants	Characteristic
With inhibition step	$r_{44} \neq 0$
Without inhibition step	$r_{44} = 0$ and Eq. (134) is excluded

### 3.4 Enzymatic cathode

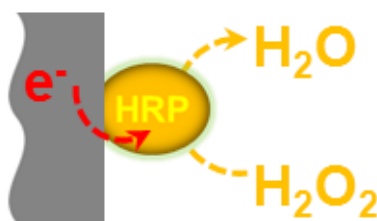


**Figure 3-4: Schematic representation of electro-enzymatic reaction of HRP on a conductive surface in the presence of hydrogen peroxide ( $H_2O_2$ )**

In the cathode,  $H_2O_2$  can be employed as an oxidant. The reduction process is catalysed by enzyme horseradish peroxidase (HRP) [122-123]. The system is applied broadly in biosensors and chemical production system. The reaction mechanism of HRP with  $H_2O_2$  on a conductive surface has been studied in the literature since 1979 [124]; the majority of the studies have focused on finding the detailed DET mechanism of this enzyme on different materials [125-128]. The general reaction mechanism is represented in the Table 3-8 and Figure 3-4 in according to literature findings. According to the scheme in Figure 3-4, HRP reacts initially with the substrate diffused from the DL forming an enzyme substrate complex ( $E_1S_1$ ) (Eq. (162)). The complex is decomposed further to compound I (CPI) (Eq. (162)) which is then electrochemically reduced in the presence of proton  $H^+$  giving compound II (CPII) (Eq. (164)). The initial state of HRP is regenerated by an electrochemical step followed by  $H^+$  incorporation (Eq. (165)). The two electrochemical steps can also be lumped as shown in Eq. (166).

**Table 3-8: Detailed reaction mechanism and reaction rate expression of HRP on a conductive surface**

Reaction mechanism	Reaction rate expressions
$S_{1,bulk} \xrightarrow{D_{S_1}^{DL}} S_1$ (159)	$r_{a1}(z, t) = k_{a1}C_{HA}(z, t)$ (167)
$HA \xrightleftharpoons{k_{a1}/k_{-a1}} H^+ + A^-$ (160)	$r_{-a1}(z, t) = k_{-a1}C_{A^-}(z, t)C_{H^+}(z, t)$ (168)
$H_0^+ \xrightarrow{D_{H^+}} H^+$ (161)	$r_1(z, t) = k_1\Gamma_{E_{1,red}}(z, t)C_{S_1}(z, t)$ (169)
	$r_{-1}(z, t) = k_{-1}\Gamma_{E_1S_1}(z, t)$ (170)
	Or
$S_1 + E_{1red} \xrightleftharpoons{k_1/k_{-1}} E_1S_1 \xrightarrow{k_{cat}} CPI + H_2O$ (162)	$r_1(z, t) = K_1\Gamma_{E_{1,red}}(z, t)C_{S_1}(z, t)$ (171)
	$r_{cat}(z, t) = k_{cat}\Gamma_{E_1S_1}(z, t)$ (172)
	Or
$S_1 + E_{1red} \xrightarrow{K_1} CPI + H_2O$ (163)	$r_{e1}(z, t) = -k_{e1}e^{\left(-\frac{\alpha_1 F}{RT}\eta_1(z,t)\right)}\Gamma_{CPI}(z, t)C_{H^+}(z, t)$ (173)
$CPI + H^+ + e^- \xrightarrow{k_{e1}} CPII$ (164)	$r_{e2}(z, t) = -k_{e2}e^{\left(-\frac{\alpha_2 F}{RT}\eta_2(z,t)\right)}\Gamma_{CPII}(z, t)C_{H^+}(z, t)$ (174)
$CPII + H^+ + e^- \xrightarrow{k_{e2}} E_{1red} + H_2O$ (165)	
	or
Or the electrochemical steps can be lumped as:	$r_e(z, t) = -k_e e^{\left(-\frac{\alpha_2 F}{RT}\eta(z,t)\right)}\Gamma_{CPI}(z, t)C_{H^+}(z, t)$ (175)
$CPI + 2H^+ + 2e^- \xrightarrow{k_e} E_{1red} + H_2O$ (166)	Where
	$\eta_1(z, t) = E(z, t) - E_{r,1}$ (176)
	$\eta_2(z, t) = E(z, t) - E_{r,2}$ (177)

$S_1$  refers to substrate ( $H_2O_2$ ),  $E_{1red}$  to the native form of HRP,  $E_1S_1$  to the enzyme substrate complex, CPI- CPII to compound I (CPI), and compound II (CPII) respectively, HA to  $H_3PO_4$  and  $A^-$  to  $[H_2PO_4]^-$ .

In the HRP catalytic cycle reported in the literature, the inhibition effects are more pronounced at higher concentrations of  $H_2O_2$  (e.g higher than 500  $\mu M$ ) and longer experimental exposure time [129, 125]. These influences tend to decrease the number of active enzymes and the current output. For the sake of simplicity, these effects are expected to be minimized in order to reduce the reaction steps and the number of optimized parameters. Therefore, the lower concentration range and shorter experimental course are controlled.

The description of the reaction rate of the electrochemical steps is also shown in Table 3-8. The kinetics of the electrochemical steps is formulated using BV formalism. As can be seen in the Eqs. (173, 174, and 175), the total electrochemical reaction rate has a negative sign '-'. This reaction rate is the net result of two opposite reactions occurring simultaneously at the



electrode surface. Since HRP behaves experimentally as a “one way enzyme” and the recordable catalytic currents appear at over-potentials of ca. -200 mV, the oxidation step was neglected. The dependence of enzyme orientation at the electrode surface and the heterogeneous rate constants dispersion on the electron transfer rate was also neglected. As a consequence, there is only the effective heterogeneous rate constant used in the system.

Protons dissociated from HA were also involved in the reaction rate of the electrochemical steps in accordance with power law kinetics (Table 3-8) which has to date been neglected in most mathematical models in the literature. This relation was experimentally proven as being importance and it was taken as an indication of the proton involvement in the charge transfer step [130]. In the reaction rate,  $\alpha_1$  and  $\alpha_2$  are transfer coefficients of two electrochemical steps, which in the present case are assumed to be identical and therefore presented as one effective  $\alpha$  value. The over-potential of the two electrochemical steps  $\eta_1$  and  $\eta_2$  are also assumed to be similar (only one effective over-potential).

The following section first illustrates the mass balance of an interface model to determine the reaction mechanism and optimized parameters. This approach is more suitable for kinetic determination due to the less significant contribution of other processes to the system performance. The interface model can be considered as an approximation of the reduced porous model in the case of no transport limitation inside the CL. The model is then integrated into the distributed model describing the porous electrode.

### 3.4.1 Interface model

#### 3.4.1.1 Mass balance equations

The modelling domain of a surface electrode is shown in Figure 3-1. The mass balances of substrate ( $S_1$ ) and proton ( $H^+$ ) in the DL are formulated and presented in Table 3-9.

Table 3-9: Mass balances of all related species on the thin film electrode using HRP in the presence of  $H_2O_2$

Mass Balance	Mathematical equation	BC2
For $S_1$ in DL	$\frac{\partial C_{S_1}(z,t)}{\partial t} = D_{S_1}^{DL} \frac{\partial}{\partial z} \left( \frac{\partial C_{S_1}(z,t)}{\partial z} \right) \quad (178)$	<ul style="list-style-type: none"> <li>• <math>D_{S_1}^{DL} \frac{\partial C_{S_1}(z,t)}{\partial z} \Big _{z=0} = r_1(0,t) \quad (179)</math></li> <li>• <math>C_{S_1}(\delta_{D,S_1}, t) = C_{S_1, bulk} \quad (180)</math></li> </ul>
For proton $H^+$	$\frac{\partial C_{H^+}(z,t)}{\partial t} = D_{H^+}^{DL} \frac{\partial}{\partial z} \left( \frac{\partial C_{H^+}(z,t)}{\partial z} \right) + k_{a1} C_{HA}(z,t) - k_{a-1} C_{A^-}(z,t) C_{H^+}(z,t) \quad (181)$	<ul style="list-style-type: none"> <li>• <math>D_{H^+}^{DL} \frac{\partial C_{H^+}(z,t)}{\partial z} \Big _{z=0} = -(r_{e1}(0,t) + r_{e2}(0,t)) \quad (182)</math></li> <li>• <math>C_{H^+}^{DL}(z = \delta_{H^+}, t) = C_{H^+}^{bulk}(t) \quad (183)</math></li> </ul>
For enzyme substrate	$\frac{d\Gamma_{E_1S_1}(0,t)}{dt} = r_1(0,t) - r_2(0,t) \quad (184)$	
For compound I	$\frac{d\Gamma_{CPI}(0,t)}{dt} = r_2(0,t) -  r_{e1}(0,t)  \quad (185)$	
For compound II	$\frac{d\Gamma_{CPII}(0,t)}{dt} =  r_{e1}(0,t)  -  r_{e2}(0,t)  \quad (186)$	
Enzyme conservation	$\Gamma_{E_1t}(0,t) = \Gamma_{E_1S_1}(0,t) + \Gamma_{CPI}(0,t) + \Gamma_{CPII}(0,t) \quad (187)$	

The reaction rates appearing in Table 3-9 are presented in Table 3-8.

To complete the interface model, the charge balance at the electrode surface is formulated:

$$C_{dl} \frac{dE(0,t)}{dt} = j(0,t) - F(r_{e1}(0,t) + r_{e2}(0,t)) \quad (188)$$

where  $C_{dl}$  is the double layer capacitance and  $j$  is the total current density.

Based on the reaction mechanism presented in Table 3-8 and by the introduction of different assumptions three model variants have been formulated. In model 1 ( $M_1$ ) and model 2 ( $M_2$ ), two enzymatic reaction steps are lumped (Eq. (163)). The difference arises from taking into account the mass transport influence of  $S_1$ .  $M_2$  accounts of the mass transfer effects of

substrates and protons while these are neglected in  $M_1$ . Additionally,  $M_2$  considered the two electrochemical steps while they are lumped in  $M_1$  (Eq. (166)). Model 3 ( $M_3$ ) is the most complicated, considering the formation and decomposition of the  $E_1S_1$  complex and all mass transfer effects. At steady state conditions, the analytical solution of the overall electrochemical rate expression using the BV approach can be derived for the three models in Table 3-10. For the detailed derivation, please refer to Appendix 2.

**Table 3-10: Final expression of the electrochemical steady state reaction rate of the three mechanistic models using the BV approach**

Model	Final expression of steady state reaction rate
$M_1$	$r_{e,ss}(0, t) = - \frac{2k_1\Gamma_t C_{H^+,ss}(0, \eta_{ss}) C_{S1,ss}(0, \eta_{ss}) k_e e^{\left(-\frac{\alpha F}{RT} \eta_{ss}\right)}}{k_1 C_{S1,ss}(0, \eta_{ss}) + k_e e^{\left(-\frac{\alpha F}{RT} \eta_{ss}\right)} C_{H^+,ss}(0, \eta_{ss})} \quad (189)$
$M_2$	$r_{e,ss}(0, t) = - \frac{2k_1\Gamma_t C_{H^+,ss}(0, \eta_{ss}) C_{S1,ss}(0, \eta_{ss}) k_e e^{\left(-\frac{\alpha F}{RT} \eta_{ss}\right)}}{k_1 C_{S1,ss}(0, \eta_{ss}) + k_e e^{\left(-\frac{\alpha F}{RT} \eta_{ss}\right)} C_{H^+,ss}(0, \eta_{ss})} \quad (190)$
$M_3$	$r_{e,ss}(0, t) = - \frac{2k_{cat}\Gamma_t C_{H^+,ss}(0, \eta_{ss}) C_{S1,ss}(0, \eta_{ss}) k_e e^{\left(-\frac{\alpha F}{RT} \eta_{ss}\right)}}{k_{cat} C_{S1,ss}(0, \eta_{ss}) + k_e e^{\left(-\frac{\alpha F}{RT} \eta_{ss}\right)} C_{S1,ss}(0, \eta_{ss}) C_{H^+,ss}(0, \eta_{ss}) + K_m k_e e^{\left(-\frac{\alpha F}{RT} \eta_{ss}\right)} C_{H^+,ss}(0, \eta_{ss})} \quad (191)$

In Eqs. (189-191),  $k_e$  stands for an effective electrochemical rate constant defined as:

$$k_e = \frac{k_{e1}k_{e2}}{k_{e1}+k_{e2}} \quad (192)$$

while  $K_m$  is the Michaelis menten kinetic constant

$$K_m = \frac{k_{cat}+k_{-1}}{k_1} \quad (193)$$

### 3.4.1.2 Electrochemical impedance spectroscopy derivation

The aim of this section is to present the application of the dynamic method FRA to extract the EIS for identifying adequate reaction kinetics of HRP on a conductive surface in the presence of  $H_2O_2$ . In this present case the potential has been chosen as an input variable. Applying the variable definition from section (2.5) and the Taylor approximation of nonlinear terms (specifically to the rate reaction expression [100], the below equations are obtained:

$$\Delta r_e(0, t) = \Delta r_{1e}(0, t) + \Delta r_{2e}(0, t) \quad (194)$$

$$\Delta r_e(0, t) = \underbrace{\left. \frac{\partial r_{1e}(0, t)}{\partial \Gamma_{CPI}} \right]_{SS}}_{P_1} \Delta \Gamma_{CPI}(0, t) + \underbrace{\left. \frac{\partial r_{1e}(0, t)}{\partial C_{H^+}} \right]_{SS}}_{P_2} \Delta C_{H^+}(0, t) + \underbrace{\left. \frac{\partial r_{1e}(0, t)}{\partial E} \right]_{SS}}_{P_3} \Delta E(0, t) + \underbrace{\left. \frac{\partial r_{2e}(0, t)}{\partial \Gamma_{CPII}} \right]_{SS}}_{P_4} \Delta \Gamma_{CPII}(0, t) + \dots \quad (195)$$

A similar procedure is applied to formulate the enzymatic reaction rates. The expressions for the Taylor coefficients,  $P_1$ ,  $P_2$ , and  $P_3$  are given in Appendix 3. As previously mentioned, the focus of the present work is the Faradaic impedance of bio-electrochemical events. Therefore, the 1<sup>st</sup> order of FRA containing linear information which is identical to EIS was derived. Similar to steady state conditions, three model variants, shown in Table 3-10, have been formulated. These models result in three different mathematical expressions of the theoretical EIS. The final expression for the electrochemical admittance  $H_1(\omega)$  of the  $M_3$  reads.

$$H_1(\omega) = \frac{2FR_4R_1 - R_3C_{dl}j\omega}{2F(R_4R_2 - R_3R_5)} \quad (196)$$

where the groups  $R_i$  ( $i=1, 5$ ) and further coefficients contained in groups  $R_i$  are defined in Appendix 3.

### 3.4.2 Porous electrode with HRP

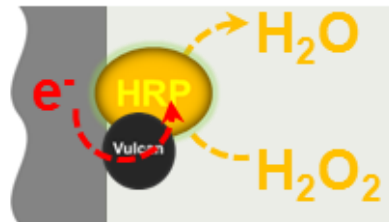


Figure 3-5: Schematic representation of the reaction kinetics of HRP in a conductive porous electrode in the presence of  $H_2O_2$

HRP is then introduced into a porous conductive matrix using Vulcan nanoparticles. The reaction kinetics of the Horseradish Peroxidase (HRP) in the presence of  $H_2O_2$  on a conductive surface for the cathode side has been discussed in section 3.4.1. The distributed model is now applied using the same reaction kinetics of  $M_3$  with a minor modification. Unlike in the original model, the proton diffusion effect was neglected. The justification for inserting  $M_3$  into the

porous electrode can be seen in section 5.3.1. Experimentally, this assumption is well satisfied in the systems which are supplied with a well-buffered solution.

The key model equations in the CL include charge balances at the interface, ion- and electron- conducting phases (presented in section 2.2 and 3.4.1), the mass balances of the related species in the CL and DL are presented in Table 3-11.

**Table 3-11: Mass balances of all related species in the CL and DL of a/the porous electrode. System: porous DET electrode using HRP as a model enzyme**

Mass balance	Mathematical equation	BC2
Substrate $S_1$	<p>In CL</p> $\varepsilon \frac{\partial C_{S_1}^{CL}(z,t)}{\partial t} = \frac{\partial}{\partial z} \left( D_{S_1}^{CL} \frac{\partial C_{S_1}^{CL}(z,t)}{\partial z} \right) - ar_1(z,t) \quad (197)$ <p>In DL</p> $\frac{\partial C_{S_1}^{DL}(z,t)}{\partial t} = \frac{\partial}{\partial z} \left( D_{S_1}^{DL} \frac{\partial C_{S_1}^{DL}(z,t)}{\partial z} \right) \quad (198)$	<ul style="list-style-type: none"> <li>• <math>D_{S_1}^{CL} \frac{\partial C_{S_1}^{CL}(z,t)}{\partial z} \Big _{z=0} = 0 \quad (199)</math></li> <li>• <math>C_{S_1}^{DL}(z = L + \delta_{S_1}, t) = C_{S_1}^{bulk}(t) \quad (200)</math></li> <li>• <math>-D_{S_1}^{CL} \frac{\partial C_{S_1}^{CL}(z,t)}{\partial z} \Big _{z=L^-} = -D_{S_1}^{DL} \frac{\partial C_{S_1}^{DL}(z,t)}{\partial z} \Big _{z=L^+} \quad (201)</math></li> <li>• <math>C_{S_1}^{CL}(L^-, t) = C_{S_1}^{DL}(L^+, t) \quad (202)</math></li> </ul>
Enzyme substrate $E_1S_1$	$\frac{\partial \Gamma_{E_1S_1}(z,t)}{\partial t} = r_1(z,t) - r_{cat}(z,t) \quad (203)$	
Compound I	$\frac{\partial \Gamma_{CPI}(z,t)}{\partial t} = r_{cat}(z,t) -  r_{e1}(z,t)  \quad (204)$	
Compound II	$\frac{\partial \Gamma_{CPII}(z,t)}{\partial t} =  r_{1e}(z,t)  -  r_{2e}(z,t)  \quad (205)$	
Enzyme conservation	$\Gamma_{E_1t}(z,t) = \Gamma_{E_1S_1}(z,t) + \Gamma_{CPI}(z,t) + \Gamma_{CPII}(z,t) \quad (206)$	

The reaction rates appearing in Table 3-11 is presented in Table 3-8 and Table 3-10.

### 3.4.3 Porous electrode with an enzymatic cascade

As can be seen from section 3.4.2, the presence of  $O_2$  in the GOx electrode can cause instability and a decline in the system performance. This is because of the formation of the intermediate  $H_2O_2$ . To overcome these problems, HRP are usually introduced to consume  $H_2O_2$  locally [49, 131]. The reaction mechanism of GOx-HRP in the presence of glucose and  $O_2$  on a conductive surface is presented schematically in Figure 3-6. The reaction rate expressions are given in detail in Eqs. (199-206). The reaction steps of the enzyme cascade in a porous electrode start with the glucose oxidation step. This step is catalysed by GOx giving the intermediate  $H_2O_2$  ( $S_1$ ),

which is then further removed locally by HRP. The pure enzymatic reaction steps and related reaction rates of GOx with glucose were presented in section 3.3.2 and the effect of  $O_2$  on the catalytic cycle of GOx was presented in 3.3.3. The electrochemical regeneration of HRP in the presence of  $H_2O_2$  was presented in section 3.4.1 and section 3.4.2. All the assumptions of the porous electrode presented in sections 3.3, 3.4.1 and 3.4.2 are valid for the porous enzymatic electrode using GOx-HRP as an enzymatic cascade.

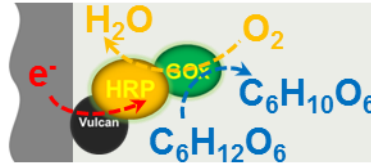


**Figure 3-6: Schematic representation of the reaction mechanism for the enzymatic cascade using GOx and HRP in the presence of glucose and  $O_2$  in a porous conductive matrix**



The mass balances of all related species are presented in Table 3-12

Table 3-12: Mass balance of all related species in the enzymatic cascade

Mass Balance	Mathematical equation	BCs
Substrate $S_2$	In CL $\varepsilon \frac{\partial C_{S_2}^{CL}(z,t)}{\partial t} = \frac{\partial}{\partial z} \left( D_{S_2}^{CL} \frac{\partial C_{S_2}^{CL}(z,t)}{\partial z} \right) - r_{11}(z,t)$ (214)	<ul style="list-style-type: none"> <li>• <math>D_{S_2}^{CL} \frac{\partial C_{S_2}^{CL}(z,t)}{\partial z} \Big _{z=0} = 0</math> (216)</li> <li>• <math>C_{S_2}^{DL}(z = L + \delta_{S_2}, t) = C_{S_2}^{bulk}(t)</math> (217)</li> </ul>
	In DL $\frac{\partial C_{S_2}^{DL}(z,t)}{\partial t} = \frac{\partial}{\partial z} \left( D_{S_2}^{DL} \frac{\partial C_{S_2}^{DL}(z,t)}{\partial z} \right)$ (215)	<ul style="list-style-type: none"> <li>• <math>-D_{S_2}^{CL} \frac{\partial C_{S_2}^{CL}(z,t)}{\partial z} \Big _{z=L^-} =</math></li> <li><math>-D_{S_2}^{DL} \frac{\partial C_{S_2}^{DL}(z,t)}{\partial z} \Big _{z=L^+}</math> (218)</li> <li>• <math>C_{S_2}^{CL}(L^-, t) = C_{S_2}^{DL}(L^+, t)</math> (219)</li> </ul>
$O_2$	In CL $\varepsilon \frac{\partial C_{O_2}^{CL}(z,t)}{\partial t} = \frac{\partial}{\partial z} \left( D_{O_2}^{CL} \frac{\partial C_{O_2}^{CL}(z,t)}{\partial z} \right) - r_{33}(z,t)$ (220)	<ul style="list-style-type: none"> <li>• <math>D_{O_2}^{CL} \frac{\partial C_{O_2}^{CL}(z,t)}{\partial z} \Big _{z=0} = 0</math> (222)</li> <li>• <math>C_{O_2}^{DL}(z = L + \delta_{O_2}, t) = C_{O_2}^{bulk}</math> (223)</li> </ul>
	In DL $\frac{\partial C_{O_2}^{DL}(z,t)}{\partial t} = \frac{\partial}{\partial z} \left( D_{O_2}^{DL} \frac{\partial C_{O_2}^{DL}(z,t)}{\partial z} \right)$ (221)	<ul style="list-style-type: none"> <li>• <math>-D_{O_2}^{CL} \frac{\partial C_{O_2}^{CL}(z,t)}{\partial z} \Big _{z=L^-} =</math></li> <li><math>-D_{O_2}^{DL} \frac{\partial C_{O_2}^{DL}(z,t)}{\partial z} \Big _{z=L^+}</math> (224)</li> <li>• <math>C_{O_2}^{CL}(L^-, t) = C_{O_2}^{DL}(L^+, t)</math> (225)</li> </ul>
Substrate $S_1$	In CL $\varepsilon \frac{\partial C_{S_1}^{CL}(z,t)}{\partial t} = \frac{\partial}{\partial z} \left( D_{S_1}^{CL} \frac{\partial C_{S_1}^{CL}(z,t)}{\partial z} \right) +$ $r_{33}(z,t) - a(r_1(z,t) - r_{-1}(z,t))$ (226)	<ul style="list-style-type: none"> <li>• <math>D_{S_1}^{CL} \frac{\partial C_{S_1}^{CL}(z,t)}{\partial z} \Big _{z=0} = 0</math> (228)</li> <li>• <math>C_{S_1}^{DL}(z = L + \delta_{S_1}, t) = 0</math> (229)</li> </ul>
	In DL $\frac{\partial C_{S_1}^{DL}(z,t)}{\partial t} = \frac{\partial}{\partial z} \left( D_{S_1}^{DL} \frac{\partial C_{S_1}^{DL}(z,t)}{\partial z} \right)$ (227)	<ul style="list-style-type: none"> <li>• <math>-D_{S_1}^{CL} \frac{\partial C_{S_1}^{CL}(z,t)}{\partial z} \Big _{z=L^-} =</math></li> <li><math>-D_{S_1}^{DL} \frac{\partial C_{S_1}^{DL}(z,t)}{\partial z} \Big _{z=L^+}</math> (230)</li> <li>• <math>C_{S_1}^{CL}(L^-, t) = C_{S_1}^{DL}(L^+, t)</math> (231)</li> </ul>
Enzyme substrate $E_1S_1$	$\frac{\partial \Gamma_{E_1S_1}(z,t)}{\partial t} = r_1(z,t) - r_{-1}(z,t) - r_{cat}(z,t)$ (232)	
Compound I	$\frac{\partial \Gamma_{CPI}(z,t)}{\partial t} = r_{cat}(z,t) -  r_{e1}(z,t) $ (233)	
Compound II	$\frac{\partial \Gamma_{CPII}(z,t)}{\partial t} =  r_{e1}(z,t)  -  r_{e2}(z,t) $ (234)	
Conservation of mediator and enzyme concentration	$C_{E1t}(z,t) = C_{E1red}(z,t) + C_{CPI}(z,t) + C_{E1S1}(z,t) + C_{CPII}(z,t)$ (235)	
	$C_{E2t}(z,t) = C_{E2red}(z,t) + C_{E2ox}(z,t)$ (236)	

To investigate the influence of  $O_2$  supplied from different sides of the CL-DL, different  $O_2$  supply scenarios (Sc) were arranged (Figure 3-7).  $O_2$  is supplied from the bulk from Sc1 which reflects the experimental condition of  $O_2$  supplied from the bulk. The difference between Sc2 and Sc1 is the direction of the  $O_2$  supply. Instead of bubbling  $O_2$  into the bulk it is supplied from the other side of CL ( $z=0$ ). The  $O_2$  supply of the Sc3 is the combination of Sc1 and Sc2. The variance in the  $O_2$  supply direction is reflected mathematically in the boundary conditions which are presented in Table 3-13.

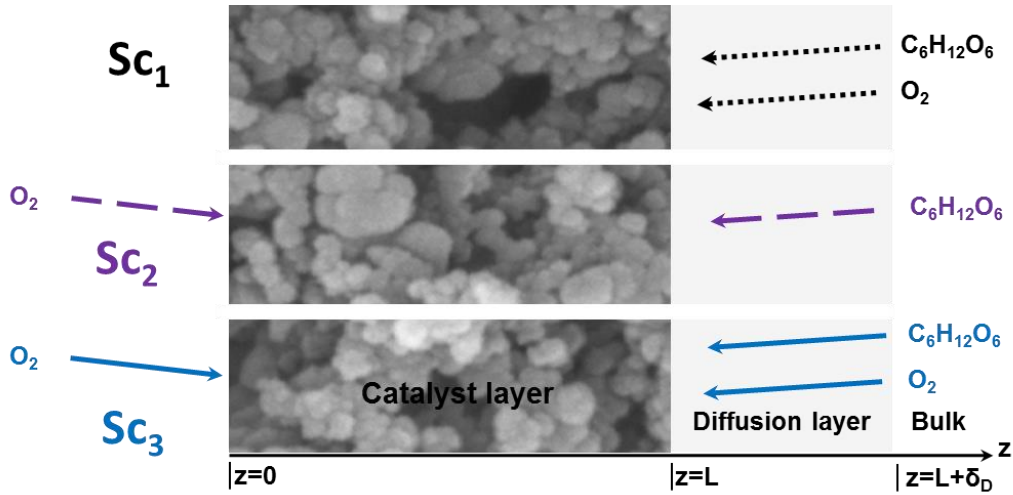


Figure 3-7: Schematic representation of  $O_2$  supply into a porous CL

Table 3-13: BCs and ICs of the enzymatic cascade with different  $O_2$  supply scenarios

Scenario 2	Scenario 3
$\bullet D_{O_2}^{CL} \frac{\partial C_{O_2}^{CL}(z,t)}{\partial z} \Big _{z=L+\delta_{O_2}} = 0 \quad (237)$	$\bullet C_{O_2}^{DL}(z=0, t) = C_{O_2}^{bulk} \quad (241)$
$\bullet C_{O_2}^{DL}(z=0, t) = C_{O_2}^{bulk} \quad (238)$	$\bullet C_{O_2}^{DL}(z=L+\delta_{O_2}, t) = C_{O_2}^{bulk} \quad (242)$
$\bullet -D_{O_2}^{CL} \frac{\partial C_{O_2}^{CL}(z,t)}{\partial z} \Big _{z=L^-} =$	$\bullet -D_{O_2}^{CL} \frac{\partial C_{O_2}^{CL}(z,t)}{\partial z} \Big _{z=L^-} =$
$-D_{O_2}^{DL} \frac{\partial C_{O_2}^{DL}(z,t)}{\partial z} \Big _{z=L^+} \quad (239)$	$-D_{O_2}^{DL} \frac{\partial C_{O_2}^{DL}(z,t)}{\partial z} \Big _{z=L^+} \quad (243)$
$\bullet C_{O_2}^{CL}(L^-, t) = C_{O_2}^{DL}(L^+, t) \quad (240)$	$\bullet C_{O_2}^{CL}(L^-, t) = C_{O_2}^{DL}(L^+, t) \quad (244)$



## 4 Experimental validation

In this section, details of the experimental validation procedures relevant for this thesis, are given. This information has been published partly in [20, 114, 116-117]. The following sections simply provide the experimental details for reference/calculation convenience.

### 4.1 Materials

Glucose oxidase (EC 1.1.3.4, GOx) from *Aspergillus niger* was supplied by Fluka. Horseradish peroxidase (E.C. 1.11.1.7, HRP) from *America rusticana* was supplied by Serva Electrophoresis GmbH. All enzymes were used without further characterization or purification. Vulcan XC72R was provided by Cabot EMEA. Tetrathiafulvalene (TTF), disodium hydrogen phosphate ( $\text{Na}_2\text{HPO}_4$ ) and 1-methyl-2-pyrrolidone, glutaraldehyde (GA/ 50% w/v) were supplied by Sigma Aldrich. Gelatin, potassium dihydrogen phosphate ( $\text{KH}_2\text{PO}_4$ ), hydrogen peroxide ( $\text{H}_2\text{O}_2$ , 30% w/v) and poly(vinylidene fluoride) (PVDF) were supplied by Merck. Spectroscopic graphite disks (10 mm) were supplied from Ted Pella INC. All chemicals were of analytical reagent grade and all solutions were prepared using ultrapure water from Millipore.

### 4.2 Electrode preparation

#### 4.2.1 Enzymatic anode

The porous structural electrodes incorporating all the materials were prepared using two procedures, PVDF and Gelatin. The first difference between the two procedures is the utilization of different binders: PVDF and Gelatin respectively (Figure 4-1). The second difference is the way in which enzymes were incorporated inside the porous conductive matrix. In the PVDF procedure, enzymes were physically absorbed on a prepared conductive matrix while they were mixed with other materials from the beginning to form an ink, which was later cast on the electrical supporter in the Gelatin procedure. The detail is given in Figure 4-1.

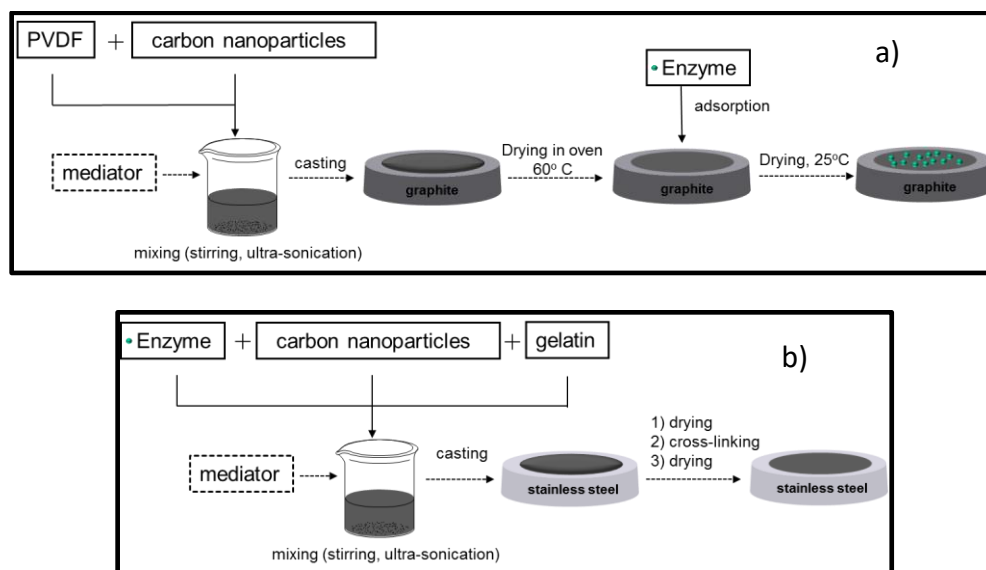


**Figure 4-1: Schematic representation of electrode preparation procedure a) PVDF and b) Gelatin**

In the PVDF procedure preparation, 20 mg of Vulcan and 10 mg of TTF were suspended /dissolved in 1 ml of 0.25 wt% PVDF solution prepared using 1-methyl-2-pyrrolidone. 70  $\mu\text{l}$  of the prepared ink was cast on spectroscopic graphite disks (Ted Pella INC, 10 mm) and left to dry at 60  $^{\circ}\text{C}$  for 5 hours. After drying, Vulcan-TTF-PVDF electrodes were modified by physical adsorption of 50  $\mu\text{l}$  of solution containing GOx in different concentrations (from 0.1  $\text{mg ml}^{-1}$  to 14  $\text{mg ml}^{-1}$ ) prepared in a 0.1 M phosphate buffer, pH7. The adsorption of enzymes on the Vulcan-TTF-PVDF electrodes was performed for 2 hours at room temperature.

In the Gelatin preparation procedure, the ink components were prepared by 20 mg of Vulcan, 10 mg of TTF, and 0.5 mg of GOx. In the case of enzyme/mediator loading testing, GOx and mediator varied from 0.5 mg to 14 mg and from 0.1 mg to 20 mg, respectively while the other loadings were kept constant. To prepare the catalyst ink, GOx, TTF and Vulcan were mixed in 1 ml of 1.96 wt% Gelatin solution at 37  $^{\circ}\text{C}$ . The ink was then cast on stainless steel disks degreased with acetone before usage. The aliquots of catalyst ink applied on the disks varied from 20  $\mu\text{l}$  for lower material loading to 50  $\mu\text{l}$  for higher material loading. The electrodes were left to dry at ambient temperature and afterwards cross linked by being dipped into the 5% (GA) for 1 minute. The electrodes were then again dried at room temperature and stored at  $-20^{\circ}\text{C}$  before usage.

## **4.2.2 Enzymatic cathode**

### **4.2.2.1 Thin film electrode preparation**

Spectroscopically pure carbon (graphite) planchets (Ted Pella, INC, USA) with impurities equal to or less than 2 ppm were used as mechanical and electrical supports for the electrode preparation. These graphite electrodes were polished by fine emery paper (P1000), rinsed with deionized water and then further polished with ordinary white paper to smooth the rough electrode surface.

For the preparation of the HRP modified electrodes, 50  $\mu\text{l}$  of 6  $\text{mg ml}^{-1}$  HRP solution in a phosphate buffer was placed on top of the graphite electrode and left to dry in ambient conditions. The electrodes were then fitted into a rotating disk holder, rinsed with phosphate buffer solution and placed in a cell for 2 hours under rotation in order to desorb all the weakly adsorbed enzymes.

To justify the assumption of using thin film electrode parameters in a porous electrode system, an ultra-thin-film electrode was prepared using a small amount of Vulcan loading from the same ink as a porous electrode. A small amount of this ink was then cast onto a conductive supporter, forming a so-called ultra-thin film electrode. Subsequently, a similar step to the preparation of HRP modified electrodes for enzyme adsorption was applied.

### **4.2.2.2 Porous electrode with single enzyme**

In the same way as the anode, two procedures were used for the porous electrode preparation on the cathode side. In the PVDF procedure, 20 mg of Vulcan was dissolved in 1 ml of 0.25 wt% PVDF solution prepared using 1-methyl-2-pyrrolidone. Different amounts (25  $\mu\text{l}$ , 70  $\mu\text{l}$ ) of the prepared ink were cast onto graphite disks and these electrodes were then left to dry at 60  $^{\circ}\text{C}$ . In the case of the ultra-thin film electrodes, the ink loading Vulcan at 0.056  $\text{mg cm}^{-2}$  was prepared by diluting the original ink further. After drying, these electrodes were modified by applying 50  $\mu\text{l}$  of 6  $\text{mg ml}^{-1}$  of HRP solution prepared in 0.1 M phosphate buffer. The enzyme adsorption step was performed for 2 hours at room temperature. The electrodes were then left to dry at room temperature and were ready for use.

In the Gelatin procedure, the catalyst ink was prepared by dissolving 20 mg of Vulcan powder and 10 mg HRP in 1 ml of 1.96 wt% Gelatin solution (at 35°C). The ink was then cast onto stainless steel disks degreased with acetone before usage. The aliquots of catalyst ink applied to the disks varied from 20  $\mu\text{l}$  to 50  $\mu\text{l}$ , resulting in Vulcan loadings of 1.43 and 3.6 mg  $\text{cm}^{-2}$  respectively. The electrodes were left to dry at ambient temperature and cross linked by dipping into the 5% glutaraldehyde (GA) for 1 minute. The electrodes were then dried again at room temperature and stored at -20°C before usage.

#### **4.2.2.3 Porous electrode with enzymatic cascade**

The PVDF procedure was adapted to the present case. Briefly, 20 mg of Vulcan was dissolved in 1 ml of 0.25 wt% PVDF solution prepared using 1-methyl-2-pyrrolidone. 70  $\mu\text{l}$  of the prepared ink was applied to the graphite disks and these electrodes were then left to dry at 60 °C. After drying, they were modified by applying 50  $\mu\text{l}$  of HRP-GOx solution prepared in a 0.1 M phosphate buffer. The concentrations of HRP and GOx were 6 mg  $\text{ml}^{-1}$  and 6 mg  $\text{ml}^{-1}$  for the loading ratio 1:1. At other loading ratios, i.e 1:1, 1:2, 1:3, 2:1, and 3:1, enzyme concentration changes with respect each enzyme. The adsorption step was performed for 2 hours at room temperature. The electrode were then left to dry at room temperature before being ready for use.

### **4.3 Measurements**

All the prepared enzymatic electrodes were mounted into a rotating disk electrode holder (RDE, Radiometer Analytical) with an opening of 6 mm and were used as working electrodes in three electrode electrochemical cells. Pt wire and the saturated calomel electrode (SCE) were used as a counter electrode and a reference electrode, respectively. The experiments were conducted at a constant rotation rate of 400 rpm (rounds per minute) in order to ensure defined mass transport conditions. All the electrochemical experiments were repeated at least three times using an Autolab potentiostat (PGSTAT302, EcoChemie).

In all the measurements, the electrolyte was a 0.1 M phosphate buffer solution, containing potassium dihydrogen phosphate (Merck) and disodium hydrogen phosphate (Sigma-Aldrich). The buffer was prepared at different pH values, i.e pH5, pH6 and pH7.

#### **4.3.1 Enzymatic anode**

The experiments were first conducted in a nitrogen atmosphere at a constant rotation rate of 400 rpm (rounds per minute). The measurements were then exposed to the O<sub>2</sub> supply in ambient conditions. All the measurements were performed at pH6, 25°C and pH7, 37°C. Steady state polarization curves were obtained from current time dependences at constant potentials by extracting the values after 120 seconds.

#### **4.3.2 Cathode**

##### **4.3.2.1 Thin film electrode**

All the experiments were carried out at 25°C, pH5 and pH6. Beforehand, the solution was purged with nitrogen and a nitrogen atmosphere was maintained during all the experiments. The steady state experiments were performed with a fixed delay of 45 second at every potential. Impedance measurements were taken in a frequency range from 10 Hz to 50 kHz at different steady state potentials. The amplitude of the sinusoidal signal was 10 mV (from base to peak).

##### **4.3.2.2 Porous electrode**

Steady state polarization curves were obtained from current time dependences at constant potentials by extracting the values after 1 minute. All the experiments were conducted at pH5 and pH6, in nitrogen atmosphere at a constant rotation rate of 400 rpm. At least three replicates were made for each measurement.

#### **4.3.3 Scanning electron microscopy**

The morphology of the enzymatic electrode surfaces and electrode cross-sections were investigated by scanning electron microscopy (SEM) at AQura GmbH, Germany.

## 5 Results and discussion

In this section, the model parameters which appeared in mathematical equations are discussed in brief and the results of each case are given in a sequence, as presented in section 3.

### 5.1 Model parameters

In the porous model, several groups of parameters appear in the mathematical model; i.e kinetic, operating, transport, structural and thermodynamic parameters. The operating, transport, and thermodynamic parameters were mainly extracted from experimental conditions/measurements or from the literature on the relevant systems. The structural parameters in the porous electrode; i.e: the porosity, electrode thickness and electrochemical active surface area, are taken either from experimental conditions or estimation. In the interface model, the structural parameters are disregarded; apart from the electrochemical active surface area. The fitted parameters were obtained from the optimization with the experimental data using the least square objective function (see Eq. (88)).

In the EES, one of the critical parameters, which has a huge influence on the kinetic constants, is the amount of enzymes remaining active for catalytic reactions. As can be anticipated in reaction rate equations, i.e (Eq. (189-191)), the kinetic constants are inversely correlated to the enzyme coverage/concentration. Therefore, the assumption of higher enzyme coverage can lead to significantly lower values of kinetic parameters and vice versa. At the moment, there is no practically applicable method to exactly determine this value. In this work, it is considered as a fitting parameter. The initial value corresponds to the value in the literature source of the similar system.

One of the important structural parameters that should be mentioned here in advance is internal active surface area. The literature on non-enzymatic systems normally considers this value based on the total catalyst loading, the thickness of CL and the catalyst specific surface area (i.e BET area) [133-134]. In the case of the interface model, assuming the monolayer of enzyme adsorption and neglecting the roughness factor, this value is identical with to the

geometrical surface area of the electrode. In addition, this value is closely related to the total number of immobilized enzymes in the case of DET and the electrochemical contact of mediators with electronically conductive support in the case of MET. The correlation of these factors to the active surface area is not straight-forwardly expressed. Therefore, ' $\alpha$ ' can be either assumed or considered as a fitting parameter. The upper/lower limits of ' $\alpha$ ' are the reciprocal of the CL thickness and geometrical area, assuming the effective radius of the Vulcan nanoparticles and the effective CL porosity respectively. The other geometrical parameter is the void fraction ' $\epsilon$ ', which is theoretically restricted between 0 and 1. The void fraction can be also estimated based on the measured thickness of the CL by, for example, scanning electron microscopy (SEM) and the calculated compact thickness of the layer which based on the loadings and densities of all components in the CL as presented in [135]. The estimated value of the porosity has been used as the initial starting values for the parameter optimization in this work.

In the following case studies, a brief introduction to the parameters for each case is given before the discussion details.

## 5.2 Enzymatic anode

This section presents the results of the distributed model applied for the porous enzymatic electrode using enzyme GOx and the mediator TTF. The mathematical modelling details are presented in section 3.3. The mathematical model is first calibrated with experimental data using the PVDF preparation procedure. The kinetic parameters obtained from the PVDF procedure would be used further used to investigate the behaviour of the Gelatin and other relevant systems. This preparation procedure is different to other reported procedures using the TTF mediator. For example, the nominal TTF concentration is higher and PVDF was used as a binder instead of Nafion, as reported in [136], or the electrode was cross-linked by GA. As a consequence, these differences create a significant impact on the electrode performance, as explained in the following discussion.

The overall modelling parameters of the distributed model for the GOx-porous electrode are shown in table 5-1. Among these parameters, the porosity was roughly estimated based on the mathematical formulation provided by Gode [135]. The electrode thicknesses of the studied

electrodes were extracted from SEM images of the cross section of the studied electrode; see figure 5 1. The other parameters were calculated, taken from the literature or were based on experimental conditions. The optimized parameters were obtained by the minimization of the differences between the experimental data and the simulated data, using Eq. (88).

**Table 5-1: Overall simulation parameters for GOx modified Vulcan-TTF-PVDF electrodes**

<b>Kinetic [Table 5-2]</b>	<b>Operating [measured]</b>		<b>Transport [calculated/fitted]</b>	
$K_{11}/\text{m}^3\text{ s}^{-1}\text{mol}^{-1}$	T/ K	298/310	$D_{S_2}^{CL}/10^{-10}\text{m}^2\text{ s}^{-1}$ [137]	9.56
$K_{22}/\text{m}^3\text{ s}^{-1}\text{mol}^{-1}$	$\omega/\text{rad s}^{-1}$	41.87	$D_{\text{Mox}}^{CL}/10^{-10}\text{m}^2\text{ s}^{-1}$	
$k_{e0}/\text{m}_{\text{geo}}^3\text{ m}_{\text{act}}^2\text{ s}^{-1}$	C/ mol m <sup>-3</sup>	0-20	$\kappa_E/\text{S m}_{\text{geo}}^{-1}$	400
$C_{Mt}/\text{mol m}^{-3}$	E vs. SHE/ V	0.044-0.444	$\kappa_I/\text{S m}_{\text{geo}}^{-1}$	0.1
$C_{E2t}/\text{mol m}^{-3}$	$R_{ohm}/\Omega$	61		
	<b>Structural [measured, estimated]</b>		<b>Thermodynamic</b>	
	L/ $\mu\text{m}_{\text{geo}}$	59	$E_r\text{ vs. SHE/ V}$ [114]	0.394
	$\epsilon/\text{m}^3\text{m}_{\text{geo}}^{-3}$	0.35	$\alpha$ [138]	0.5
	$A_{\text{geo}}\times 10^4/\text{m}_{\text{geo}}^2$	0.28		
	$a\times 10^4/\text{m}_{\text{act}}^2\text{ m}_{\text{geo}}^{-3}$	1		

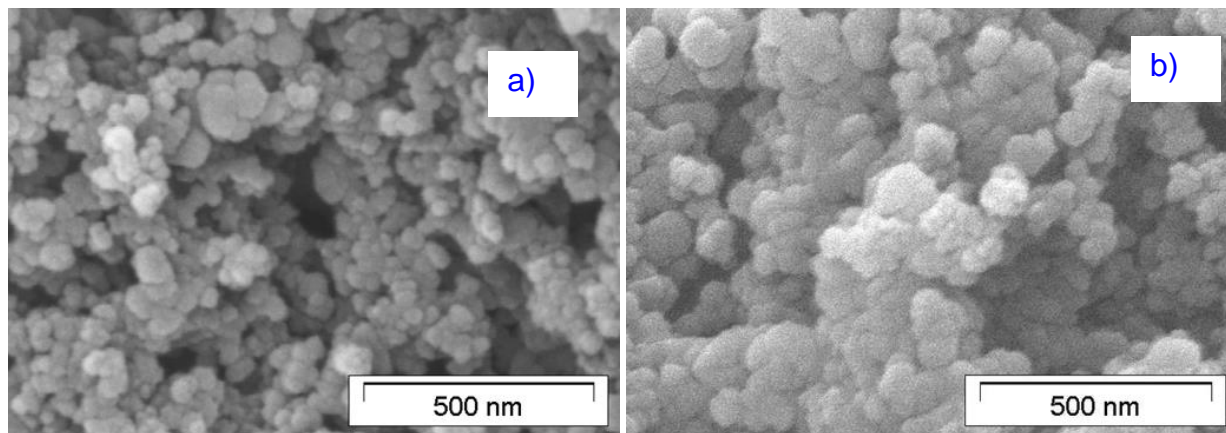


**Figure 5-1: Typical SEM image of a) PVDF porous electrode b) Gelatin porous electrode**

## 5.2.1 Porous electrode with a single substrate

### 5.2.1.1 PVDF porous electrode

#### 5.2.1.1.1 Steady state polarization

The simulation and experimental steady state polarization of GOx modified Vulcan-TTF-PVDF electrodes is presented in Figure 5-2 for the two different operating conditions (pH7, 37°



C and pH6, 25° C). It should be mentioned here that the condition of pH6, 25° C is reported to extract the necessary parameters and these parameters are used later for the description of the porous enzymatic cascade. As the optimized working condition of GOx is at pH7, 37 °C [139] , the model fitting and discrimination were first applied to get the parameters and the best model was selected and applied further for the case at pH6, 25° C.

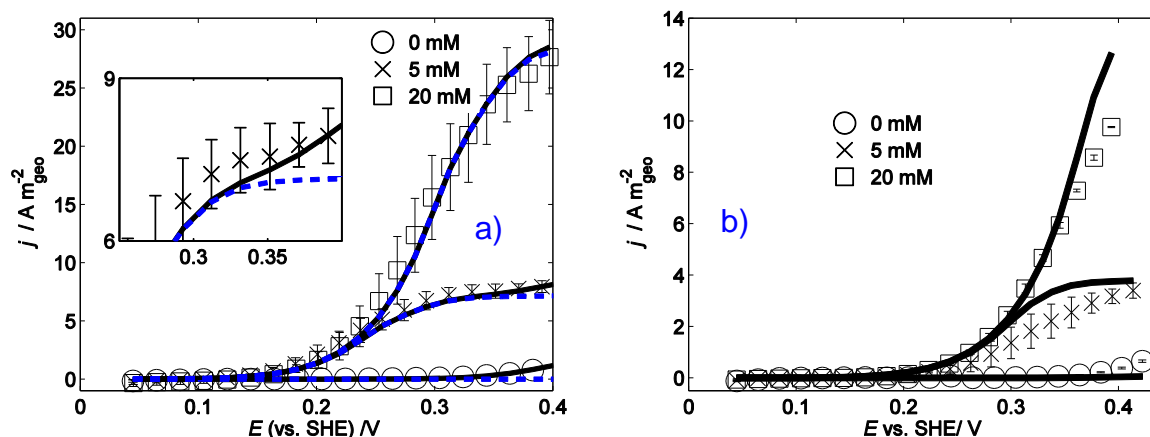


Figure 5-2: Steady state polarization curves of GOx modified Vulcan-TTF-PVDF electrodes: symbols – experimental data, full black lines – simulated curves of the model FM1, dashed blue lines – simulated curves of the model FM2, dashed black lines a) pH7, 37° C b) pH6, 25° C. Conditions: Ratio in mg of Vulcan-TTF-enzyme (20-10-6), fixed delay of 2 minutes, glucose concentrations 0, 5 mM and 20 mM, rotation rate 400 rpm, with other parameters given in table 5-1 and table 5-2

At pH7, 37° C, the electrode current density can reach ca.  $9 \text{ Am}^2_{\text{geo}}$  at 5 mM glucose concentration and ca.  $30 \text{ Am}^2_{\text{geo}}$  at 20 mM glucose concentration, with applied potential at 0.4 V vs. SHE. This performance is comparable or even higher than other reported values in the literature in the same conditions. The referred examples are the Os complex-based electrode incorporating multi-wall carbon nanotubes using GOx at pH7.4, 37° C, 5 mM of glucose and enzyme loading (c.a  $7 \text{ g m}^{-2}_{\text{geo}}$ ) [136], or other reported Os-GOx based electrodes at pH7, 37° C [140-141]. Electrode performance at lower pH and temperature (pH6, 25° C) is smaller than its performance at pH7, 37° C, which is logical since the reaction rate is proportional to an increase in temperature, and the optimized working condition of enzyme GOx is under physiological conditions (pH7, 37° C) [139].

At pH7, 37° C excellent agreement of the simulations using the full model FM1 (black line) and the experimental data can be obtained at different glucose concentrations within the whole range of applied potentials (Figure 5-2a). The optimized parameters are shown in Table 5-2 with  $\chi^2=272$ .  $\chi^2$  is obtained from eq.88 and corresponding the minimal difference of the experimental data and simulation data. The magnitude of the value depends on the scale of the absolute standard deviation of experimental data. An additional step was taken to check the influence of TTF<sup>+</sup> diffusion out of CL by setting the oxidized mediator diffusivity at zero (FM2). The steady state fitting of this model shown in Figure 5-2a in dashed lines demonstrates that the diffusivity of TTF<sup>+</sup> is more pronounced in conditions of higher positive potentials and lower glucose concentration (5 mM). This influence can be ascribed by the higher reaction rate of the electrochemical step due to a higher driving force (higher over-potentials). At the higher glucose concentration, TTF<sup>+</sup> is consumed rapidly by the enzyme regeneration and electrochemical reaction; therefore, the influence is not noticeable. The reduced model has been also used for simulations for this system utilizing the parameters given in Table 5-2. However, it failed to quantify and qualify the experimental data at any set of parameters, which demonstrate the necessity of the full 1-D model in investigating the system behaviour. The full 1-D model is therefore selected for the further studied cases.

Figure 5-2b shows the steady state behaviour of the PVDF system using GOx-TTF in the presence of glucose at pH6, 25° C using the FM1 model. As mentioned in the previous section, this condition is of particular interest due to the involvement with the later enzymatic cascade system using GOx-HRP. The quantitative and qualitative agreement of the simulation and experimental data can be seen in Figure 5-2 with  $\chi^2=304$ . The optimized parameters of the system under two studied conditions are presented in Table 5-2. At 0 mM of glucose supply, the diffusivity of the oxidized mediator was not significantly pronounced as in the case of pH7, 25° C. This probably shows an underestimate value of the oxidized mediator.

**Table 5-2 Optimized simulation parameters for the GOx modified Vulcan-TTF-PVDF electrodes**

Parameter	pH6, 25°C	pH7, 37°C
$K_{11}/ \text{m}^3 \text{ mol}^{-1} \text{ s}^{-1}$	4	9.15
$K_{22}/ \text{m}^3 \text{ mol}^{-1} \text{ s}^{-1}$	1562	6945
$k_{e0}/ 10^{-4} \text{m}_{\text{geo}}^3 \text{m}_{\text{act}}^{-2} \text{s}^{-1}$	3	18
$C_2^{\text{Et}}/ \text{mol m}^{-3}$	0.040	0.048
$C_{\text{Mt}}/ \text{mol m}^{-3}$	1.05**	1.05
$D_{\text{M}}/ 10^{-10} \text{m}_{\text{geo}}^2 \text{s}^{-1}$	0.15	8.61
$\chi^2$	304	272

\*\* adopted values from previous simulation

Analysing the mathematical equations in Table 3-2 and Table 3-4, six individual parameters ( $K_{11}$ ,  $C_{\text{Et}}$ ,  $K_{22}$ ,  $k_{e0}$ ,  $C_{\text{Mt}}$  and  $D_{\text{Mox}}$ ) can be fitted parameters, which should be obtained from the optimization. The fitting parameters of the full model at pH7, 37°C and pH5, 25°C are shown in Table 5-2. At pH7, 37°C, the values of  $K_{11}$  and  $K_{22}$  would be  $9.15 \times 10^3 \text{ M}^{-1} \text{ s}^{-1}$  and  $6.945 \times 10^6 \text{ M}^{-1} \text{ s}^{-1}$  respectively. These values are higher than the values at pH6, 25°C, which reflects the influence of pH and temperature on the constants and the real optimal working conditions of GOx at pH7, 37°C. The value of  $K_{22}$  constant in this condition is in the same magnitude range of the second order rate constants reported for ferrocenemethanol as a mediator ( $0.6\text{-}1.2 \times 10^7 \text{ M}^{-1} \text{ s}^{-1}$  / pH 6, 25 °C) [111-112]. Enzyme utilization at pH7, 37°C is ca 8% higher than its utilization at pH6, 25°C. Moreover, utilization is about 3.5% to 4.8% of the nominal enzyme loading, which reflects the real working conditions of the system; i.e for example enzyme leaching and the presence of inactive enzymes in the nominal loading. Mediator utilization was assumed to be the same for the two studied conditions and the optimized mediator utilization was calculated. This value is relatively small (ca. 0.027% of its nominal concentration), which indicates that the nominal mediator amount can be considerably reduced without any impact on system performance. The electrochemical rate constant  $k_{e0}$  at pH6 25°C and pH7 37°C are  $3 \times 10^{-4} \text{ m}_{\text{geo}}^3 \text{ m}_{\text{act}}^2 \text{ s}^{-1}$  and  $18 \times 10^{-4} \text{ m}_{\text{geo}}^3 \text{ m}_{\text{act}}^2 \text{ s}^{-1}$ , respectively. If the roughness factor is equal to 1, the heterogeneous rate constant is  $3 \times 10^{-4} \text{ m s}^{-1}$   $18 \times 10^{-4} \text{ m s}^{-1}$ , which is in the range of the reported values ( $3 \times 10^{-4}$  to  $2.2 \times 10^{-2} \text{ m s}^{-1}$ ) of the TTF/TTF<sup>+</sup> couple

heterogeneous rate constant at the Pt micro disk electrode in an organic solvent at 293 K [138-142]. The diffusion coefficient of the oxidized mediator ( $D_{MOX}$ ) is  $8.61 \times 10^{-10} \text{ m}^2 \text{ s}^{-1}$ . Bond et al. [138] report the value of  $1.95 \times 10^{-9} \text{ m}^2 \text{ s}^{-1}$  at  $25^\circ\text{C}$  for  $TTF^+$  diffusion in an organic solvent. At pH6,  $25^\circ\text{C}$ , the fitted diffusivity of  $M_{ox}$  is  $1.5 \times 10^{-11} \text{ m}_{geo}^2 \text{ s}^{-1}$  which is smaller than its value at pH7,  $37^\circ\text{C}$ . The smaller diffusivity indicates the dependence of this value on pH and temperature. These optimized parameters are in general smaller than their values at pH7,  $37^\circ\text{C}$ , reflecting the optimal working conditions of GOx at pH7,  $37^\circ\text{C}$  and showing the influence of temperature and pH on system performance [139].

### 5.2.1.1.2 Concentration profiles

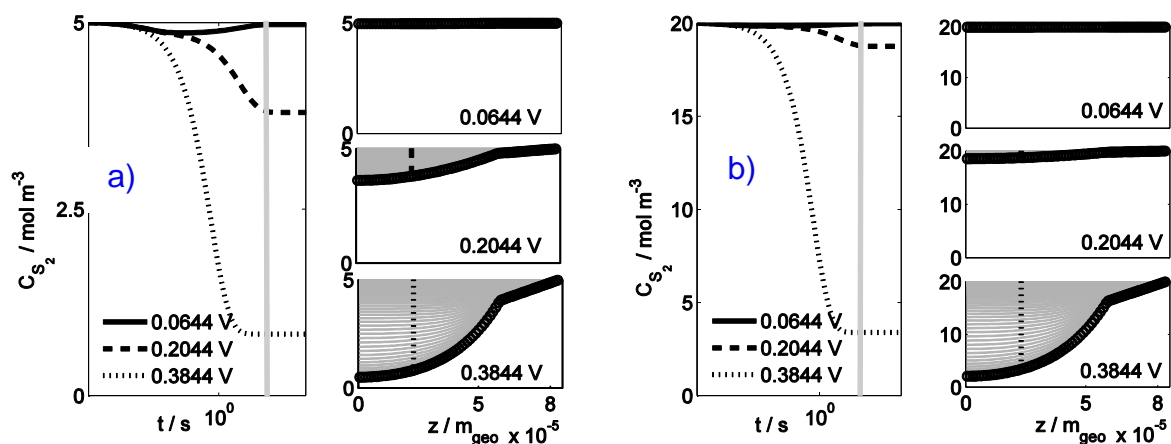


Figure 5-3: Simulated transient (at the middle of CL) and steady state (along spatial coordinate) profiles of glucose concentration a) at 5 mM and b) at 20 mM. Conditions: temperature  $37^\circ\text{C}$ , pH7, rotation rate 400 rpm, with other parameters given in Table 5-1 and Table 5-2

The change in glucose concentration with time at the middle point of the CL and spatial coordinate is presented in Figure 5-3 for conditions of pH7,  $37^\circ\text{C}$ . As can be seen, steady state behaviour can be reached at ca. 120 s for 5 mM and 20 mM of glucose concentration independent on electrode potentials. The spatial profiles show a linear concentration drop in the DL and a further decrease in the CL. The concentration drop in the CL is more pronounced at higher applied potentials due to the fast consumption rate of the species. The different behaviour at different applied potentials can also be explained by different limitation processes at different applied potentials; i.e., the electrochemical process at the lower range and the enzymatic system at higher potentials. These profiles reveal that the CL is working through in

the studied conditions and that the system still works under a mass-reaction control regime. The charge transports (electron and ionic) have no influence on electrode performance.

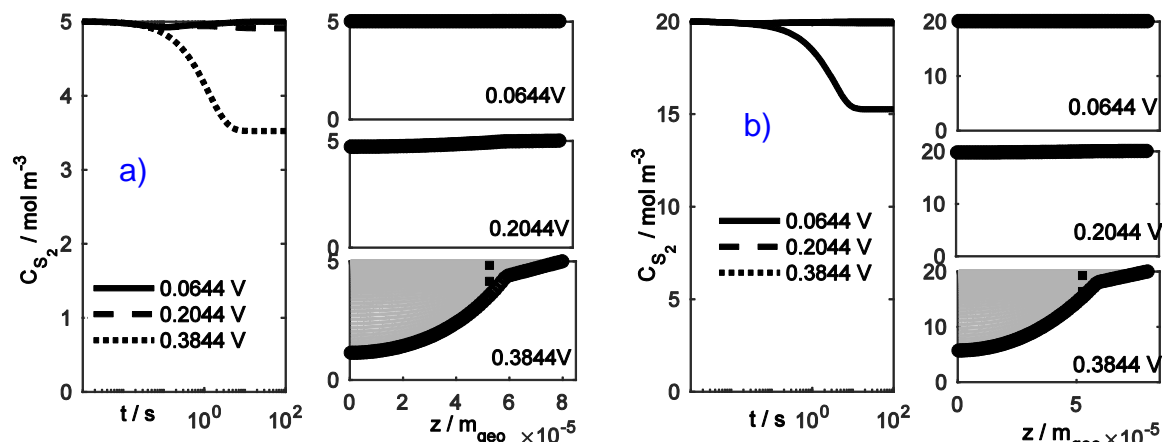


Figure 5-4: Simulated transient (at the middle of CL) and steady state (along spatial coordinate) profiles of glucose concentration a) at 5 mM and b) at 20 mM. Conditions: temperature 25°C pH6, rotation rate 400 rpm, with other parameters given in Table 5-1 and Table 5-2

At pH6, 25°C, similar behaviour of the concentration profile as at values of pH7, 37°C can be also seen in Figure 5-4. Additionally, there is no distribution of glucose concentration in both CL and DL at the lower range of applied potential (<0.2044 V), which can be ascribed to the controlling of the electrochemical step.

### 5.2.1.1.3 Parameter study

A sensitivity analysis of the model's optimized parameters was investigated by varying each parameter in turn, while leaving the other parameters unchanged on the steady state response at pH 7, 37 °C. Beside the optimized values, two limiting cases were also included. The first case corresponds to the small parameter value, which is 10 times smaller than the optimized value. The value of 10 times higher than the optimized value is considered in the latter case.

The influence of these parameters ( $K_{11}$ ,  $K_{22}$ ,  $C_{E2t}$ ,  $C_{Mt}$ ,  $k_{e0}$ ,  $\epsilon$ ,  $D_{MOX}$ ) is shown in Figure 5-5. In general, the higher values of these parameters provide better performance in the system. Some parameters (i.e  $K_{11}$ ,  $D_{Mox}$  and  $\epsilon$ ) have a strong influence on the higher range of applied potentials and some make a significant contribution to system performance in the whole range of applied potentials ( i.e  $C_{E2t}$ ,  $K_{22}$ ,  $C_{Mt}$ ,  $k_{e0}$ ). This can be rationalized by the contribution of

different steps in different potential ranges. For example, the level of active enzymes influences the enzyme substrate and enzymatic mediator step, while the  $K_{11}$  constant only affects the enzyme substrate step and the electrochemical related parameters ( $K_{22}$ ,  $C_{Mt}$ ,  $k_{e0}$ ) directly effect the electrochemical steps. The mass transport related parameters ( $\epsilon$ ,  $D_{MOX}$ ) make a big contribution to the system at higher potential values due to the high substrate demand for enzymatic steps as a consequence of the fast electrochemical reaction rate at higher over-potentials.

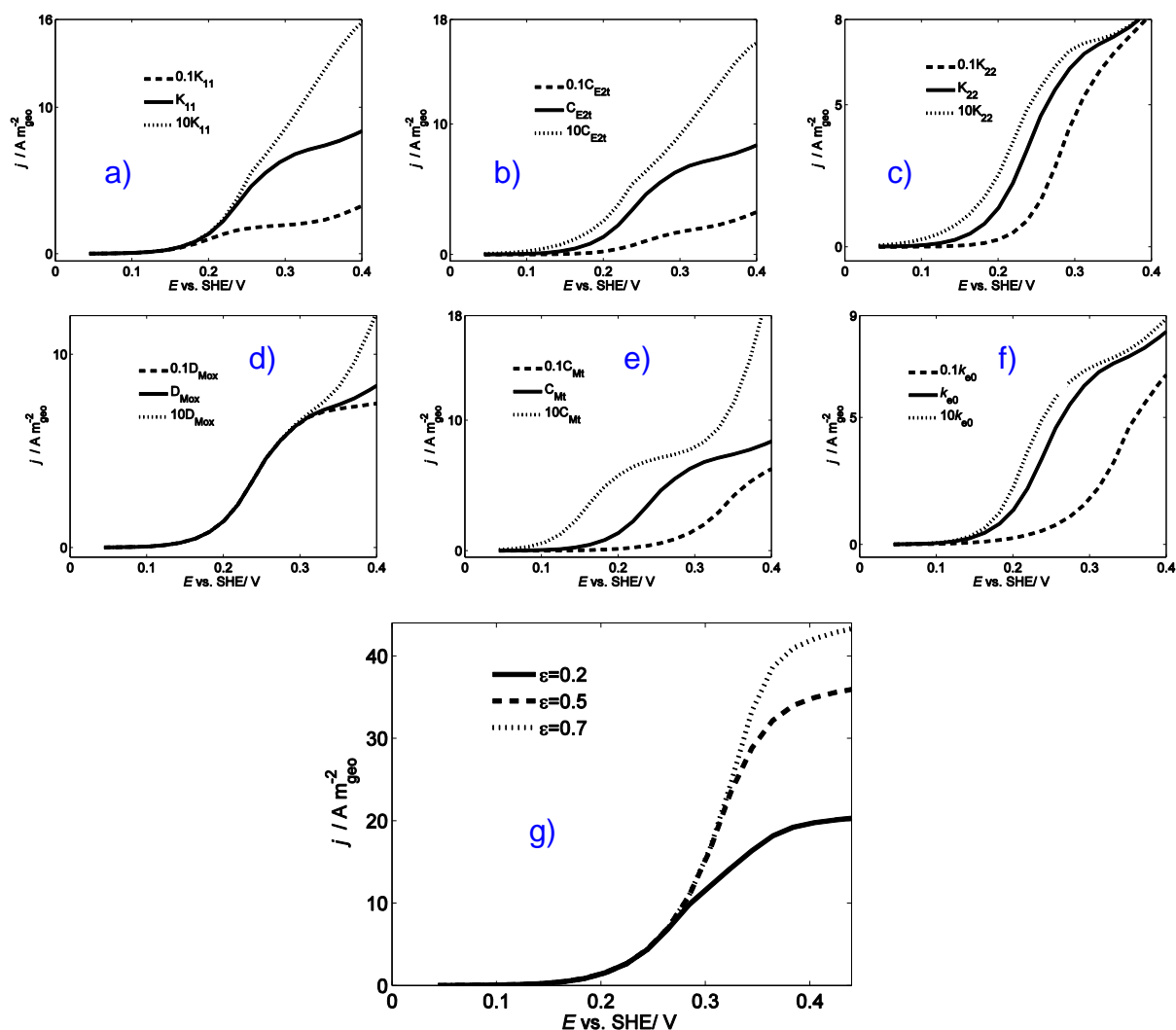


Figure 5-5: Simulated steady state response of the full model showing the influence of the parameter variation with respect to their optimized values a)  $K_{11}$ , b)  $C_{Et}$ , c)  $K_{22}$ , d)  $D_{Mox}$ , e)  $C_{Mt}$ , f)  $k_{e0}$  and g)  $\epsilon$ . Conditions: 5 mM glucose concentration, pH7, temperature 37 °C, rotation rate 400 rpm, with other parameters given in Table 5-1 and Table 5-2

Increasing some parameters, such as  $K_{22}$  and  $k_{e0}$ , did not improve considerably system performance (Figure 5-5 c, f) due to the overall limitations of either enzymatic or electrochemical steps. Changing the mediator concentration in particular create two distinguished influences on electrode performance at the lower and the higher range of potentials. Higher active TTF available in the system at a given enzyme loading and glucose concentration creates a shift in the onset potential of the reaction to lower values. This behaviour can be observed in both simulation and experiment (see section 5.2.1.2 on the Gelatin system). Simultaneously, the effect of TTF<sup>+</sup> diffusion becomes more significant at more positive potentials, as also demonstrated in the model discrimination (Figure 5-2). The porosity creates a dominant change in the higher potential range due to its direct relation to the diffusive species, such as the substrate and the oxidized mediator. The simulation shows that several parameters ( $C_{E2t}$ ,  $K_{22}$  and  $C_{Mt}$ ) might also influence the onset potential of the reaction due to the relation with the amount of mediator TTF. Similar behaviour was also reported in the study of Limoges et al [78].

### **Implications:**

The full 1-D model is necessary to describe the behaviour of the enzymatic electrode using GOx-TTF. Most of the parameters mutually influence the electrode response for the whole applied potential range. Some of them ( $C_{E2t}$ ,  $K_{11}$ ,  $C_{Mt}$ ,  $D_{Mox}$ ,  $\epsilon$ ) had a strong influence at the higher range of applied potentials; i.e., the oxidized mediator diffusivity and the enzymatic constant  $K_{11}$ . The concentration profiles illustrated that electrodes work through under all studied conditions. The shift of the onset potential can be ascribed to the changing of the three parameters ( $C_{E2t}$ ,  $K_{22}$ ,  $C_{Mt}$ ). Electrode performance is higher at pH7, 37°C than its value at pH7, 25°C.

#### **5.2.1.2 Gelatin porous electrode**

The PVDF was demonstrated to be an efficient system providing high current density for the MET case using GOx as the model enzyme in the presence of mediator TTF and substrate glucose. However, due to their physical adsorption, leaching of enzymes can happen after several operating hours. The Gelatin procedure that uses gelatine to encapsulate all the materials in a stable insoluble conductive matrix can overcome these problems. However, a different material arrangement inside the porous structure is expected for the different

electrode preparation procedures. The differences can influence electrode performance, which is proved in the following sections. These influences were mostly correlated in the modelling by geometrical/optimized parameters. To analyse this system, a similar modelling approach incorporating the following assumptions is used:

- The immobilization technique of the porous matrix effectively influences on two groups of parameters, as found in previous section. The first refers to the total number of enzymes/mediators and the second one is the structural parameter i.e. porosity/thickness/active surface area. This assumption can later allow us to use the kinetic constant from the PVDF procedure and to directly compare the amount of active enzyme/mediator inside the porous electrode prepared by different procedures in the same operating conditions.
- Unlike the PVDF system, TTF is not dissolved in this system; however, the uniform distribution assumption of the mediator is still applicable, bearing in mind that the mediator can be electrochemically dissolved and can freely move inside the CL.
- The porosities of the thin and thick electrodes for the Gelatin preparation procedure are similar. This assumption is well justified because the same type of ink was used to prepare the electrodes.
- The modelling domain is kept similar to the PVDF system. The differences are the physical interactions inside the catalyst structure, resulting in a change in system performance.

The simulation parameters of the Gelatin electrodes are summarized in Table 5-3. In general, they are similar to the PVDF electrode. Based on the SEM cross sections, the effective electrode thickness of the lower/higher loading electrode of 19  $\mu\text{m}$ / 65  $\mu\text{m}$  respectively has been estimated. The calculated porosity of the thin electrode, according to the equation provided by Gode et al [135], is 0.3, which is in the similar range of porous enzymatic electrodes [0.3-0.45] for both electrodes [132]. Optimization of the parameters starts with the thin electrode. The obtained optimized parameters are then applied to the thick electrode. This strategy is logical, bearing in mind that the same ink was utilized to prepare the two electrodes and only the ink loading varied. Starting the fitting with the thin electrode is also a better



approach, due to the better utilization of the CL and the lower contribution of other resistances (i.e charge, mass) on the thin electrode. The diffusivities of the oxidized mediator and glucose are also fitting parameters due to their relation to the Gelatin environment.

**Table 5-3: Overall modelling parameters for the GOx modified TTF-Gelatin electrodes.**

Kinetic [adopted/fitted]		Operating [measured]		Transport [adopted/fitted]	
$K_{11}/\text{mol}^{-1}\text{m}^3\text{s}^{-1}$	9.15 <sup>**</sup>	T / K	310	$D_{S_2}/10^{-9}\text{m}^2\text{s}^{-1}$	9.56 [137]
$K_{22}/\text{mol}^{-1}\text{m}^3\text{s}^{-1}$	6945 <sup>**</sup>	$\omega / \text{rad s}^{-1}$	41.87	$D_{S_2}^{\text{CL}}/\text{m}^2\text{s}^{-1}$	<b>Table 5-4</b>
$k_{e0}/10^{-4}$	18 <sup>**</sup>	C / mol m <sup>-3</sup>	0-20	$D_{\text{Mox}}/10^{-9}\text{m}^2\text{s}^{-1}$	8.61 <sup>**</sup>
$m_{\text{geo}}^3 m_{\text{act}}^{-2} \text{s}^{-1}$					
$C_{\text{Mt}}/\text{mol m}_{\text{geo}}^{-3}$	<b>Table 5-4</b>	E vs. SHE / V	0.04-0.44	$D_{\text{Mox}}^{\text{CL}}/\text{m}^2\text{s}^{-1}$	<b>Table 5-4</b>
$C_{\text{E2t}}/\text{mol m}_{\text{geo}}^{-3}$	<b>Table 5-4</b>	$R_{\text{ohm}}/\Omega$	89	$\kappa_{\text{E}}/S\text{m}_{\text{geo}}^{-1}$	400
				$\kappa_{\text{I}}/S\text{m}_{\text{geo}}^{-1}$	0.5
		<b>Structural [measured, adopted]</b>		<b>Thermodynamic</b>	
		L / $\mu\text{m}_{\text{geo}}$	<b>Table 5-4</b>	$E_r$ vs. SHE / V	0.394 [95]
		$\epsilon / \text{m}^3\text{m}_{\text{geo}}^{-3}$	0.3	$\alpha$	0.5
		a/ $\text{m}_{\text{act}}^2\text{m}_{\text{geo}}^{-3}$	<b>Table 5-4</b>		

<sup>\*\*</sup> adopted values from previous simulation

The steady state experimental data and the simulated data of the FM1 model for the thin and thick Gelatin electrodes (20  $\mu\text{L}$  and 50  $\mu\text{L}$  of ink loading respectively) at different glucose concentrations are presented in Figure 5-6. An excellent fit between the simulation and the experimental data can be seen for the thin electrode. At the same set of optimized parameters, the model was able to predict qualitatively the steady state behaviour of the thick electrode in the whole applied potential range. The deviation between simulated and experimental data is more obvious at the higher range of potentials, which was designated with a higher residue value ( $\chi^2=114$ ). This can be explained by the different process interactions/parameters from i.e., the electrochemical active surface area and enzyme and material agglomeration at the higher applied potential range. None of these influences was incorporated in the simulation. The

steady state performance of the thin and thick electrode at the higher potential range is similar due to the similar effective working CL in both systems (Figure 5-6b). The behaviour of the thin electrode is similar to the PVDF system reported in the previous section. At pH7, 37°C, the steady state performance of these electrodes can reach ca.  $9 \text{ A m}_{\text{geo}}^{-2}$  at 5 mM of glucose concentration and ca.  $30 \text{ A m}_{\text{geo}}^{-2}$  at 20 mM of glucose concentration.

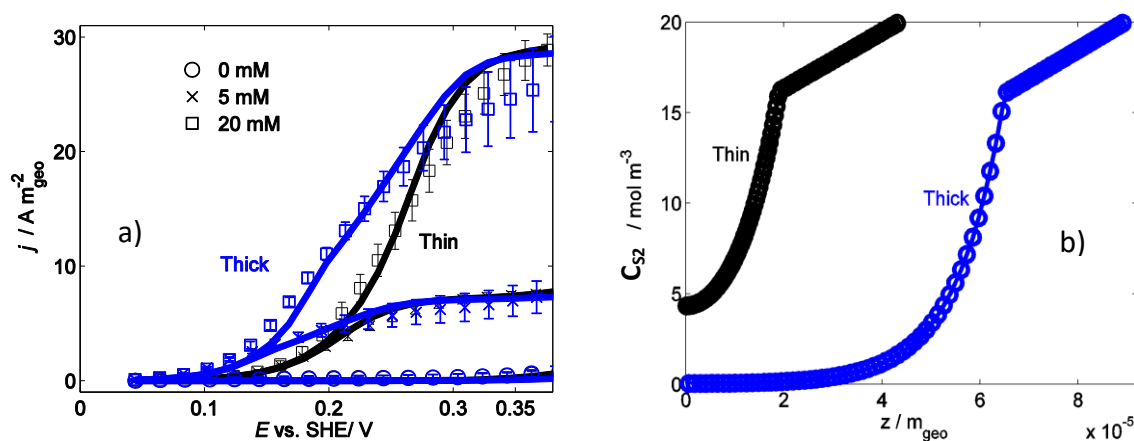


Figure 5-6: a) Steady state polarization curves of the Gelatin thin and thick porous electrodes: symbols – experimental data, lines – simulated curves electrode b) simulated local profiles of glucose concentration for a thin (in black) and a thick (in blue) porous electrode along spatial coordinate  $E=0.384 \text{ V}$ . Conditions: ratio in mg of Vulcan-TTF-enzyme (20-10-0.5), fixed delay of 2 minutes, glucose concentrations from 0 mM to 20 mM, temperature 37 °C; rotation rate 400 rpm, pH7 with other parameters given in Table 5-3 and Table 5-4.

The obtained optimized parameters are shown in Table 5-4. Assuming that the kinetic constants of the enzymatic steps are not affected by the structural parameters, the number of active enzymes in the thin electrode at lower nominal loading (0.5 mg/ml for the Gelatin system and 6 mg/ml for the PVDF system) is comparable with amount of active enzymes in the PVDF electrode (0.068 mol and 0.07296 mol). It also means that the thin electrode works more effectively. With the thick electrode, the utilization is ca 3 times higher than its value in the PVDF system, connecting directly to the amount of active mediator used in the system. The active electrochemical surface area (in  $\text{m}_{\text{act}}^2$ ) of the Gelatin electrode is in the same magnitude and a little higher than its value in the PVDF system. Potentially, the different arrangement of TTF in the Gelatin system would allow more electrochemical active materials to access the TTF molecules. The result is that the active mediator concentration in the PVDF system is lower

than that of the thick electrode and comparable to the thin electrode. The diffusivity of mediator and glucose in the Gelatin environment ( $5.6 \times 10^{-10} \text{ m}_{\text{geo}}^2 \text{ s}^{-1}$  and  $2.7 \times 10^{-11} \text{ m}_{\text{geo}}^2 \text{ s}^{-1}$  respectively) is smaller than these values in the corresponding bulk solutions.

**Table 5-4: Optimized parameters of the GOx modified TTF-Gelatin electrodes, pH7, 37°C**

Parameter	20 $\mu\text{L}$	50 $\mu\text{L}$
$L/10^{-6} \text{ m}_{\text{geo}}$	19	65
$a/10^4 \text{ m}_{\text{act}}^2 \text{ m}_{\text{geo}}^{-3}$	1.8	1.8 <sup>**</sup>
$C_{\text{E2t}}/\text{mol m}_{\text{geo}}^{-3}$	0.1136	0.1136 <sup>**</sup>
$n_{\text{E2t}}/10^{-9} \text{ mol}$	0.068 <sup>++</sup>	0.2087 <sup>++</sup>
$C_{\text{Mt}}/\text{mol m}_{\text{geo}}^{-3}$	4.3	4.3 <sup>**</sup>
$n_{\text{Mt}}/10^{-9} \text{ mol}$	2.3 <sup>++</sup>	7.8 <sup>++</sup>
$D_{\text{S2}}^{\text{CL}}/10^{-10} \text{ m}_{\text{geo}}^2 \text{ s}^{-1}$	5.6	5.6 <sup>**</sup>
$D_{\text{Mox}}^{\text{CL}}/10^{-10} \text{ m}_{\text{geo}}^2 \text{ s}^{-1}$	2.7	2.7 <sup>**</sup>
$\chi^2$	59.73	114

<sup>\*\*</sup> adopted values from previous simulation, <sup>++</sup> calculated values

As can also be seen in Figure 5-6a, the thick electrode steady state performance shows a shift of onset potential in comparison to the thin electrode. In addition, the behaviour of the thin electrode is somewhat similar to the PVDF system. As shown in the parameter analysis, this dependence is due to the contribution of several factors, such as active mediator concentration, enzyme utilization and the active surface area. The optimized parameters show a similar parameter range of the thin electrode and the PVDF system. Interestingly, the increase in the ink loading can only improve the system performance at lower potentials. At higher potentials, the thin electrode provided better performance due to better CL utilization. The thick electrode is anticipated to have a higher mass transport limitation. A significant limitation of this type inside the CL of the thick electrode, especially at the higher potential range, can be seen in Figure 5-6b. The behaviour in the transient and spatial profiles is similar to that in the PVDF procedure. This limitation results in the comparable effective CL utilized in the thick and the thin electrodes (Figure 5-6b). This is also indicated in the similar performance of the thin

and thick electrodes in the higher over-potential range. Therefore, the use of an appropriate amount of materials to achieve optimal interaction between the different processes is one of the important strategies for an efficient biocatalyst used in different applications of bio-electrochemical systems. For example, the thick electrode should be utilized for better performance at the lower potential range, but the thin one should be a better candidate at the higher potential range.

### **Implications**

The distributed model had been applied successfully to study the behaviour of the same enzymatic porous system using Gelatin as a binder. The mass transport limitation is more pronounced for the thick electrode at higher potentials, which is revealed by the concentration profiles of the substrate along the spatial coordinate at a high concentration of glucose. The similar performance of the thin and thick electrodes at the higher potential range can be ascribed to the similar effective CL in both electrodes. A shift of onset potential can be observed between the thin and thick electrodes due to the different catalyst loadings. At lower potentials, the thick electrode provides better performance, mainly due to higher mediator/catalyst utilization. This provides very useful and interesting information for different applications of the studied system.

#### **5.2.1.3 Influence of thickness on electrode performance**

An additional simulation was conducted to show the dependence of electrode performance on electrode thickness, disregarding the influence of other factors. The simulation result is shown in Figure 5-7 for 5 mM and 20 mM of glucose concentration. This condition can be realized experimentally by only varying the ink loading. In general, increasing the thickness improves the electrode performance due to the increasing number of catalysts and mediators inside the CL. However, this is not always the case; increasing the electrode thickness up to a certain value ( $> 65 \mu\text{m}$ ,  $0.16 \text{ V} < E < 0.26 \text{ V}$ ) does not enhance electrode performance due to the control of the electrochemical step. At the higher range of potentials ( $E > 0.26 \text{ V}$ ), a very thick electrode has the worst performance due to the higher resistance for the mediator diffusion out of the CL and the mass transfer limitation of glucose in the CL.

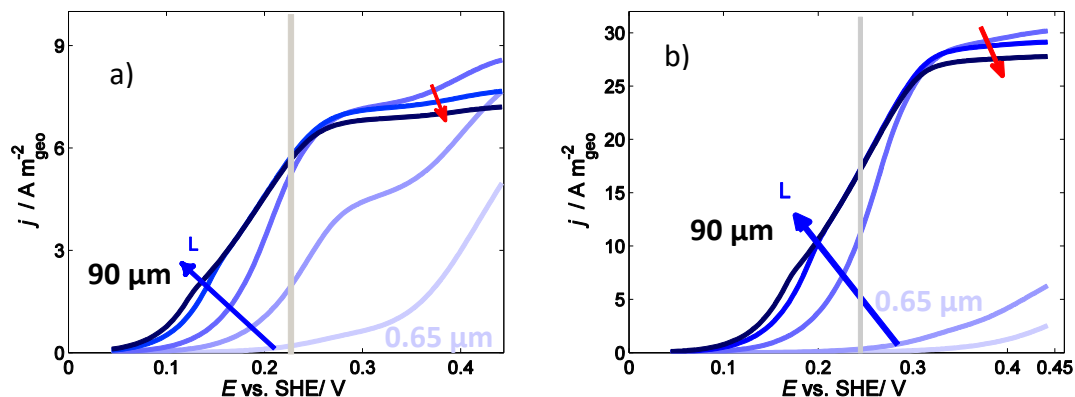


Figure 5-7: Simulated steady state response of the model showing the influence of thickness on the GOx modified TTF-Gelatin electrodes. a) at 5 mM, b) at 20 mM. Conditions: temperature of 37 °C, and rotation rate of 400 rpm, with other parameters given in Table 5-3 and Table 5-4

#### 5.2.1.4 Influence of enzyme and mediator on electrode performance using the Gelatin procedure

The Gelatin procedure was used to analyse the influence of mediator and enzyme on electrode behaviour due to its stability over a longer time experimental period and as it has less impact on the oxidized mediator diffusivity at the higher range of applied potential. Changing both quantities individually can have different impacts on the performance, as can be seen in the theoretical analysis in section 5.2.1.1.3. Experimentally, the effect can be altered due to the non-ideality of the system and the interaction among many other processes.

Changing the mediator loading individually has an impact directly on the amount of active mediator, electrochemical surface area, porosity, and thickness of the working electrode. As can be seen from previous sections, the amount of active mediator and electrochemical active surface area required for electrochemical purposes is small in comparison to the nominal one. Therefore, variation of mediator can be neglected in the studied condition. Porosity and the thickness should be considered in the modelling.

Enzyme loading can have an impact not only on the amount of active enzyme but also on the porosity. The impact of enzyme loading on the porosity is more significant in comparison to mediator loading due to its smaller size and the possibility of enzyme agglomeration inside the

CL. This reliance is more significant at higher potentials. The calculated value of porosity varies from 0.13-0.30, corresponding to enzyme loading from 0.5 mg-20 mg.

Taking into account these influences, two possibilities can be proposed to study electrode behaviour by changing both nominal loadings. The first takes into account linear thickness changing with the nominal loading, while the second considers a change in porosity. Different SEM images on different material loadings for the lower ink loading were analysed and show the change in CL thickness layer in the approximate range of 15-21  $\mu\text{m}$ , with the total material loading staying in the range of 0.6 mg to 1 mg. Since the total material loading for the thin electrode lies experimentally between 0.6-0.9 mg, the thickness of CL is subject to linear change within the studied range.

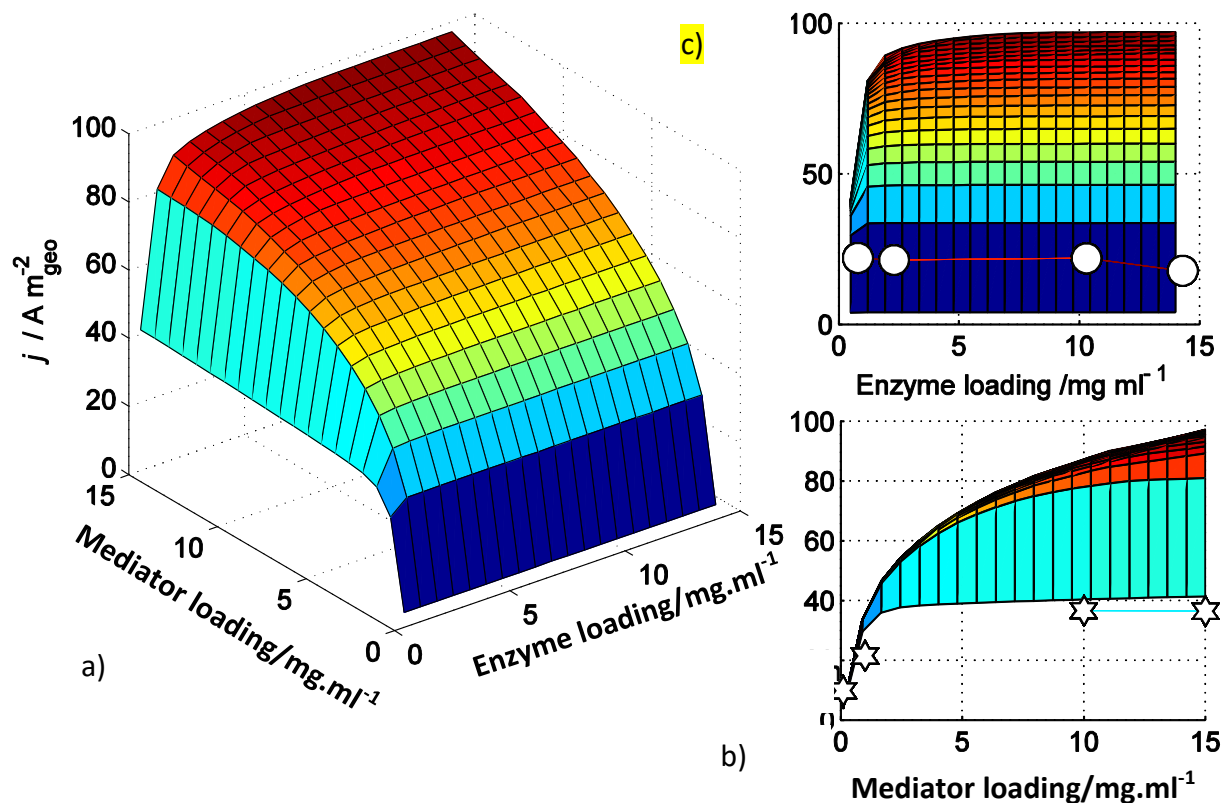


Figure 5-8: Dependence of electrode performance with the change in the electrode thickness on a) TTF and GOx loading; b) enzyme loading (projection from a); and c) mediator loading (projection from a). Spectra: simulation, symbols: experimental data. Other conditions:  $E=0.3844$  V vs. SHE fixed delay of 2 minutes, glucose concentration of 20 mM, temperature 37 °C; rotation rate 400 rpm, pH7, porosity ( $\epsilon$ ) 0.35, with other parameters given in Table 5-3 and Table 5-4

For the first case, the simulated data without considering the influence of porosity on the variance in enzyme and mediator loadings is presented in Figure 5-8. As can be observed in Figure 5-8, optimal electrode performance can be achieved at the highest loading of mediator and enzyme. This condition does not agree with the experimental observation that the optimal electrode was obtained at the 20.10.10 ratio (Figure 5-8). The simulation only provides qualitative agreement in the case of changing mediator loading and the simulation data is much higher than the measured data. There is a qualitative deviation in the experimental data and simulation at the last point (ratio 25.10.15), which can be explained by the lower catalyst utilization, the change in porosity and agglomeration with the increase in enzyme amount.

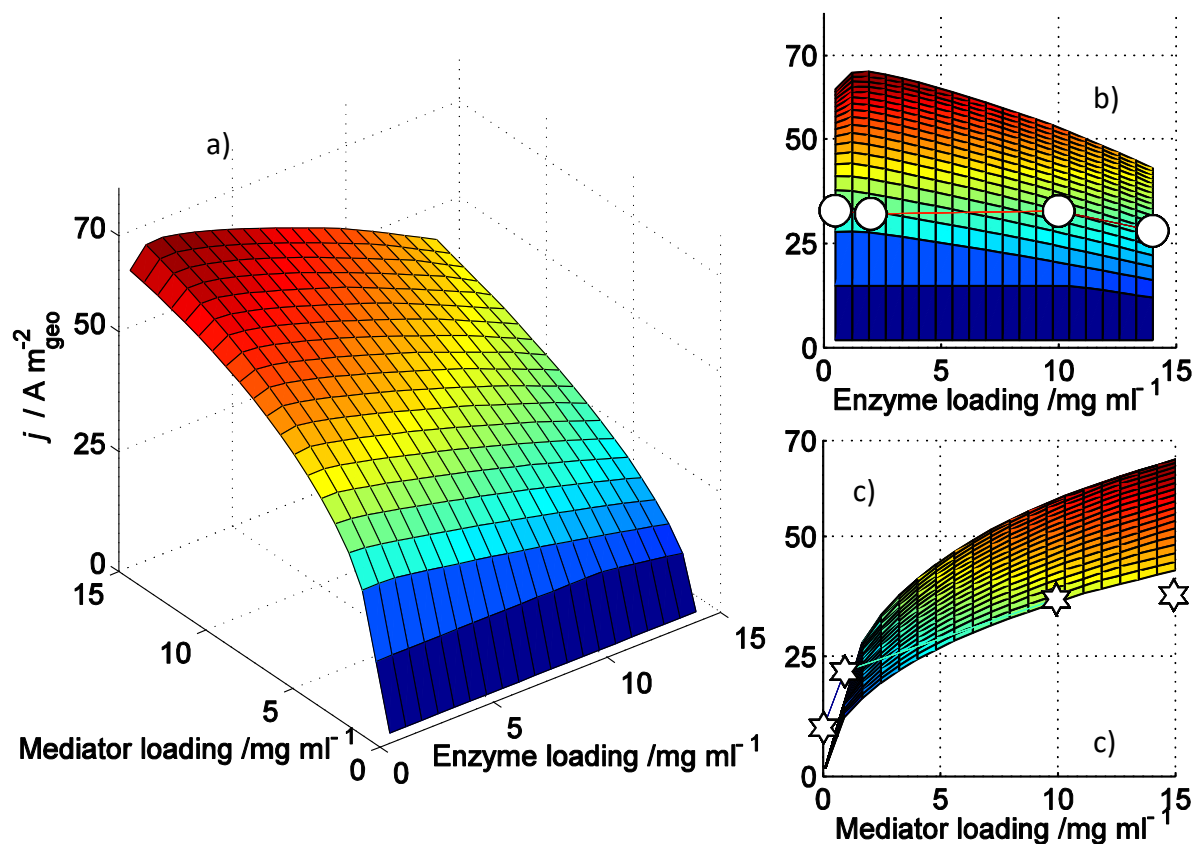


Figure 5-9: a) Dependence of thin electrode performance with changing porosity on a) TTF and GOx loading; b) enzyme loading; and c) mediator loading. Spectra: simulation, symbols – experimental data at the loading of 20.10.10 ratio. Other conditions:  $E=0.3844$  V vs. SHE,  $20 \mu\text{L}$  of ink loading, fixed delay of 2 minutes, glucose concentration of 20 mM, temperature  $37^\circ\text{C}$ ; rotation rate 400 rpm, pH7, with other parameters given in Table 5-3 and Table 5-4

The additional simulation, taken into account the change in porosity, with the change in enzyme loading has made and shown in Figure 5-9. As can be seen in Figure 5-9a, electrode performance reaches an optimal value at the highest mediator loading, enzyme loading at 10 mg/ml and porosity at 0.3, corresponding to the experimental conditions that we achieved for the Gelatin porous electrode. By taking into account the influences of the enzyme loading on porosity, the simulated electrode performance decreases with the increase in enzyme loading (Figure 5-9). The experimental data also reflects a trend similar to the simulation. The simulated electrode performance and experimental data qualitatively agree (Figure 5-9c). However, the



experimental data shows a lower value in comparison to the simulated data in both cases due to the theoretical higher enzyme/mediator utilization in the simulation.

At high enzyme loading, the MET electrode performance is likely to be more dependent on the structural parameters. Therefore, a strategy for improvement would be a better selection of mediator (i.e. decreased size, or alternative type of mediators) or the better design of the electrode structure (control particle size, or material structure).

### **Implications**

In general, the enzyme and mediator utilizations compared to the nominal loadings in the MET electrode are low. Increasing enzyme /mediator loading does not always improve electrode performance due to the interaction between different parameters; i.e., porosity, thickness, agglomeration, active mediator concentration inside the system and the contribution of non-ideality to the system. For example, increasing enzymes possibly create enzyme agglomeration/filling up of pores and, in turn, decrease the porosity. Therefore, dependence of applications, and different experimental design under different enzyme and mediator loadings could be useful. Design of a better electrode structure to improve mass transport in the system, and better selection of mediator, are improved strategies for the porous enzymatic MET system.

#### **5.2.2 Porous electrode with O<sub>2</sub> supply**

This section evaluates the influence of O<sub>2</sub> on the PVDF electrode using GOx in the presence of glucose. Figure 5-10 shows the steady state behaviour of the studied electrodes with and without consideration of the inhibition of the intermediate H<sub>2</sub>O<sub>2</sub> on the reduced form of GOx. As can be seen, the mathematical model characterized well the experimental data at 5 mM and 20 mM glucose concentration. As already mentioned in the previous sections, a higher O<sub>2</sub> concentration in the system is a disadvantage for enzyme activity due to the formation of irreversible enzyme inactive compound (E<sub>2</sub>I) between GOx and H<sub>2</sub>O<sub>2</sub>. The irreversible inhibition consumes GOx and thus reduces the number of active enzymes. In order to see the effect of this phenomenon, the simulation included an enzyme inhibition step was also made (Table 3-7). As we can see in Figure 5-11a in the red line, there is insignificant influence of enzyme inhibition by H<sub>2</sub>O<sub>2</sub> on electrode performance. This is mainly a consequence of the small amount

of H<sub>2</sub>O<sub>2</sub> production, which does not have a big impact on the amount of reduced GOx forming the inactivate substance. According to Kleppe [118], the inactivation of GOx due to H<sub>2</sub>O<sub>2</sub> plays a role at higher H<sub>2</sub>O<sub>2</sub> concentration, which is higher than the concentration of H<sub>2</sub>O<sub>2</sub> available in the studied system.

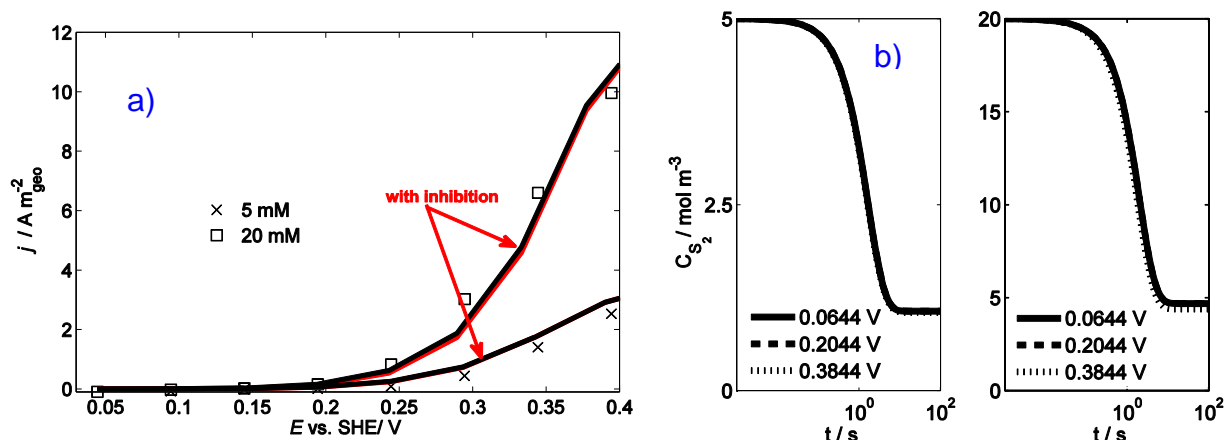


Figure 5-10: a) Steady state polarization curves of MET porous electrode with PVDF procedure with O<sub>2</sub> supply: symbols – experimental data, lines – simulated curves b) simulated transient profiles of glucose concentration at 5mM and 20 mM. Conditions: ratio of Vulcan-TTF-enzyme (20-10-10), fixed delay of 2 minutes, temperature 25 °C, pH6, rotation rate 400 rpm, with other parameters given in Table 5-1, Table 5-2 and Table 5-6

The simulated parameters corresponding to the relevant steps are similar to the Gelatin or PVDF procedures and are extracted from previous related sections (Table 5-1, Table 5-2). The remaining fitting parameters are the kinetic constants of the O<sub>2</sub>-enzyme and inhibition steps; the fitted  $K_{33}$  value is  $252 \text{ m}_{\text{geo}}^3 \text{ mol}^{-1} \text{ s}^{-1}$ ; and the estimated  $K_{44}$  value is  $0.002 \text{ m}_{\text{geo}}^3 \text{ mol}^{-1} \text{ s}^{-1}$ . For further simulations, we neglected enzyme inhibition due to H<sub>2</sub>O<sub>2</sub> since it has a negligible influence on electrode performance.

Table 5-5: Optimized parameters in the presence of O<sub>2</sub>.

Parameter	No Inhibition	inhibition
$K_{33} / \text{m}^3 \text{ mol}^{-1} \text{ s}^{-1}$	252	252**
$K_{44} / \text{m}^3 \text{ mol}^{-1} \text{ s}^{-1}$	0	0.002

\*\* adopted values from previous simulation

The simulated transient and steady state concentration profiles of glucose at a fixed point in the CL (end point) are presented in Figure 5-10b. From Figure 5-10b, the glucose concentration is polarized at both concentrations (5 mM and 20 mM). However, its behaviour is independent of the applied potentials, possibly due to the controlling enzymatic steps. At lower potentials, the glucose concentration was dropped mainly due to the participation of  $O_2$  in the catalytic cycle to produce  $H_2O_2$ . At higher applied potentials, due to the higher speed of the electrochemical reaction which requires a more reduced form of GOx, the glucose concentration profile is steeper. Compared to the case of no  $O_2$  supply, the depletion level of glucose concentration is higher with an  $O_2$  supply, indicating a fast consumption of glucose due to the additional reaction between  $O_2$  and reduced GOx.

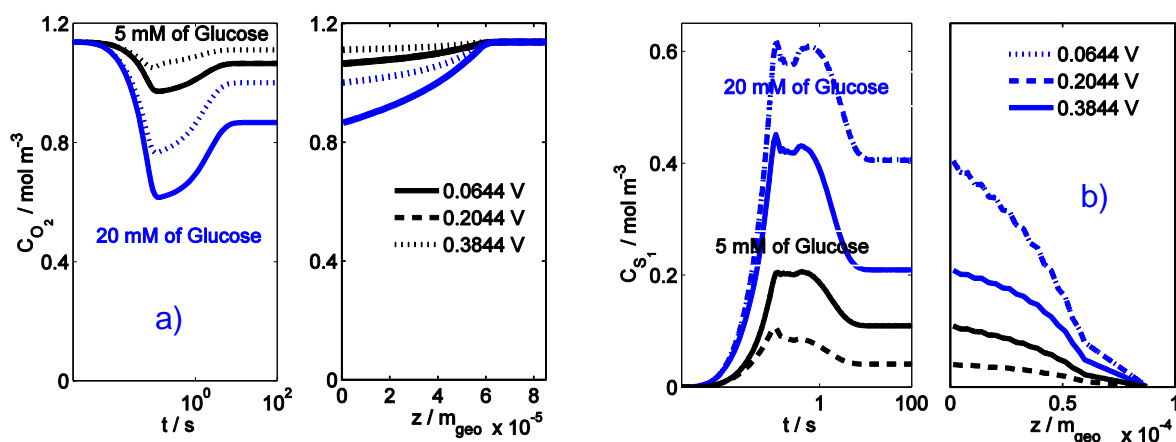


Figure 5-11: Simulated transient (at fixed position in the middle of CL) and steady state (along spatial coordinate) profiles of glucose concentration at different applied potentials a)  $O_2$  and b)  $S_1$  ( $H_2O_2$ ). Conditions: temperature  $25^\circ\text{C}$  pH6, rotation rate 400 rpm, with other parameters given in Table 5-1, Table 5-3 and Table 5-6

The  $O_2$  concentration profiles are shown in Figure 5-11a. The potential dependence of the profiles is more visible at the lower range of potentials.  $O_2$  consumption is higher at 20 mM due to the higher amount of reduced GOx in the system. The dynamic profile initially shows a decrease, then an increase, and reaches a steady state at ca. 30 s.

The dynamic change in  $H_2O_2$  at a fixed point in the CL and the spatial concentration profile are shown in Figure 5-11b. More  $H_2O_2$  is produced at the higher range of potential, which is the consequence of the electrochemical controlling step. The amount of  $H_2O_2$  produced in the

system is also higher at a higher glucose concentration (20 mM). The accumulation of  $H_2O_2$  increases in line with a decrease of the CL thickness, which is evidence of the higher availability of the reduced form of GOx for the  $O_2$  reduction reaction.

### Implications

The distributed model was employed further to study the behaviour of the similar system in the presence of  $O_2$ . The presence of  $O_2$  decreased the performance of the electrode using GOx and TTF more at 5 mM than at 20 mM, pH6. At the lower potential range, the GOx regeneration speed by  $O_2$  is faster than the mediator regeneration, while this behaviour is comparable at the higher range of the applied potentials. Inhibition contributes insignificantly and therefore can be neglected in the following study cases.

### 5.3 Enzymatic cathode

As discussed in section 3.4, the interface model is firstly used to extract the kinetics and relevant parameters. These are plugged into the porous electrode model using the same enzyme (HRP). To justify the compatibility of using these parameters for the respective porous electrode, an ultra-thin film electrode was prepared (section 4.2.2.1). The experimental steady state polarization at 80  $\mu$ M and 160  $\mu$ M shows similar activity to the flat graphite electrode. To further prove the hypothesis, the reduced 1-D model was used to simulate the behaviour of this electrode, assuming no appearance of a concentration gradient in the ultra-thin film electrode. This condition can be created by setting an infinitely large diffusion coefficient of  $H_2O_2$  in the CL. The same kinetic parameters and enzyme coverage as in the graphite electrode are used for the simulation. The simulated data reflects very well the experimental data, indicating that the immobilization conditions on the ultra-thin film PVDF electrode are similar to those on the interface electrode (data not shown here). This also supports the assumption that the intrinsic enzymatic kinetics in the case of physical adsorption in the porous electrodes remains largely unchanged. The Vulcan-PVDF system is more suitable for adopting this assumption because of the possible impact of cross-linking on enzyme kinetics in the Vulcan-Gelatin system.

At a given enzyme coverage per active surface area ( $\Gamma_{E1t}$ ), the total number of enzymes can be estimated using the following equation:

$$n_{E1t} = \Gamma_{E1t} a A_a L \quad (245)$$

The inhibition of H<sub>2</sub>O<sub>2</sub> in the catalyst cycle can be significant at a higher range of substrate concentration [129]. To decrease this influence, the lower range of substrate concentration (<500mM) is restricted. The higher range of substrate is subsequently considered to study the influence of the inhibition of substrate in the electrode performance.

It should be mentioned here that a similar hierarchical approach to kinetic parameter determination cannot be adopted for the case of MET enzyme due to the impossibility of designing an equivalent system. The following presents the kinetic determination of the enzymatic electrode using the interface model, and simulation of the porous electrode using the HRP and the enzymatic cascade GOx-HRP.

### 5.3.1 Thin film electrode

This section focuses on the interface mode of the thin film electrode system using HRP as a DET enzyme. Three different proposed models (M<sub>1</sub>, M<sub>2</sub>, M<sub>3</sub>) were presented in section 3.4.1.1. The analytical solutions of the three models at steady state and EIS were derived and discriminated. The thermodynamic parameters (formal potentials of the electrochemical steps) were extracted from the literature [143-144], while the kinetic parameters were obtained by matching the experimental data with the simulation on the surface electrode using steady state and electrochemical impedance spectroscopy (EIS) techniques. Before discussing the results, the parameter determination is addressed in brief.

#### 5.3.1.1 Steady state polarization

As can be anticipated from the equations presented in Table 3-9 and Table 3-10 under steady state conditions, the rate constants of the two electrochemical steps ( $k_{e1}$ ,  $k_{e2}$ ) described by BV formalism cannot be determined separately, but instead by a lumped effective rate constant ( $k_e$ ). This effective constant is controlled by the rate of the slower step. It is similar for the enzymatic constants; from the three enzymatic kinetic constants only  $k_{cat}$  and  $K_m$  can be determined independently, while  $k_1$  and  $k_{-1}$  are lumped together as the  $K_m$  value.

Figure 5-12 shows the steady state behaviour of the three different models and the experimental data with error bars at two different pHs (pH5 and pH6) and different  $\text{H}_2\text{O}_2$  concentrations (ranging from 10  $\mu\text{M}$  to 80  $\mu\text{M}$ ). Experimentally, the error bars are greater at a higher  $\text{H}_2\text{O}_2$  concentration and higher pH value, reflecting the possibility of enzymes leaching during the experiment course and pH dependence on the enzyme orientation. In addition, the performance is higher at pH5 than at pH6. This performance holds true at a higher range of applied potential, which is potentially contributed by the pH favourable dependence of the electrochemical steps.

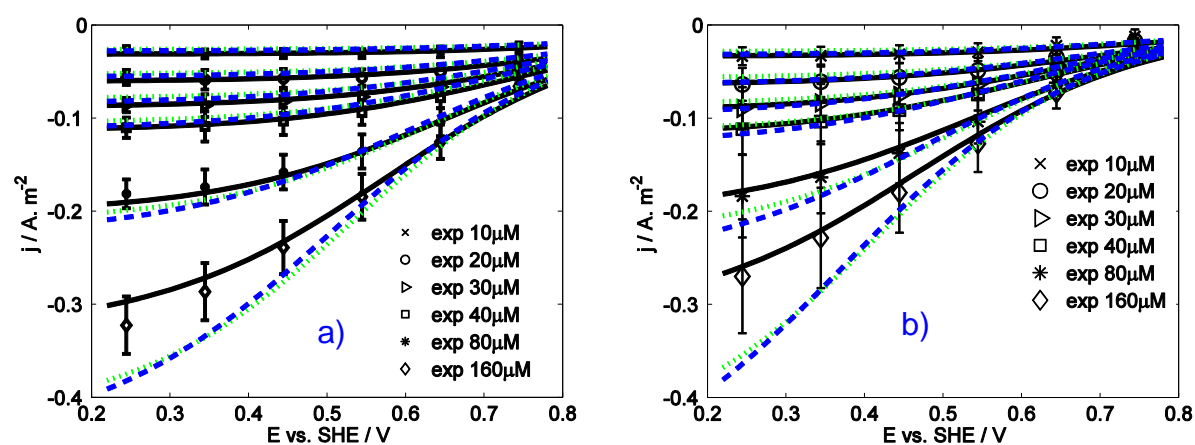


Figure 5-12: Steady state polarisation curves at a) pH5 and b) pH6 for  $\text{H}_2\text{O}_2$  reduction on HRP modified graphite electrode; symbols – experimental data and lines – simulated curves ( $M_1$  – blue dotted line,  $M_2$  – green dashed line and  $M_3$  – black solid line). Conditions: fixed delay of 1 minute,  $\text{H}_2\text{O}_2$  concentrations from 10 to 160  $\mu\text{M}$ , room temperature; rotation rate 400 rpm; with the parameters for the simulations given in Table 5-7

As can be seen in Figure 5-12, all three models agreed qualitatively with the experimental data. Among them, the best quantitative fit was obtained by  $M_3$ . The steady state behaviour of the two models  $M_1$  and  $M_2$  is almost similar, which indicates the insignificant contribution of proton and substrate transport in them. However,  $M_3$ , which takes into account the ES formation step, shows better quantitative agreement with the experimental data in different cases, according to  $\chi^2$  presented in Table 5-7.

As mentioned in the previous section, enzyme concentration is very important for parameterization. Therefore, a literature survey was carefully made to select a reasonable

initial value. Taking into account the fact that not all absorbed enzymes can contribute to the DET and the graphite was used as a supporter, the low value of  $0.1 \text{ pmol cm}^{-2}$  was chosen as the initial value. This corresponds to the study of Andreu et al [128].

The optimized parameters are shown in Table 5-7. As can be seen, enzyme coverage at pH6 is slightly higher than the value at pH5. This difference is probably due to differences in enzyme orientation at different pH values, but it can be also a random effect, as discussed by Andreu et al [128]. The behaviour of  $M_1$  and  $M_2$  almost coincides, but the optimized enzymatic kinetic constants are not identical. The higher values of parameters in the case of  $M_2$  can probably be considered to be more precise, since the substrate concentration at the electrode surface shows a small dependence on mass transport conditions. The electrochemical constants ( $k_e$ ) are similar for both models, but they show some pH dependence.

With the initial values provided, the final optimal coverage enzyme value was  $0.3 \text{ pmol cm}^{-2}$ , which is relatively small, as concluded from the work of Ruzgas [126]. The results also indicate lower activity of the immobilized enzymes compared to the enzymes in the solution. The consequence of low enzyme coverage is that the  $K_1$  values reported in the present paper are more than 100 times bigger ( $5.58 \times 10^6 \text{ M}^{-1} \text{ s}^{-1}$ ) based on  $M_1$  and ca. ( $7.2 \times 10^6 \text{ M}^{-1} \text{ s}^{-1}$ ) based on  $M_2$ , and closer to the value reported for the enzyme in the solution (Table 5-6).

The rate constants of the electrochemical steps in this study were defined as second order constants. In steady state conditions, only one effective electrochemical rate constant  $k_e$  in accordance to (Eq. (191)) can be determined. This value was multiplied by proton concentration, giving an apparent electrochemical rate constant with values in the range from  $27.74 \text{ s}^{-1}$  at pH 5 to  $17.4 \text{ s}^{-1}$  at pH6 (Table 5-7). The value also reflects the proportional dependence of rate constants on pH [145]. The higher value at pH5 might indicate more favourable enzyme orientation to the electrode surface. The pH dependence of the apparent electrochemical reaction rate constant was also obtained in the work of Ferapontova and Gorton [130].

Table 5-6: Kinetic constants  $K_{11}$  on different studied systems in the literature

Type of electrode	Enzyme coverage	$K_{11}$	Literature
Graphite	40 pmol cm <sup>-2</sup>	0.039 - 0.014.10 <sup>6</sup> M <sup>-1</sup> s <sup>-1</sup>	[126]
Graphite coating	14 pmol.cm <sup>-2</sup>	0.031- 0.014.10 <sup>6</sup> M <sup>-1</sup> s <sup>-1</sup>	[146]
Gold	23 pmol.cm <sup>-2</sup>	0.13-0.02.10 <sup>6</sup> M <sup>-1</sup> s <sup>-1</sup>	[130]
In solution	N/A	15 10 <sup>6</sup> M <sup>-1</sup> s <sup>-1</sup>	[126]

In the full model ( $M_3$ ), the enzymatic kinetic constants  $K_m$  and  $k_{cat}$  were obtained. Similar to other kinetic constants, the low enzyme coverage results in a  $k_{cat}$  value of 1898 s<sup>-1</sup> and  $K_m$  of 0.21 mM at pH 5, while  $k_{cat}$  is 1202 s<sup>-1</sup> and  $K_m$  is 0.20 mM at pH 6. As can be seen, these kinetic values between the models are of the same magnitude, pH independent and lower than the values assumed by Andreu et al [128]. A similar magnitude of electrochemical rate constants (pH 5 and pH 6) for the three models was obtained. The value of the electrochemical rate constant is higher than its value in the reported works (ranging from 0.66 - 0.28 s<sup>-1</sup>) at the similar studied condition in similar conditions [128]. The deviation of these values from those in the literature can be explained by the difference in experimental working range (potentials), the different rate expression (Tafel) and the catalytic properties of electrode materials in these studies.



**Table 5-7: Optimized parameter values based on steady state data for all three models under different conditions of pH and H<sub>2</sub>O<sub>2</sub> concentrations**

Parameters	pH5			pH6		
	M <sub>1</sub>	M <sub>2</sub>	M <sub>3</sub>	M <sub>1</sub>	M <sub>2</sub>	M <sub>3</sub>
$\alpha$	0.17	0.17	0.17	0.17	0.17	0.17
$K_1/10^3 \text{ m}^3 \text{ mol}^{-1} \text{ s}^{-1}$	5.58	7.20	-	5.57	7.14	-
$k_{\text{cat}}/ \text{s}^{-1}$	-	-	1898	-	-	1202
$K_m/ \text{mol m}^{-3}$	-	-	0.21	-	-	0.20
$k_e/ 10^3 \text{ m}^3 \text{ mol}^{-1} \text{ s}^{-1}$	2.77	2.77	3.78	17.17	17.4	18.9
$k_e C_{H^+, \infty}/\text{s}^{-1}$	27.7 <sup>++</sup>	27.7 <sup>++</sup>	37.80 <sup>++</sup>	17.17 <sup>++</sup>	17.4 <sup>++</sup>	18.9 <sup>++</sup>
$\Gamma_t/10^{-13} \text{ mol cm}^{-2}$	2.61	2.61	2.20	3.0	3.0	3.1
$\chi^2$	0.0060069	0.005318	0.0015898	0.0124	0.01133	0.001979

<sup>++</sup>calculated (not fitted) values

In addition to already discussed kinetic parameters, the value of transfer coefficient  $\alpha$  has been also considered as a fitting parameter. The effective phenomenological coefficient  $\alpha$  value was 0.17 (Table 5-7) independent on the models used for the data fitting. This value corresponds also to the literature finding [128].

### 5.3.1.2 Electrochemical impedance spectroscopy

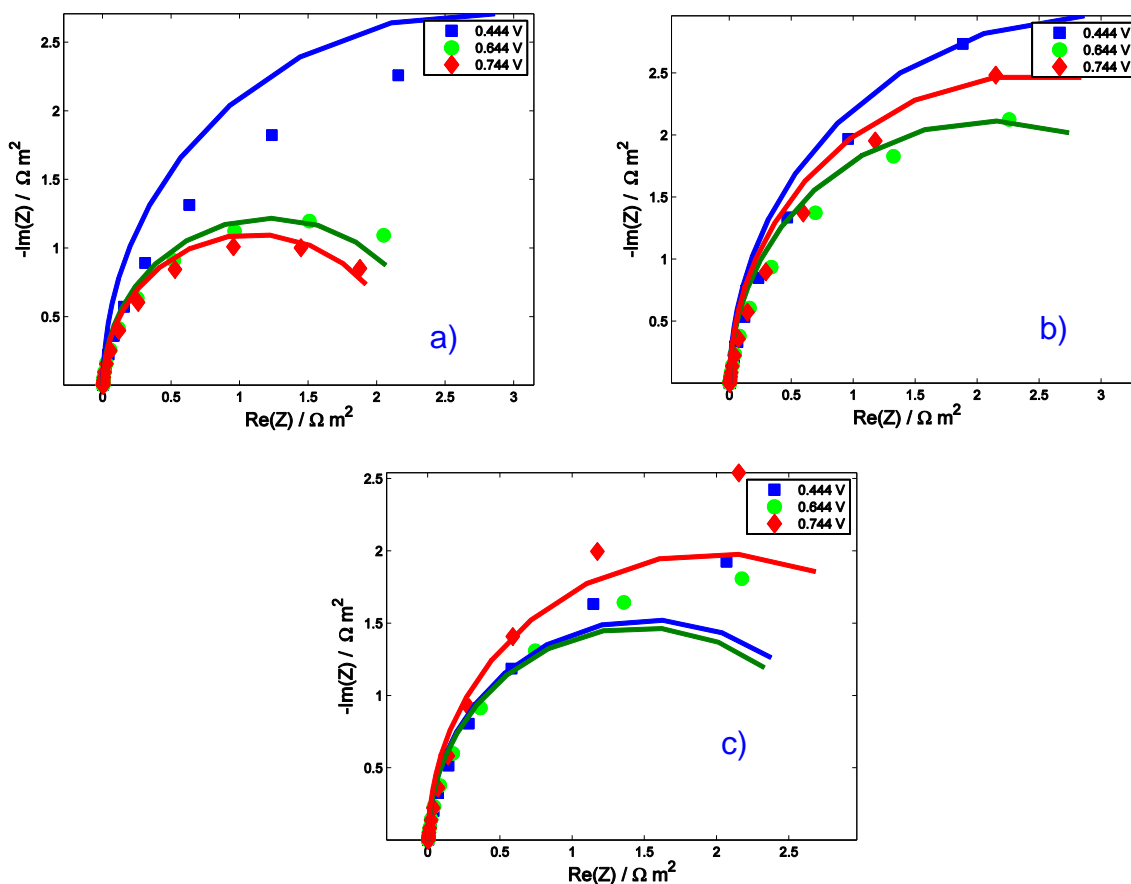


Figure 5-13: Experimental EIS (symbols) vs. simulated (lines- $M_3$ ) at three potentials; a) pH5 at 80  $\mu\text{M}$   $\text{H}_2\text{O}_2$  concentration, b) pH6 at 80  $\mu\text{M}$   $\text{H}_2\text{O}_2$  concentration and (c) pH6 at 160  $\mu\text{M}$   $\text{H}_2\text{O}_2$  concentration. Other conditions: 25°C and rotation rate of 400 rpm, with other parameters as shown in Table 5-9

The steady state measurements have not been sufficient to discriminate between the different kinetic descriptions. The EIS is used due to its higher sensitivity, since the dynamic information of the studied system can be included [98]. The final analytical solution of  $M_3$  applied FRA is shown in section 3.4.1.2 and was restricted at the linear part, which known as the EIS. All unknown parameters were obtained by optimization using the same procedure as the steady state conditions. Some parameters, for instance electron transfer coefficient  $\alpha$  and the two enzymatic constants  $k_{\text{cat}}$  and  $K_m$ , were fixed at values as shown in Table 5-7. The initial input of the other kinetic parameters is at optimized values in steady state conditions. Despite the effort in fitting with the experimental data for the three models, only  $M_3$  was able to produce

quantitatively and qualitatively the experimental data at both pH values and different concentrations. Therefore, the following is a discussion of the behaviour of the  $M_3$  model.

The Nyquist plot of the theoretical electrochemical impedances for  $M_3$ , along with the experimental data at pH5 and pH6, different substrate concentrations and different applied potentials, are shown in Figure 5-14. Good agreement between the experimental data and the model can be obtained. It should be noticed here that the data at 80  $\mu\text{M}$  was used for parameter determination; the data at 160  $\mu\text{M}$  was simulated using the same parameter set obtained from fitting at 80  $\mu\text{M}$ , pH6. In addition, the higher weight ( $\sigma$ ) was given to the data points at lower frequencies due to its higher sensitivity to kinetic constants.

**Table 5-8: Optimized parameter values based on EIS data for  $M_3$  with different pH(s)**

Parameters	pH5	pH6
$\alpha$	0.17 <sup>**</sup>	0.17 <sup>**</sup>
$k_1/10^3 \text{ m}^3 \text{ mol}^{-1} \text{ s}^{-1}$	12.18	15.9
$k_{-1}/\text{s}^{-1}$	614 <sup>++</sup>	1962 <sup>++</sup>
$k_{\text{cat}}/\text{s}^{-1}$	1898 <sup>**</sup>	1202 <sup>**</sup>
$K_m/\text{mol m}^{-3}$	0.21 <sup>**</sup>	0.20 <sup>**</sup>
$k_{e1}/10^5 \text{ m}^3 \text{ mol}^{-1} \text{ s}^{-1}$	5.62	2.63
$k_{e2}/10^3 \text{ m}^3 \text{ mol}^{-1} \text{ s}^{-1}$	6.19	36.7
$k_e/10^3 \text{ m}^3 \text{ mol}^{-1} \text{ s}^{-1}$	6.12	32.2
$k_e C_{H^+, \infty}/\text{s}^{-1}$	61.2 <sup>++</sup>	32.2 <sup>++</sup>
$\Gamma_t/10^{-13} \text{ mol cm}^{-2}$	3.0	2.2
$\chi^2$	1.544	3.36

<sup>\*\*</sup> adopted values from previous simulation, <sup>++</sup> calculated values

The values of the corresponding parameters used for the simulation of the theoretical EIS are shown in Table 5-8. In general, these values are comparable to the parameters determined for the steady state models. As can be recognized, the EIS is more sensitive to model discrimination than the steady state response, which is also reflected in higher number of optimized parameters. The individual electrochemical constants support the finding that the

rate of the first electrochemical step is faster than the second one (at least 10 times). The sensitivity of theoretical impedance on this constant is lower compared to other constants at pH5 [100], while it is higher at pH6 (Figure 5-14). The total enzyme coverages are similar to those obtained from the steady state experiments. The effective electrochemical rate constant was calculated and was influenced mainly by the rate of the slower step (second electrochemical step), which is close the value in the steady state conditions. The enzymatic kinetic constants are slightly pH dependent, which might be considered as evidence of the pH influence on enzyme activity, as shown in [130]. These important contributions of the mass transport of  $H^+$  and ES forming step the system behaviour were neglected in  $M_1$  and as a result it was not possible to reproduce the experimental data.

The diameter of the semicircles approximating the total reaction resistance does not change uniformly with the change in applied potentials. Theoretically, an increase in imposed over-potential should result in a decrease in the total reaction resistance in the total resistance of the EIS response if the electrochemical step is the controlling step. This behaviour is due to the increase in the catalytic current and can be seen in the certain applied potential range. An example is the EIS at pH6 (both concentrations), and the potential range from 0.744 V to 0.644 V (complying with the direction of the increase in the overpotential). However, further increases in overpotential provide the opposite behaviour of the EIS, implying that the system is alternated by other limiting steps. The limiting step for the EIS at higher overpotential is more likely to be enzymatic reaction steps, since mass transfer resistance was not a significant contributor to the behaviour of  $M_1$  and  $M_2$ .

The parameter sensitivity analysis with respect to  $k_{cat}$  influenced the impedance response at pH6, 160  $\mu$ M of substrate concentration considering two limiting cases (0.1  $k_{cat}$  and 10  $k_{cat}$ ) is shown in Figure 5-14a. In the same way, the influence of the effective electrochemical rate constant  $k_e$  on the overall impedance response was simulated and is shown in Figure 5-14b. As can be seen in Figure 5-14a, the diameter of the EIS response is wider at low  $k_{cat}$  value due to the control of the enzymatic reaction rate in the whole range of the studied potentials. The behaviour is opposite in the case of a higher  $k_{cat}$  value because the electrochemical reactions become the rate limiting steps. The real case at pH 6 (Figure 5-13b) reflected clearly the

behaviour of these two limiting cases which was investigated theoretically of  $k_{\text{cat}}$ . The real case at pH 5 is more likely to indicate the prevalence of enzymatic reaction control in the whole range of investigated potentials. This is also reflected in the steady state response at pH 5 and 80  $\mu\text{M}$  (Figure 5-13a).

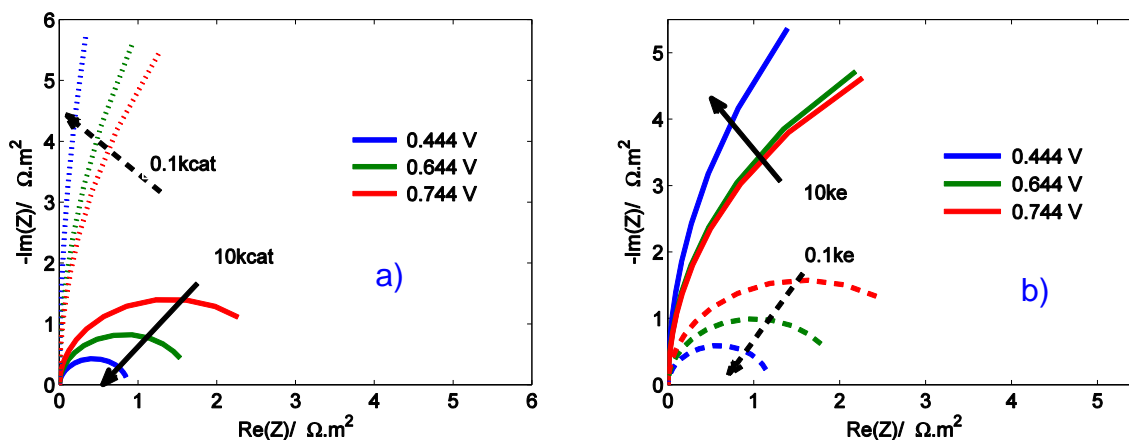


Figure 5-14: Simulated EIS of  $M_3$  showing the influence of the variation of the reaction rate constants with respect to their optimized values (Table 5-8) a) variation of  $k_{\text{cat}}$  at pH6 and b) variation of  $k_e$  at pH6. Other conditions: 160  $\mu\text{M}$   $\text{H}_2\text{O}_2$  concentration, room temperature, rotation rate 400 rpm.

### Implications

The steady state and EIS had been applied to study the kinetics of the system, where HRP as the biocatalyst was adsorbed physically on the graphite electrode. Three kinetic models were proposed with an increase in complexity from  $M_1$  to  $M_3$ . All the models can predict quantitatively the steady state experiments.  $M_3$ , considering the formation of the  $E_1S_1$  complex, was the best candidate to satisfy the description of the experimental data at the steady state conditions and EIS. A further investigation of the parameter influence on the impedance spectra was presented, which highlighted the complex interaction of the parameters on the EIS. The obtained set of parameters of  $M_3$  from EIS is used later for the respective porous electrode modelling. One of the obstacles of the system is the uncertainty of enzyme coverage, which influences all the kinetic constants (enzymatic and electrochemical constants). Therefore, a comparison with the literature values of similar systems operating in the same conditions is essential.

### 5.3.2 DET porous electrode with a single enzyme

Table 5-9: Model parameters of porous HRP modified electrodes.

Parameters			
Kinetic		Operating [measured]	
$k_1 / \text{m}^3 \text{mol}^{-1} \text{s}^{-1}$	$12.18 \times 10^{3**}$	T / K	298
$k_{-1} / \text{s}^{-1}$	614**	$\omega / \text{rad s}^{-1}$	41.87
$k_{\text{cat}} / \text{s}^{-1}$	1898**	C / $\text{mol m}^{-3}$	0.08-3.0
$k_{e1} / \text{m}^3 \text{mol}^{-1} \text{s}^{-1}$	$5.62 \times 10^{5**}$	E vs. SHE / V	0.244-0.644
$k_{e2} / \text{m}^3 \text{mol}^{-1} \text{s}^{-1}$	$6.19 \times 10^{3**}$	pH	5
Thermodynamic		Structural [measured, fitted]	
$E_{r,1}$ vs. SHE / V	1.05	L / $\mu\text{m}_{\text{geo}}$	47/ 53
$E_{r,2}$ vs. SHE / V	1.02	$\epsilon / \text{m}^3 \text{m}_{\text{geo}}^{-3}$	Table 5-10
$\alpha$	0.17**	a / $\text{m}_{\text{act}}^2 \text{m}_{\text{geo}}^{-3}$	Table 5-10

\*\* adopted values from previous simulation

Section 3.4.2 describes the mathematical model details of the porous DET electrode using HRP as enzyme. The model is used to describe the behaviour of the two electrodes prepared by the two preparation procedures, namely PVDF and Gelatin. Several groups of parameters, such as kinetic, operating, thermodynamic and structural ones, appear in this model and are listed in Table 5-9. In this table, the kinetic parameters are extracted from the kinetic model of the thin film electrode. Among the structural parameters, the void fraction and the internal active surface area were obtained by matching the experimental data, while the electrode thickness was determined from the SEM cross sections of the investigated electrodes. The thin electrode thickness was obtained by linearly scaling down the thick electrode thickness, following the assumption of the same porosity of both electrodes. In the Gelatin procedure, the diffusivity of substrate to CL was also considered as a fitting parameter due to the presence of the high diffusive resistance substance (Gelatin). As the upper limit of the diffusivity its value in the bulk solution has been assumed.

### 5.3.2.1 PVDF porous procedure

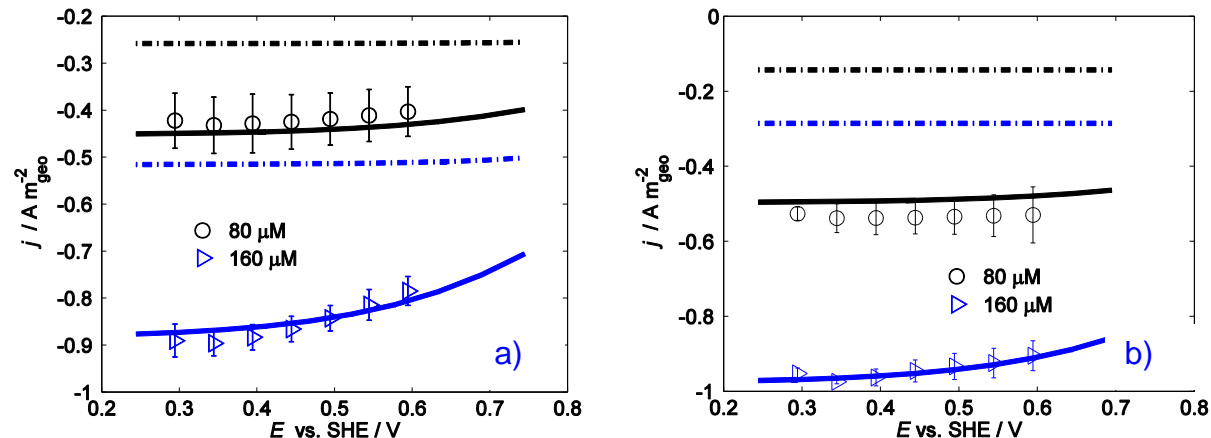


Figure 5-15: Steady state polarization curves of PVDF electrodes: symbols – experimental data, dashed lines – simulated curves of reduced 1-D model; continuous lines – simulated curves of full 1-D model. a) thin porous electrode b) thick porous electrode. Conditions: fixed delay of 1 minute,  $H_2O_2$  concentrations of 80  $\mu M$  and 160  $\mu M$ , room temperature; rotation rate 400 rpm, with other parameters given in Table 5-10 and Table 5-9

Figure 5-15 shows the steady state behaviour of the thin (20  $\mu L$  ink loading) and the thick (70  $\mu L$  ink loading) PVDF electrodes at two  $H_2O_2$  concentrations. In general, simulation can describe well the experimental data for the two studied systems. The three fitting parameter values ('a',  $\epsilon$  and substrate diffusivity) are given in Table 5-10. The CL void fraction based on the simulations is 0.35, which shows the high packed electrode and is slightly smaller than the calculated value of 0.45 for the same type of electrode, as shown in [132]. The reason for this difference is the neglect of the enzyme phase in the theoretical calculation. The internal electrochemical surface area is  $5.04 \times 10^5 m_{act}^2 m_{geo}^{-3}$  and relatively small (c.a 4.6%) in comparison to the theoretical calculated value based on the BET of Vulcan. The low utilization of available active surface area can be explained by either the contribution of the binder PVDF, or the low utilization of enzymes inside the CL. In the presence of PVDF, the actual active surface area can be smaller than the theoretical value due to the possible covering and blocking of the conductive particles. The total active surface area of the thick electrode is 1.6 times higher than that of the thin electrode, which does not correspond to the independent correlation of the internal active surface area to the thickness at a constant porosity. The result

suggests that either constant porosity or the constant enzyme coverage per active surface area for the thin and thick electrodes was not completely fulfilled.

A total number of enzymes calculated based on Eq. (245) for the thin and thick electrodes are  $8 \times 10^{-13}$  mol and  $35.5 \times 10^{-13}$  mol respectively. They are higher than the values of the thin electrode (ca. 4 times). In comparison to the nominal loading, these values also show that only a small amount of enzyme can be used effectively in the porous electrode. The higher number of utilized enzymes in the porous electrode in comparison to the thin film electrode (ca. 10 times more for the thin electrode and 40 times for the thick electrode) enhances the current density of the porous electrode (by ca. 3 times for the thin electrode and 4 times for the thick electrode). However, the proportional relation between the amount of active enzyme and current density could not be obtained due to the mass transport limitations, especially at higher ink loading.

**Table 5-10: Estimated parameter values for the porous HRP modified Vulcan- PVDF electrodes under different conditions of ink loading and  $H_2O_2$  concentrations**

Parameter	25 $\mu$ L	70 $\mu$ L	70 $\mu$ L ( $C_{H_2O_2}=1000 \mu$ M)	70 $\mu$ L ( $C_{H_2O_2}=3000 \mu$ M)
$\epsilon$	0.35	0.35 <sup>**</sup>	0.35 <sup>**</sup>	0.35 <sup>**</sup>
$D_{S1}/10^{-9} m^2 s^{-1}$	1.6	1.6	1.6	1.6
$L/10^{-6} m_{geo}$	19 <sup>++</sup>	53	53	53
$\Gamma_{E1t}/10^{-9} mol m_{act}^{-2}$	3 <sup>**</sup>	3 <sup>**</sup>	2.1	1.5
$a/10^5 m_{act}^2 m_{geo}^{-3}$	5.04	7.97	7.97 <sup>**</sup>	7.97 <sup>**</sup>
$n_{E1t}/10^{-13} mol$	8 <sup>++</sup>	35.5 <sup>++</sup>	24.85 <sup>++</sup>	17.75 <sup>++</sup>

<sup>\*\*</sup> adopted values from previous simulation, <sup>++</sup> calculated values

Figure 5-16 shows the spatial distribution of  $H_2O_2$  along the CL-DL of the thin and thick electrodes. At the steady state condition, concentration starts decreasing linearly from the DL and further decreases in the CL. These profiles are almost independent of the applied potentials. This behaviour shows the substantial governing of the mass transport inside the studied systems. The thin electrode works through, but only part of the thick electrode works



effectively. For example, the effective thickness of the thick electrode is around 27  $\mu\text{m}$ , compared to the nominal of 53  $\mu\text{m}$  of the thick electrode contributing to current production. The electrode is working under a mass transport controlling regime.

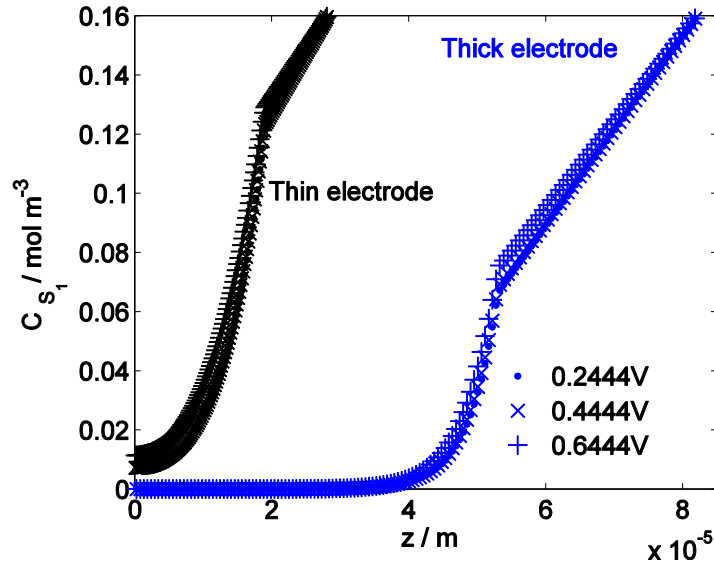


Figure 5-16: a) Steady state profile of H<sub>2</sub>O<sub>2</sub> concentration for the thin and thick electrodes at different applied potentials. Conditions: PVDF electrode, fixed delay of 1 minute, H<sub>2</sub>O<sub>2</sub> concentrations at 160  $\mu\text{M}$ , room temperature; rotation rate 400 rpm, pH5, with other parameters given in Table 5-9 and Table 5-10

Figure 5-15 also shows the simulation of the reduced distributed model in dashed lines. All the optimized parameters obtained from the full 1-D model are applied to the reduced model. The shortcoming of using the reduced model is the loss of information of the substance concentration distribution in the DL. However, the structural information of the CL, i.e. void fraction, electrode thickness, and active surface area, remains. As can be seen in Figure 5-15, the reduced model provided a smaller value to the experimental data and also failed to fit the experimental data at reasonable set parameters. The divergence between the 1-D and the reduced model in the thick electrode is even higher compared to the case of the thin electrode (Figure 5-15b). This confirms the necessity of the full 1-D model to describe the electrode performance and understand of processes taking place in the porous enzymatic electrode. The underestimation of the reduced model can be ascribed to the lower concentration in the CL (10-15  $\mu\text{M}$ ), calculated by the reduced model in comparison to the average.

Apparently, an increase in the electrode thickness is not always a good strategy to enhance the performance of the PVDF electrode due to the association with mass transfer resistance, which can create a 'non effective working portion' in the thicker electrode. Compared to the thick electrode, the thin electrode works more effectively. The reduced model is not able to depict the porous system behaviour well. This again proved the importance of the distributed model in describing the porous CL. In the following sections, only the distributed model is used to describe the enzymatic porous electrode.

### **5.3.2.2 Gelatin porous procedure**

The distributed model incorporated kinetic parameters from the interface model and was able to describe the DET porous PVDF electrode. The distributed model was utilized further to study the behaviour of the DET Gelatin porous electrode using HRP. The kinetic parameters were adopted from the thin film system. The additional fitting parameters were void fraction, internal active surface area, and substrate diffusion coefficient  $D_{S1}$  in the Gelatin environment. The optimized parameters were obtained using the same procedure described in section 5-1. Similarly, the porosity, diffusion coefficient and the internal active surface area were determined from the thinner electrode with lower ink loading. The former two parameters were then input into the thicker electrode model with additional optimization of the active surface area.

The experimental data, along with the simulated data of the 1-D model under steady state conditions for the two different electrode thicknesses, are illustrated in Figure 5-17. The qualitative agreement between the experimental data and the simulated data can be seen in both cases. However, slight deviation between the experimental and simulated data can be seen in the case of the thin electrode, at lower and higher ranges of applied potentials. This phenomenon is more pronounced in the case of the Gelatin than in that of the PVDF, showing the possibility of high dispersion of enzyme orientation. At the lower range of applied potential (<0.4 V), the simulation underestimates the experimental data, presenting a higher number of active enzymes performing the electrochemical reaction. This behaviour is opposite at the higher applied potential value (>0.4 V). The favoured orientation effect of enzymes can cause a high distribution of reaction kinetic constants related to enzyme coverage, which was neglected

in the modelling. It should be remembered that all the kinetic constants were adopted from the interface model and can be considered as effective rate constants for given enzyme orientations at the flat electrode surface. The results of the thin porous electrodes also imply that the dispersion of enzyme orientations is significant in the case of the flat electrode. Additionally, the possibly formation of enzyme agglomerates and enzyme clogging due to the cross-linking of Gelatin can cause the rate constant distribution.

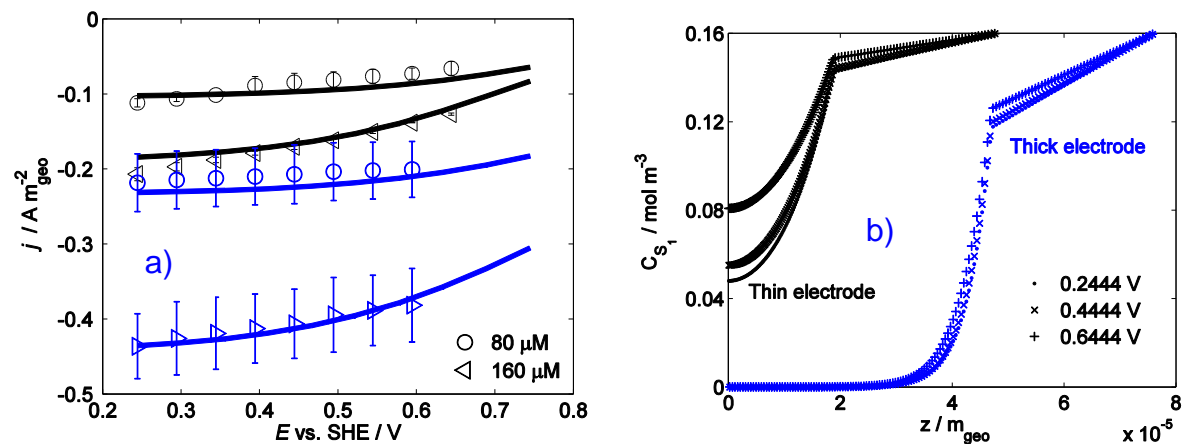


Figure 5-17: a) Steady state polarization curves of the thin and thick Gelatin electrodes: symbols – experimental data, continuous lines – simulated curves of 1-D model; b) simulated local profiles of  $\text{H}_2\text{O}_2$  concentration for a thin (in black) and a thick (in blue) porous electrode along the spatial coordinate. Conditions: fixed delay of 1 minute,  $\text{H}_2\text{O}_2$  concentrations of 80 and 160  $\mu\text{M}$ , room temperature; rotation rate 400 rpm, pH5, with other parameters given in Table 5-9 and Table 5-11

Similar to the PVDF system, the increase in electrode thickness results in better electrode performance due to the higher number of active enzymes for the electrochemical reaction. The number of active enzymes was calculated and is shown in Table 5-11. As can be seen, enzyme utilization is very low (in the range of  $10^{-3}$  to  $10^{-2}$  %) which can be explained by the effect of enzyme agglomeration. The agglomeration formation of enzymes lessens the electrode activity by cross-linking and by GA, and has been demonstrated in the literature [9, 132, 147]. The much smaller amount of enzyme utilization in the thin film electrode (almost 10 times lower than for the thick electrode) demonstrates that the cross-link agent may penetrate deep inside the thin electrode and decrease significantly the amount of active enzyme. It can be observed that the cross-linking procedure is the determining step contributing to such behaviour.

Experimentally, the Gelatin electrode after preparation was dipped in the GA solution for a certain time, allowing a more thorough cross-linking thin electrode and possibly creating a non-cross-linked part of the thick electrode. To see this influence, the cross link time of the thick porous electrode should be included. This cross-linked effect is also reflected in the non-linear increase in the total number of active enzymes between the thick and the thin electrodes (ca. 17 times for enzyme increase vs ca. 2.5 times increase in the electrode surface).

The determined value of porosity in the present system is 0.3, indicating even denser packing of the Gelatin procedure than in the PVDF case. This behaviour corresponds well with the SEM pictures of the electrode cross section and the top views reported in [132]. The diffusion coefficient of the  $H_2O_2$  in the Gelatin environment is  $5 \times 10^{-10} \text{ m}^2 \text{ s}^{-1}$ , which is significantly smaller than its value in the bulk and is close to the reported value for  $H_2O_2$  diffusion in hydrogels [148].

**Table 5-11: Estimated parameter values for porous HRP modified Vulcan- Gelatin electrodes under different conditions of ink loading and  $H_2O_2$  concentrations**

Parameter	20 $\mu\text{L}$	50 $\mu\text{L}$	50 $\mu\text{L}$ ( $C_{H_2O_2}=1000 \mu\text{M}$ )	50 $\mu\text{L}$ ( $C_{H_2O_2}=3000 \mu\text{M}$ )
$\epsilon$	0.3 <sup>**</sup>	0.3 <sup>**</sup>	0.3 <sup>**</sup>	0.3 <sup>**</sup>
$D_{S1}/10^{-9} \text{ m}^2 \text{ s}^{-1}$	0.5	0.5 <sup>**</sup>	0.5 <sup>**</sup>	0.5 <sup>**</sup>
$L/10^{-6} \text{ m}$	19 <sup>++</sup>	47 <sup>**</sup>	47 <sup>**</sup>	47 <sup>**</sup>
$\Gamma_{E1t}/10^{-9} \text{ mol m}_{\text{act}}^{-2}$	3 <sup>**</sup>	3 <sup>**</sup>	2.1	1.2
$a/10^5 \text{ m}_{\text{act}}^2 \text{ m}_{\text{geo}}^{-3}$	0.35	2.35	2.35 <sup>**</sup>	2.35 <sup>**</sup>
$n_{E1t}/10^{-13} \text{ mol}$	0.56 <sup>++</sup>	9.2 <sup>++</sup>	6.44 <sup>++</sup>	3.68 <sup>++</sup>

<sup>\*\*</sup> adopted values from previous simulation, <sup>++</sup> calculated values

Figure 5-17b shows the steady state concentration profile of the substrate along the spatial coordinate for the thin and the thick electrodes. Similar to the PVDF system, mass transfer limitations can be observed in all the studied cases and are more severe in the case of the thick electrode. The calculated effective electrode thickness and amount of active enzyme of the thick electrode are  $24 \mu\text{m}$  and  $4.5 \times 10^{-13} \text{ mol}$  respectively. The concentration profile of  $H_2O_2$  in the case of the thick electrode drops rapidly to zero due to the higher amount of

enzyme active in the CL. The minor potential dependence on steady concentration profile can be seen in both cases. The ion and electron transports are not limited processes for this system.

### 5.3.2.3 Higher range of concentration

Figure 5-18a shows the steady state responses of the thick electrode at higher  $\text{H}_2\text{O}_2$  concentrations (1000  $\mu\text{M}$  – 3000  $\mu\text{M}$ ) in the two procedures. The simulation shows a quantitative and qualitative fit with the experimental data. At this condition, all the parameters are kept the same as in the case of low substrate concentrations (10  $\mu\text{M}$  – 160  $\mu\text{M}$ ). The remaining fitting parameter is enzyme coverage, reflecting the influence of inhibition on the system. The possibility of side-reactions taking place in the catalytic cycle of HRP at higher substrate concentrations which can catalytically form non-active enzyme forms has been demonstrated [129]. These inhibition reactions were not expressed explicitly in the kinetic models. Alternatively, approximation of this effect can be made by changing the enzyme coverage per active surface area (Table 5-10 and Table 5-11), which influences further the total number of active enzymes. This parameter is optimized and shown in Table 5-10 and Table 5-11. The data in these tables show a decrease in the enzyme coverage with increasing  $\text{H}_2\text{O}_2$  concentration. As a consequence, the calculated total number of active enzymes declined with an increase in  $\text{H}_2\text{O}_2$  concentration in both studied systems. For example, for the PVDF electrode, there is a ca. 70% decrease in the total number of active enzymes at 1000  $\mu\text{M}$  compared to its value in low substrate concentrations, and ca. 25 % and 40 % reductions at 1000  $\mu\text{M}$  and 3000  $\mu\text{M}$  respectively in the case of Gelatin.

The maximum current density can reach ca.  $10 \text{ Am}^{-2}$  for the PVDF optimized electrode (Figure 5-18a) and  $3 \text{ Am}^{-2}$  for the Gelatin optimized electrode. The PVDF system still provides better performance due to the higher amount of the active enzyme. The performance of these optimized electrodes is very high compared to other reported enzymatic cathodes. For example, the comparable result of MET laccase enzyme on the “wired” cathode has been reported at pH5, 37 °C [149] and the reported values of all other HRP/nanotube based electrodes at pH6 is lower than our studied electrode [150, 151].

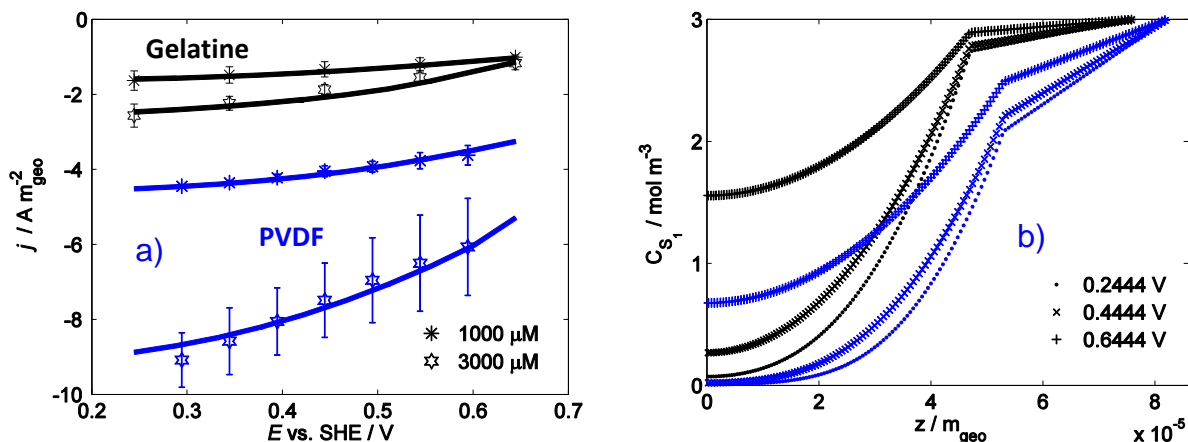


Figure 5-18: a) Steady state polarization curves at high concentration for the thick electrode: symbols – experimental data, continuous lines – simulated curves of 1-D model; b) simulated local profiles of  $\text{H}_2\text{O}_2$  concentration for the Gelatin (in black) and PVDF (in blue) electrode along the spatial coordinate. Conditions: fixed delay of 1 minute,  $\text{H}_2\text{O}_2$  concentrations of  $1000 \mu\text{M}$  and  $3000 \mu\text{M}$ , room temperature, rotation rate 400 rpm, pH5, with other parameters given in Table 5-9 and Table 5-11

The higher the substrate concentration, the better electrode performance can be obtained. This is due to the effective utilization of CL, which can be seen in the concentration profile of  $\text{H}_2\text{O}_2$  in Figure 5-18b. These profiles reveal that both electrodes work through. A potential dependence of profile now can be seen. However, the mass transport is still an obstacle for the system performance.

Two different electrode preparation procedures, namely PVDF and Gelatin, were used for two main reasons. The first was to demonstrate the necessity of the model in describing porous electrode behaviour. The second was to study the impact of the preparation procedure on system performance. In both cases, the PVDF electrodes performed electrochemically better than the Gelatin electrodes, which show the high impact of the cross-linking step in porosity and enzyme agglomeration. The two systems are under mass control, which is revealed from the concentration profiles of the  $\text{H}_2\text{O}_2$  along the spatial coordinate.

The structural parameters, including the void fraction and the internal active surface area, are the fitted parameters in the two procedures. The calculated enzyme utilization is small, reflecting the importance of enzyme orientation for electrochemical performance in the case of DET. The results show a strong correlation between the kinetic and some structural parameters

of the studied systems. The good fit of the simulation with the experiment also demonstrates the right approach for the kinetic parameter determination, using an independent method, i.e., the thin film electrode approach.

### **Implications:**

The 1-D porous model was utilized further in the DET system and experimentally validated. The structural parameters, such as the void fraction and the internal active surface area, were determined for the two different electrode preparation procedures (PVDF and Gelatin). In the case of DET, the PVDF procedure can provide a more open structure, which is beneficial for easy  $H_2O_2$  diffusion inside the porous matrix. This results in a higher performance of the PVDF electrode in comparison to the Gelatin one. In addition, Gelatin provided less current density in the whole range of applied potentials. These behaviours cannot be observed in the case of MET.

A 'dead' portion of the electrode still appears due to the mass transfer limitation of the  $H_2O_2$ , which can be reviewed from the concentration profiles along the spatial coordinate. At a higher concentration of  $H_2O_2$ , this limitation is moderate, but the enzyme inhibition effect by the substrate might become significant

Enzyme utilization in both the Gelatin and PVDF systems is low, although the PVDF procedure allows more enzymes to remain active for the electrochemical reaction in comparison to the Gelatin procedure. Apparently, this is not the case of porous MET, probably due to the different reaction steps related to the enzymes. Specifically, enzymes participate in both enzymatic and electrochemical steps in the case of DET, while only in the enzymatic and mediator regeneration steps in the case of MET.

### 5.3.3 Porous electrode with the enzymatic cascade GOx-HRP

The 1-D model was demonstrated to be a relevant approach to exploring the porous enzymatic behaviour using DET and MET enzymes. The model is now extended to study the behaviour of the GOx-HRP cascade in a porous structure. The mathematical model was performed representatively with a temperature at 25°C at pH6. The relevant kinetic parameters are extracted from previous sections and presented in Table 5-12.

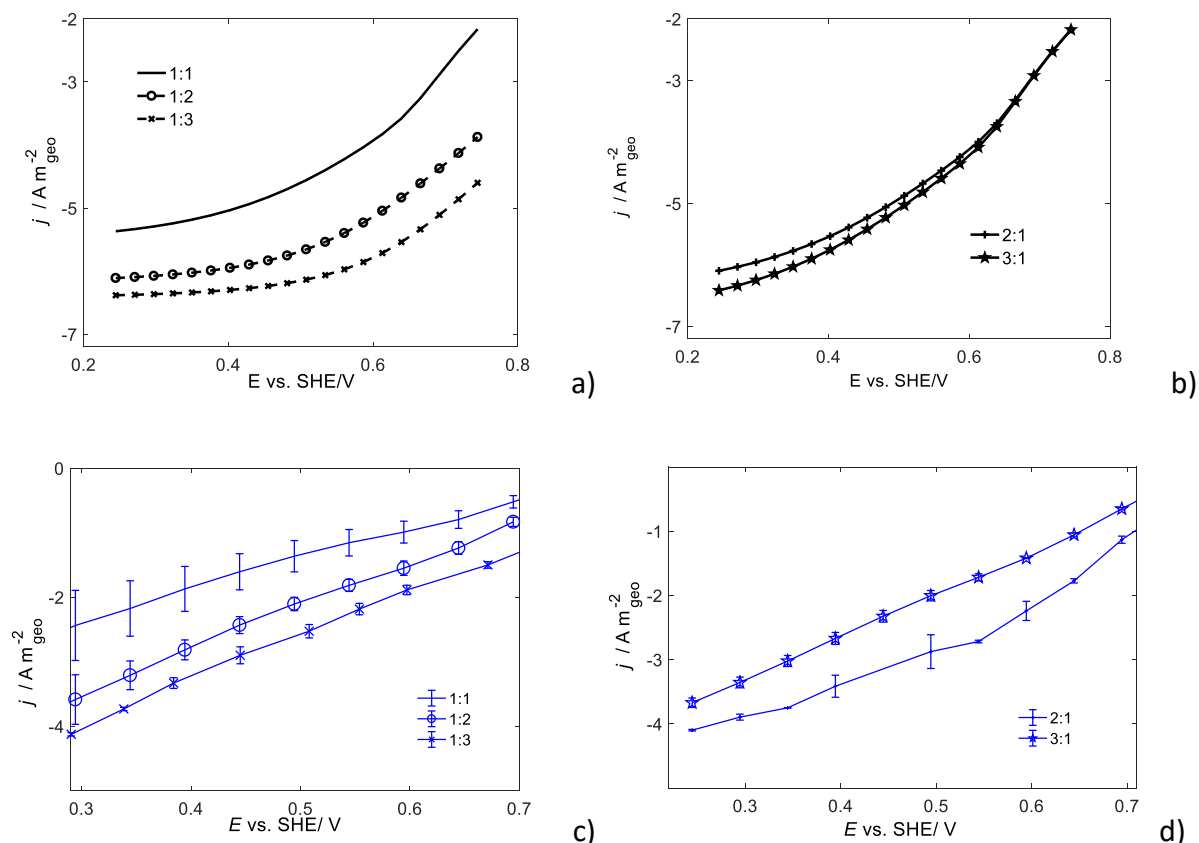


**Figure 5-19: Simulated steady state polarization curves by increasing HRP at a fixed concentration of GOx: a) simulation c) experiment and increase in GOx at a fixed concentration of HRP: b) simulation d) experiment. Conditions: 20 mM of glucose concentration, porous electrode, fixed delay of 2 minutes, pH6, 25 °C; rotation rate 400 rpm; parameters for the simulations are given in Table 5-9 and Table 5-12**



**Table 5-12: Model parameters for simulation of the porous GOx-HRP modified Vulcan PVDF electrodes**

Parameter	Value	Parameter	Value
$\epsilon$	0.35 **	$k_1 / \text{m}^3 \text{mol}^{-1} \text{s}^{-1}$	$15.9 \times 10^3$ **
$K_{11} / \text{m}^3 \text{mol}^{-1} \text{s}^{-1}$	4 **	$k_{-1} / \text{s}^{-1}$	1962 **
$K_{22} / \text{m}^3 \text{mol}^{-1} \text{s}^{-1}$	1562 **	$k_{\text{cat}} / \text{s}^{-1}$	1202 **
$K_{33} / \text{m}^3 \text{mol}^{-1} \text{s}^{-1}$	252 **	$k_{e10} / \text{m}^3 \text{mol}^{-1} \text{s}^{-1}$	$2.63 \times 10^5$ **
$L / 10^{-6} \text{m}_{\text{geo}}$	53 **	$k_{e20} / \text{m}^3 \text{mol}^{-1} \text{s}^{-1}$	$36.7 \times 10^3$ **
$\Gamma_{E1t} / 10^{-9} \text{mol m}_{\text{act}}^{-2}$	2.2 **		

\*\* adopted values from previous simulation

Figure 5-19 displays the simulation and experimental steady state polarization curves of the porous electrodes using GOx-HRP at different ratios. As the nominal enzyme loading changes, the amount of active enzyme is assumed to be proportional to the trend. For example, the GOx concentration at the 1:1 ratio is  $0.04 \text{ mol} \cdot \text{m}^{-3}$ , which is doubled, tripled at the ratios of 2:1 and 3:1, respectively. As can be seen, the increase in HRP creates two phenomena, including promotion of the system performance and a shift in the onset potential in both the experiment and simulation [129]. The increasing amount of GOx in the system can accelerate the glucose consumption rate, which thus speeds up the  $\text{O}_2$  reduction to produce the intermediate  $\text{H}_2\text{O}_2$  for the electrochemical reaction. Consequently, the electrode performance is improved. However, the performance is still lower than the ratios 1:2 and 1:3 at 20 mM of glucose concentration due to its lower HRP concentration. In addition, at a fixed HRP concentration, increasing GOx concentration does not vary the onset potential and only slightly improves the performance at the higher over-potential range (Figure 5-19 b). This indicates that the amount of HRP is more significant for the system performance. Experimentally, the shift of the onset potential was observed not only by HRP loading but also by the GOx loading. Moreover, the change in electrode performance did not correspond to the simulation behaviour (Figure 5-19 c,d). This can be explained by the reduction in the electrochemical active surface area due to the occupation of GOx and the non-ideality of the real system.

The simulated data (ca.  $6.2 \text{ A m}_{\text{geo}}^{-2}$ ) is higher than the experimental data (Figure 5-20) (ca.  $3.9 \text{ A m}_{\text{geo}}^{-2}$ ) and only qualitative agreement between both sets of data could be obtained.

Experimentally, among these electrodes the data at the ratio of 2:1 provided the highest performance, while the ratio of 1:3 provided better performance in the simulation. Practically, increasing further the GOx decreases electrode performance due to the possibility of electroactive surface area being occupied by GOx.

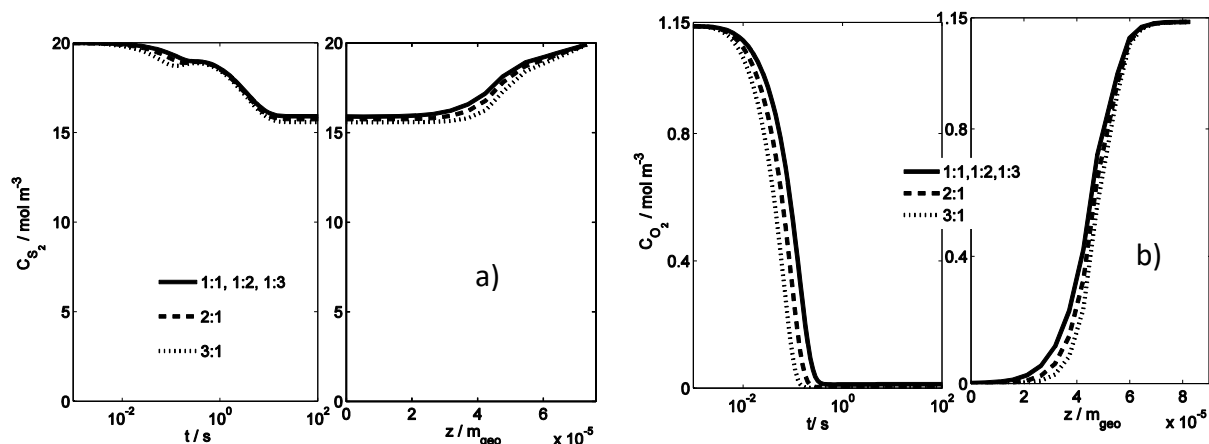


**Figure 5-20: Simulated transient (at fixed position in the middle of CL) and steady state (along the spatial coordinate) profiles of a) glucose ( $S_2$ ) concentration b)  $O_2$  at 20 mM of glucose concentration. Conditions: temperature 25°C, pH6, rotation rate 400 rpm, with other parameters given in Table 5-9 and Table 5-12**

From Figure 5-20, the simulated concentration distributions of  $S_2$  ( $C_6H_{12}O_6$ ) and  $O_2$  show an independent relationship to the applied potentials. Instead, it is slightly dependent on the enzyme ratios. This behaviour can be ascribed to the interplay between the reduction of  $O_2$  and  $H_2O_2$  on the whole potential range. Increasing the amount of HRP did not influence the  $S_2$  and  $O_2$  concentration profiles due to the limitation of  $O_2$  inside the CL and the control of the electrochemical rate. A higher amount of GOx makes a slightly steeper concentration profile due to more GOx being available for the glucose reduction. Due to the slow electrochemical step,  $H_2O_2$  is always available for enzymatic and electrochemical reactions with HRP, as seen in Figure 5-21a. The transient state is very short, which agrees well with literature findings and also indicates that the porous structure composite immobilized GOx and HRP made  $S_2$  and  $H_2O_2$  easily locally accessible to the active sites of those enzymes.

The dynamic and spatial concentration profiles of  $H_2O_2$  at various potentials (Figure 5-21) reveal a proportional relation to the applied potential. At lower applied potentials, the electrochemical regeneration of HRP is faster due to the higher driving force and vice versa. As

a consequence, less  $\text{H}_2\text{O}_2$  remains in the CL at the lower range of applied potentials than at higher applied potentials. The concentration of  $\text{H}_2\text{O}_2$  reaches its maximum level in the middle of the CL, indicating the crossing of the  $\text{O}_2$  under supply from the left part of the CL and the high  $\text{H}_2\text{O}_2$  consumption rate in the right part (Figure 5-21a)

The spatial and transient concentration distributions of  $\text{H}_2\text{O}_2$  at different loadings of enzymatic cascade are presented in Figure 5-21b. A similar trend to the 1:1 ratio can be seen in the dynamic and steady state profiles. First, the increased amount of HRP decreases the  $S_1$  ( $\text{H}_2\text{O}_2$ ) concentration in the CL due to the higher consumption rate. At higher loadings of GOx (ratios of 2:1 and 3:1), the production of  $\text{H}_2\text{O}_2$  is increased in the layer close to the DL since the amount of active GOx has increased.

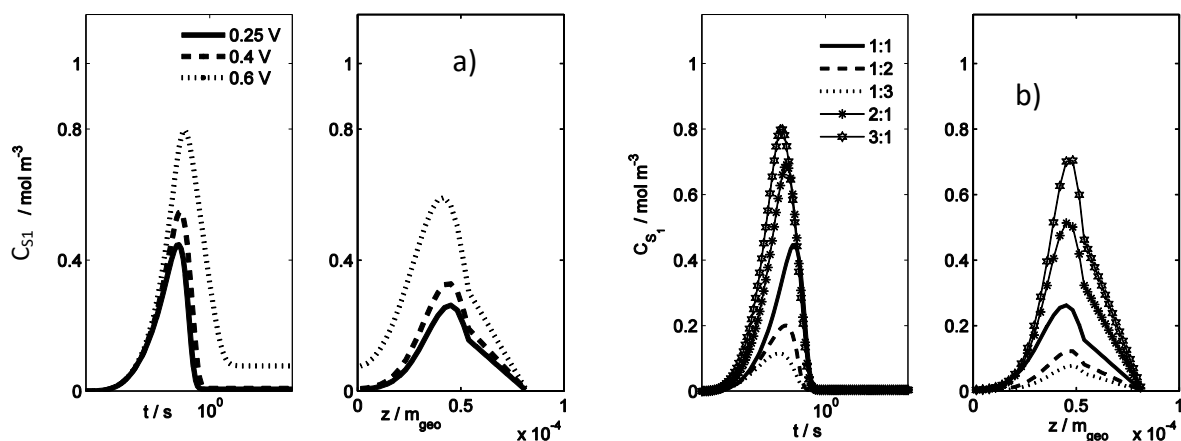


Figure 5-21: Simulated transient (at fixed position in the middle of CL) and steady state (along spatial coordinate) profiles of  $\text{H}_2\text{O}_2$  concentration at a) different applied potentials at enzyme ratio 1:1 b) different ratios. Conditions: 20 mM of  $S_2$ , 25°C, pH6, rotation rate 400 rpm, with other parameters given Table 5-9 and Table 5-12

Due to the observation of the mass transport resistance of  $\text{O}_2$  in the porous CL, additional simulation was performed for different  $\text{O}_2$  supply regimes, as shown in Figure 3-7 (section 3.4.3). The steady state behaviour of these systems is presented in Figure 5-22. The electrode with an  $\text{O}_2$  supply from both sides ( $S_{c3}$ ) achieved the highest absolute current density while the lowest performance was obtained for the configuration  $S_{c2}$ . At 20 mM of glucose

concentration, there is an intersection of performance for Sc1 and Sc2 due to the controlling of the  $O_2$  transport inside the CL.

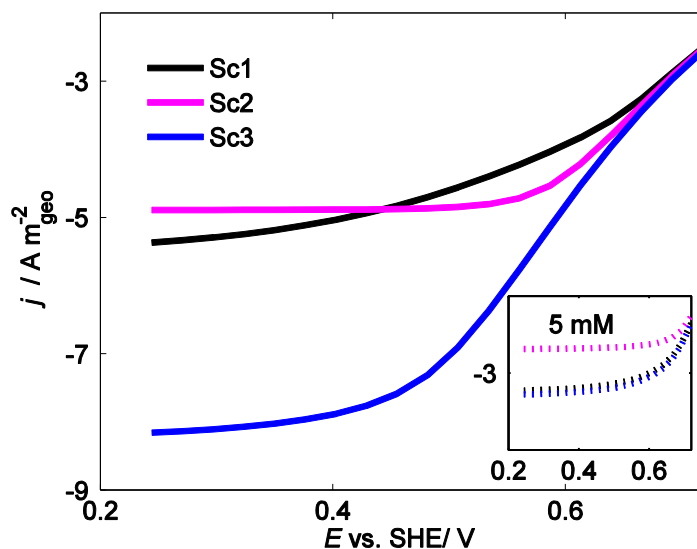


Figure 5-22: Simulated steady state performance of the enzymatic DET electrode with different scenarios of  $O_2$  supply, rotation rate 400 rpm, and with other parameters given in Table 5-9 and Table 5-12

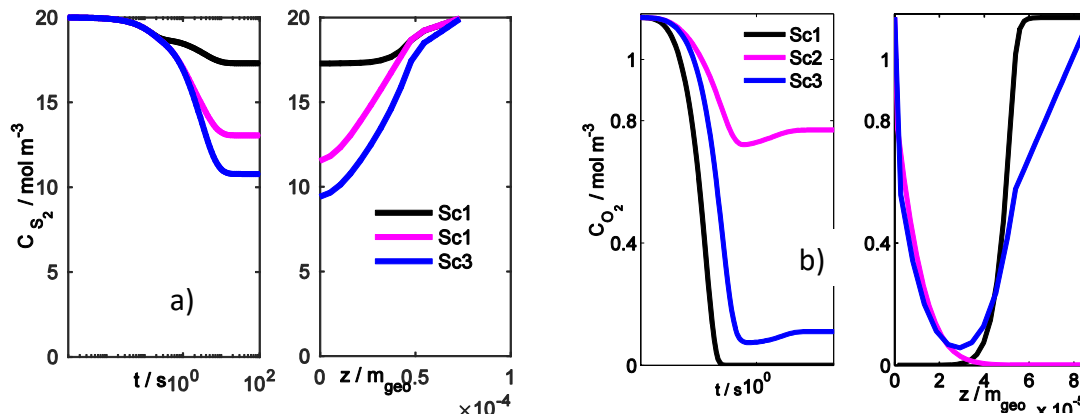


Figure 5-23: Simulated transient (at fixed position in the middle of CL) and steady state (along the spatial coordinate) profiles of a) glucose concentrations and b)  $O_2$  at different  $O_2$  supply scenarios. Conditions: 0.25 V, pH6, 25°C, rotation rate 400 rpm, with other parameters given in Table 5-9 and Table 5-12

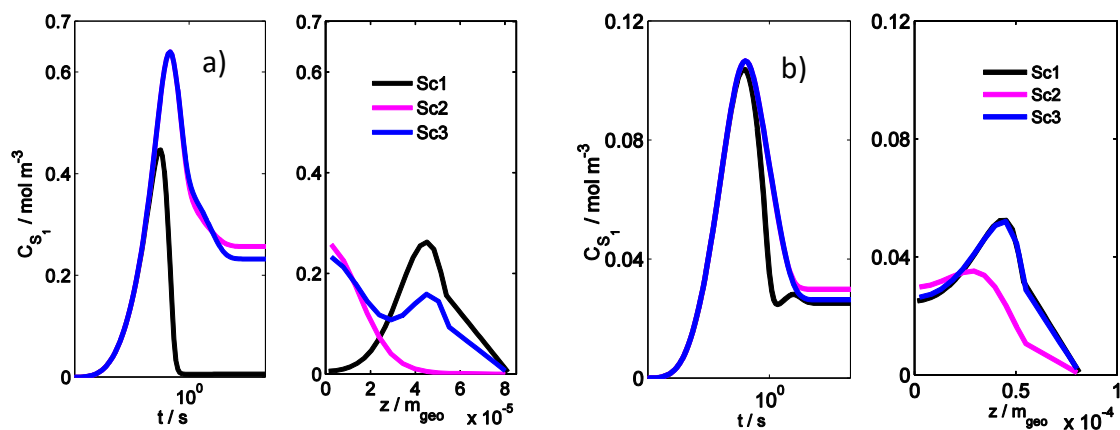


Figure 5-24: Simulated transient (middle of CL) and steady state (along spatial coordinate) profiles of  $S_1$  concentrations a) at 5 mM and b) 20 mM of glucose concentration. Conditions: 0.25 V, pH6, 25°C, rotation rate 400 rpm, with other parameters given in Table 5-9 and Table 5-12

Figure 5-23 shows the spatial and dynamic concentration distribution of glucose for different configurations of  $O_2$  supply (Sc1-Sc3) at the applied potential of 0.25V. Glucose consumption increases from Sc1 to Sc3 due to the availability of  $O_2$  participating in the enzymatic reaction system. The completed utilization of the CL of  $O_2$  can be seen for the Sc3, while the mass transport still appears in Sc2 close to the DL. The spatial concentration profile of  $O_2$  in the case of Sc3 is the combination of the profiles of Sc1-Sc2. The whole layer is now working through.

The spatial and transient concentration distributions of  $H_2O_2$  at different  $O_2$  supplied scenarios of the enzymatic cascade system at 5mM and 20mM of glucose concentration are presented in Figure 5-24. At 5mM of glucose concentration, the  $H_2O_2$  concentration is highest at the left end of the CL due to more  $O_2$  supplied from that side. One can see the deficiency of  $O_2$  in the right boundary in the Sc2. At 20mM of concentration, more  $FADH_2$  is available to uptake  $O_2$ , therefore, no mass limitation of  $H_2O_2$  can be observed.

# 6 Concluding remarks and outlook

*“The scientist is not a person who gives the right answers, he's one who asks the right questions”*

---

*– Rainer Maria Rilke*

## 6.1 Conclusions

A systematic modelling approach has been developed to study the behaviour of electrochemical enzymatic systems. As the model systems, GOx and HRP have been selected as representative MET and DET biocatalysts, respectively. They are commonly used in biosensors, fuel cells as well as biotransformation processes i.e conversion of glucose to other chemicals. The focus was on model discrimination, parameter determination and process analysis. For each porous enzymatic electrode, different preparation procedures, namely Gelatin and PVDF, were used to validate the mathematical model. Different mathematical macroscale models, i.e., the distributed model, EIS and interface model, were used to describe the studied system.

The distributed model including the relevant kinetics was first used on the anode side for the model selection, parameter determination and process analysis. In the case of MET, GOx and mediator TTF were immobilized in the porous matrix using Vulcan as the conductive material and stabilizers (PVDF, Gelatin). Two electrode preparation procedures named in accordance with the respective stabilizers (PVDF and Gelatin) were employed to validate the mathematical distributed model. The distributed model was able to describe excellently the experimental data in both procedures at pH7, 37°C and pH6, 25°C. In the same system, the electrode system performance was lower at pH6, 25°C due to the slower reaction kinetics. The simulation emphasised the importance of the oxidized mediator diffusing out of the CL especially at the higher applied potential. At the working condition of pH7, temperature at 37°C, both procedures could provide an electrode with similar performance at higher applied potentials. The thin electrode of the Gelatin system behaved similarly to the PVDF electrode. The Gelatin procedure provided better activity than the PVDF one at lower applied potentials due to the higher amount of mediator available for the electrochemical step. Moreover, in

comparison to the thick Gelatin electrode, activity of thin Gelatin electrode provided similar performance at the higher range of applied potentials and lower performance at lower applied potentials. This can be explained by the mass transport limitation of the thick electrode which is observable in the concentration profiles. Provided a specific set of reaction constants, the shift in the onset potential on the Gelatin electrodes can be ascribed mainly to the related constants in the electrochemical steps, i.e., mediator and related mediator kinetics constants in the MET. The mathematical simulation suggested the dependence of catalytic activity on pH and temperature, and the lower utilization of catalysts and mediators in the systems. In addition, the different electrode preparations contributed significantly to the system performance. The presence of  $O_2$  in the system decreased the electrode activity in general. This decline is more significant at lower concentrations of glucose due to the control of the enzymatic reaction steps. The inhibition effect of  $O_2$  on the enzyme activity is negligible at the studied conditions. Better electrode design to improve the mass transport of species into the CL (e.g. selection of binders, size of nanomaterials, type of material to increase the enzyme affinity...) and the selection of suitable mediators are the important keys to accelerate the system performance toward a system usable for practical applications.

On the cathode side, the reaction kinetics and parameter identification were first performed in the thin film electrode. The analytical derivations for the steady state and EIS models were obtained for the three proposed mechanistic models. At the steady state conditions, pH5 and pH6, 25°C, qualitative and quantitative fitting to the polarization curves were obtained for the three proposed models. The simulation showed that the EIS methodology is more sensitive for parameter estimation and model discrimination. The best kinetic model considering the enzyme substrate complex step and  $H_2O_2$ ,  $H^+$  diffusion was selected, further parameterized and inserted into the distributed model. The porous model incorporating the kinetics which was obtained from the surface electrode model was able to describe the experimental data using the PVDF and Gelatin procedures at pH5, 25°C. The additional fitting parameters are related to structural parameters and diffusivities of substances in the Gelatin environment. The simulation demonstrated that the PVDF porous system could provide better activity than the Gelatin porous electrode due to the higher number of active

enzymes remaining on the conductive surface and better CL utilization. This behaviour spreads to the whole range of applied potentials but cannot be observed in the case of the MET enzyme, which indicates that immobilization strategies causing enzyme agglomeration are disadvantageous for enzymes obeying the DET mechanism. The concentration profiles indicated that the mass transport limitation of  $H_2O_2$  is more pronounced in the electrode using the Gelatin procedure. However, the catalyst utilization of both systems is low and is the key factor in increasing electrode performance in the case of DET.

The distributed model was also used to study the behaviour of the porous electrode using the enzymatic cascade of GOx-HRP at pH6, 25°C. The kinetic parameters obtained by optimization of the individual GOx and HRP electrode were inheritably used. It has been shown that the model was able to depict qualitatively the experimental data at different GOx-HRP ratios. It means that the straightforward relationship between enzyme ratios and the electrode performance cannot be easily seen due to the additional process interactions and the contributions of non-idealities of the experimental system. The concentration profiles of glucose and  $O_2$  along the CL are more dependent on the enzyme ratio. The mass transfer of  $O_2$  and electrochemical steps are the rate limiting steps of the porous electro-enzymatic cascade system. Different supply scenarios of  $O_2$  to the CL have been proposed. The enzymatic electrode performance in the case of the  $O_2$  supply from both sides of CL provided highest activity which corresponds also to the experimental observation.



## 6.2 Outlook

The distributed model has proven its necessity in describing the behaviour of the enzymatic porous electrode. This approach should be applied to other systems using, for instance, different enzymes, and enzymatic cascades. Alternatively, it can be used further in a system with an ordered porous electrode structure/ different material.

The EIS methodology demonstrated a high sensitivity for parameter estimation and model discrimination. It showed potential for studying and understanding other bioelectrochemical processes. Therefore, it can be employed further in other enzymatic systems and porous electrodes.

The enzyme orientation/distributions through the CL and the number of active enzymes are critical for the kinetic parameter determination due to their high correlation with each other and other parameters, i.e., active surface area/ porosity. These factors should be correlated into the mathematical model system, which could provide more insight into the system behaviour.

It is also essential to consider the further use of kinetics and parameters from this work in a higher complex model system; for example, an electroenzymatic reactor for biotransformation or a fuel cell system for power generation.

**Table 6-1: Further possible extensions of the current work**

Approach	The bottom up approach to obtain parameters that can be subsequently used further in the respective system should be used in other electro-enzymatic systems.
Mathematical Model	Extension of the 1-D porous electrode model into different enzymatic systems and different porous structure preparations.
	The mathematical model should consider the CL partition due to possible different enzyme and mediator distribution inside the CL.
	Extension of EIS for model discrimination and process analysis in porous enzymatic electrodes and other electro-enzymatic systems. The higher frequency response function should be derived to further investigate the behaviour of the enzymatic system.
Parameter	The methodology for better estimation of the enzyme and mediator concentrations would help to obtain identifiable kinetic constants
	The enzyme distribution and electron tunnelling distance should be included in the model using DET enzymes.
The whole system	Use of optimized parameters for the mathematical modelling of an enzymatic reactor or an enzymatic fuel cell.

# List of figures

Figure 1-1: Different approaches in designing electro-enzymatic systems .....	2
Figure 1-2: Schematic representation of the process system engineering (PSE) modelling approach which includes the steps in finding answers to the research questions.....	7
Figure 1-3: Schematic representation of the different steps of modelling to obtain parameters subsequently used for the GOx-HRP cascade.....	8
Figure 2-1: Schematic representation of the “lock-and-key” mechanism for an enzyme substrate reaction (particularly for oxidoreductases) .....	9
Figure 2-2: Schematic representation of different electrode configurations: a) a monoenzyme layer, b) multi-enzyme layers entrapped behind a membrane and c) a porous enzymatic electrode.....	12
Figure 2-3: Schematic presentation and working principle of an enzymatic biofuel cell .....	13
Figure 2-4: Schematic representation of: a) SEM image of CL; b) typical modelling domains ....	16
Figure 2-5: Schematic representation of the physical modelling domain: a) an interface model b) a spatial distributed model c) a spatial distributed model with enzyme layer trapped behind a membrane.....	21
Figure 2-6 : Illustration of the discretization in the spatial domain .....	23
Figure 2-7: Schematic representation of the EIS methodology.....	26
Figure 3-1: Overview of the physical modelling domain corresponding to the respective experimental setup of the thin film and the porous electrode organized by length scale.....	33
Figure 3-2: Schematic representation of the reaction mechanism of the glucose oxidation using GOx - TTF in a porous conductive matrix.....	38
Figure 3-3: Schematic representation of the reaction mechanism of the glucose oxidation using GOx -TTF in a porous conductive matrix with additional oxygen supply .....	40
Figure 3-4: Schematic representation of electro-enzymatic reaction of HRP on a conductive surface in the presence of hydrogen peroxide (H <sub>2</sub> O <sub>2</sub> ).....	43
Figure 3-5: Schematic representation of the reaction kinetics of HRP in a conductive porous electrode in the presence of H <sub>2</sub> O <sub>2</sub> .....	48
Figure 3-6: Schematic representation of the reaction mechanism for the enzymatic cascade using GOx and HRP in the presence of glucose and O <sub>2</sub> in a porous conductive matrix .....	50
Figure 3-7: Schematic representation of O <sub>2</sub> supply into a porous CL.....	52
Figure 4-1: Schematic representation of electrode preparation procedure a) PVDF and b) Gelatin.....	54

Figure 5-1: Typical SEM image of a) PVDF porous electrode b) Gelatin porous electrode ..... 60

Figure 5-2: Steady state polarization curves of GOx modified Vulcan-TTF-PVDF electrodes: symbols – experimental data, full black lines – simulated curves of the model FM1, dashed blue lines – simulated curves of the model FM2, dashed black lines a) pH7, 37°C b) pH6, 25°C. Conditions: Ratio in mg of Vulcan-TTF-enzyme (20-10-6), fixed delay of 2 minutes, glucose concentrations 0, 5 mM and 20 mM, rotation rate 400 rpm, with other parameters given in Table 5-1 and Table 5-2..... 61

Figure 5-3: Simulated transient (at the middle of CL) and steady state (along spatial coordinate) profiles of glucose concentration a) at 5 mM and b) at 20 mM. Conditions: temperature 37°C, pH7, rotation rate 400 rpm, with other parameters given in Table 5-1 and Table 5-2 ..... 64

Figure 5-4: Simulated transient (at the middle of CL) and steady state (along spatial coordinate) profiles of glucose concentration a) at 5 mM and b) at 20 mM. Conditions: temperature 25°C pH6, rotation rate 400 rpm, with other parameters given in Table 5-1 and Table 5-2 ..... 65

Figure 5-5: Simulated steady state response of the full model showing the influence of the parameter variation with respect to their optimized values a)  $K_{11}$ , b)  $C_{Et}$ , c)  $K_{22}$ , d)  $D_{Mox}$ , e)  $C_{Mt}$ , f)  $k_{e0}$  and g)  $\epsilon$ . Conditions: 5 mM glucose concentration, pH7, temperature 37 °C, rotation rate 400 rpm, with other parameters given in Table 5-1 and Table 5-2..... 66

Figure 5-6: a) Steady state polarization curves of the Gelatin thin and thick porous electrodes: symbols – experimental data, lines – simulated curves electrode b) simulated local profiles of glucose concentration for a thin (in black) and a thick (in blue) porous electrode along spatial coordinate  $E=0.384$  V. Conditions: ratio in mg of Vulcan-TTF-enzyme (20-10-0.5), fixed delay of 2 minutes, glucose concentrations from 0 mM to 20 mM, temperature 37 °C; rotation rate 400 rpm, pH7 with other parameters given in Table 5-3 and Table 5-4..... 70

Figure 5-7: Simulated steady state response of the model showing the influence of thickness on the GOx modified TTF-Gelatin electrodes. a) at 5 mM, b) at 20 mM. Conditions: temperature of 37 °C, and rotation rate of 400 rpm, with other parameters given in Table 5-3 and Table 5-4..... 73

Figure 5-8: Dependence of electrode performance with the change in the electrode thickness on a) TTF and GOx loading; b) enzyme loading (projection from a); and c) mediator loading (projection from a). Spectra: simulation, symbols: experimental data. Other conditions:  $E=0.3844$  V vs. SHE fixed delay of 2 minutes, glucose concentration of 20 mM, temperature 37 °C; rotation rate 400 rpm, pH7, porosity ( $\epsilon$ ) 0.35, with other parameters given in Table 5-3 and Table 5-4 ..... 75

Figure 5-9: a) Dependence of thin electrode performance with changing porosity on a) TTF and GOx loading; b) enzyme loading; and c) mediator loading. Spectra: simulation, symbols – experimental data at the loading of 20.10.10 ratio. Other conditions:  $E=0.3844$  V vs. SHE, 20  $\mu$ L of ink loading, fixed delay of 2 minutes, glucose

concentration of 20 mM, temperature 37 °C; rotation rate 400 rpm, pH7, with other parameters given in Table 5-3 and Table 5-4 .....	76
Figure 5-10: a) Steady state polarization curves of MET porous electrode with PVDF procedure with O <sub>2</sub> supply: symbols – experimental data, lines – simulated curves b) simulated transient profiles of glucose concentration at 5mM and 20 mM. Conditions: ratio in mg of Vulcan-TTF-enzyme (20-10-10), fixed delay of 2 minutes, temperature 25 °C, pH6, rotation rate 400 rpm, with other parameters given in Table 5-1, Table 5-2 and Table 5-6.....	78
Figure 5-11: Simulated transient (at fixed position in the middle of CL) and steady state (along spatial coordinate) profiles of glucose concentration a) O <sub>2</sub> and b) H <sub>2</sub> O <sub>2</sub> . Conditions: temperature 25°C pH6, rotation rate 400 rpm, with other parameters given in Table 5-1, Table 5-3 and Table 5-6 .....	79
Figure 5-12: Steady state polarisation curves at a) pH5 and b) pH6 for H <sub>2</sub> O <sub>2</sub> reduction on HRP modified graphite electrode; symbols – experimental data and lines – simulated curves (M <sub>1</sub> – blue dotted line, M <sub>2</sub> – green dashed line and M <sub>3</sub> – black solid line). Conditions: fixed delay of 1 minute, H <sub>2</sub> O <sub>2</sub> concentrations from 10 to 160 μM, room temperature; rotation rate 400 rpm; with the parameters for the simulations given in Table 5-7.....	82
Figure 5-13: Experimental EIS (symbols) vs. simulated (lines-M <sub>3</sub> ) at three potentials; a) pH5 at 80 μM H <sub>2</sub> O <sub>2</sub> concentration, b) pH6 at 80 μM H <sub>2</sub> O <sub>2</sub> concentration and (c) pH6 at 160 μM H <sub>2</sub> O <sub>2</sub> concentration. Other conditions: 25°C and rotation rate of 400 rpm, with other parameters as shown in Table 5-9 .....	86
Figure 5-14: Simulated EIS of M <sub>3</sub> showing the influence of the variation of the reaction rate constants with respect to their optimized values (Table 5-8) a) variation of $k_{cat}$ at pH6 and b) variation of $k_e$ at pH6. Other conditions: 160 μM H <sub>2</sub> O <sub>2</sub> concentration, room temperature, rotation rate 400 rpm.....	89
Figure 5-15: Steady state polarization curves of PVDF electrodes: symbols – experimental data, dashed lines – simulated curves of reduced 1-D model; continuous lines – simulated curves of full 1-D model. a) thin porous electrode b) thick porous electrode. Conditions: fixed delay of 1 minute, H <sub>2</sub> O <sub>2</sub> concentrations of 80 μM and 160 μM, room temperature; rotation rate 400 rpm, with other parameters given in Table 5-10 and Table 5-9 .....	91
Figure 5-16: a) Steady state profile of H <sub>2</sub> O <sub>2</sub> concentration for the thin and thick electrodes at different applied potentials. Conditions: PVDF electrode, fixed delay of 1 minute, H <sub>2</sub> O <sub>2</sub> concentrations at 160 μM, room temperature; rotation rate 400 rpm, pH5, with other parameters given in Table 5-9 and Table 5-10 .....	93

- Figure 5-17: a) Steady state polarization curves of the thin and thick Gelatin electrodes: symbols – experimental data, continuous lines – simulated curves of 1-D model; b) simulated local profiles of  $H_2O_2$  concentration for a thin (in black) and a thick (in blue) porous electrode along the spatial coordinate. Conditions: fixed delay of 1 minute,  $H_2O_2$  concentrations of 80 and 160  $\mu M$ , room temperature; rotation rate 400 rpm, pH5, with other parameters given in Table 5-9 and Table 5-11 ..... 95
- Figure 5-18: a) Steady state polarization curves at high concentration for the thick electrode: symbols – experimental data, continuous lines – simulated curves of 1-D model; b) simulated local profiles of  $H_2O_2$  concentration for the Gelatin (in black) and PVDF (in blue) electrode along the spatial coordinate. Conditions: fixed delay of 1 minute,  $H_2O_2$  concentrations of 1000  $\mu M$  and 3000  $\mu M$ , room temperature, rotation rate 400 rpm, pH5, with other parameters given in Table 5-9 and Table 5-11 ..... 98
- Figure 5-19: Simulated steady state polarization curves by increasing HRP at a fixed concentration of GOx: a) simulation c) experiment and increase in GOx at a fixed concentration of HRP: b) simulation d) experiment. Conditions: 20 mM of glucose concentration, porous electrode, fixed delay of 2 minutes, pH6, 25 °C; rotation rate 400 rpm; parameters for the simulations are given in Table 5-9 and Table 5-12... 100
- Figure 5-20: Simulated transient (at fixed position in the middle of CL) and steady state (along the spatial coordinate) profiles of a) glucose ( $S_2$ ) concentration b)  $O_2$  at 20 mM of glucose concentration. Conditions: temperature 25°C, pH6, rotation rate 400 rpm, with other parameters given in Table 5-9 and Table 5-12 ..... 102
- Figure 5-21: Simulated transient (at fixed position in the middle of CL) and steady state (along spatial coordinate) profiles of  $H_2O_2$  concentration at a) different applied potentials at enzyme ratio 1:1 b) different ratios. Conditions: 20 mM of  $S_2$ , 25°C, pH6, rotation rate 400 rpm, with other parameters given Table 5-9 and Table 5-12 ..... 103
- Figure 5-22: Simulated steady state performance of the enzymatic DET electrode with different scenarios of  $O_2$  supply, rotation rate 400 rpm, and with other parameters given in Table 5-9 and Table 5-12..... 104
- Figure 5-23: Simulated transient (at fixed position in the middle of CL) and steady state (along the spatial coordinate) profiles of a) glucose concentrations and b)  $O_2$  at different  $O_2$  supply scenarios. Conditions: 0.25 V, pH6, 25°C, rotation rate 400 rpm, with other parameters given in Table 5-9 and Table 5-12 ..... 104
- Figure 5-24: Simulated transient (middle of CL) and steady state (along spatial coordinate) profiles of  $S_1$  concentrations a) at 5 mM and b) 20 mM of glucose concentration. Conditions: 0.25 V, pH6, 25°C, rotation rate 400 rpm, with other parameters given in Table 5-9 and Table 5-12..... 105

## List of tables

Table 1-1: Summary of enzyme electrode models in the literature.....	5
Table 2-1: Survey of DET and MET.....	11
Table 2-2: Charge balance of the electron conducting phase .....	17
Table 2-3: Charge balance of the ionic conducting phase.....	18
Table 2-4: Charge balances at the electrochemical interface inside the CL.....	18
Table 2-5: Charge balance at quasi-stationary conditions .....	19
Table 2-6: General mass balance equation .....	19
Table 2-7: Mathematical expressions of a reduced 1-D model (Appendix 1) .....	20
Table 2-8: Interface and distributed models .....	21
Table 2-9: A typical PDE with IC and BCs .....	22
Table 2-10: Defined quantities for FVM discretization.....	23
Table 2-11: Definition of input and output variables .....	30
Table 3-1: Mathematical equations of charge balances inside the CL and DL.....	37
Table 3-2: Reaction mechanism and reaction rate of GOx-TTF in the presence of glucose .....	38
Table 3-3: Model variants of the MET(GOx-TTF) system.....	39
Table 3-4: Mass balance of all related species of the system: glucose oxidation using GOx -TTF in a porous conductive matrix [117] .....	39
Table 3-5: Detailed reaction mechanism and rate expression of the system: glucose oxidation using GOx - TTF in a porous conductive matrix with additional O <sub>2</sub> supply.....	41
Table 3-6: Mass balance of related species of the system: glucose oxidation using GOx -TTF in a porous conductive matrix with additional O <sub>2</sub> supply.....	42
Table 3-7: Model variant of MET (GOx-TTF) system with O <sub>2</sub> supply .....	43
Table 3-8: Detailed reaction mechanism and reaction rate expression of HRP on a conductive surface .....	44
Table 3-9: Mass balances of all related species on the thin film electrode using HRP in the presence of H <sub>2</sub> O <sub>2</sub> .....	46
Table 3-10: Final expression of the electrochemical steady state reaction rate of the three mechanistic models using the BV approach .....	47
Table 3-11: Mass balances of all related species in the CL and DL of a/the porous electrode. System: porous DET electrode using HRP as a model enzyme .....	49
Table 3-12: Mass balance of all related species in the enzymatic cascade.....	51
Table 3-13: BCs and ICs of the enzymatic cascade with different O <sub>2</sub> supply scenarios .....	52

Table 5-1: Overall simulation parameters for GOx modified Vulcan-TTF-PVDF electrodes.....	60
Table 5-2 Optimized simulation parameters for the GOx modified Vulcan-TTF-PVDF electrodes .....	63
Table 5-3: Overall modelling parameters for the GOx modified TTF-Gelatin electrodes. ....	69
Table 5-4: Optimized parameters of the GOx modified TTF-Gelatin electrodes, pH7, 37°C.....	71
Table 5-5: Optimized parameters in the presence of O <sub>2</sub> .....	78
Table 5-6: Kinetic constants $K_{11}$ on different studied systems in the literature .....	84
Table 5-7: Optimized parameter values based on steady state data for all three models under different conditions of pH and H <sub>2</sub> O <sub>2</sub> concentrations .....	85
Table 5-8: Optimized parameter values based on EIS data for M <sub>3</sub> with different pH(s).....	87
Table 5-9: Model parameters of porous HRP modified electrodes.....	90
Table 5-10: Estimated parameter values for the porous HRP modified Vulcan- PVDF electrodes under different conditions of ink loading and H <sub>2</sub> O <sub>2</sub> concentrations.....	92
Table 5-11: Estimated parameter values for porous HRP modified Vulcan- Gelatin electrodes under different conditions of ink loading and H <sub>2</sub> O <sub>2</sub> concentrations.....	96
Table 5 12: Model parameters for simulation of the porous GOx-HRP modified Vulcan PVDF electrodes.....	100
Table 6-1: Further possible extensions of the current work .....	110



## Bibliography

- [1] S.C. Barton, J. Gallaway, P. Atanassov, Enzymatic biofuel cells for implantable and microscale devices, *Chemical Reviews*, 104 (2004) 4867-4886.
- [2] J.K. Guterl, V. Sieber, Biosynthesis “debugged”: Novel bioproduction strategies, *Engineering in Life Sciences*, 13 (2013) 4-18.
- [3] R.N. Patel, *Biocatalysis in the Pharmaceutical and biotechnology industries*, Edited by Ramesh N. Patel. CRC Press: Boca Raton, FL and London. 2007, *Organic Process Research & Development*, 11 (2007) 296-296.
- [4] L.C. Jr Clark, EW Clark, A personalized history of the Clark oxygen electrode, *International Anesthesiology Clinics*, 3(25) (1987) 1–29.
- [5] P.N. Bartlett, C.S. Toh, E.J. Calvo, V. Flexer, Modelling biosensor responses, in: *bioelectrochemistry*, John Wiley & Sons, Ltd, (2008) 267-325.
- [6] K. Habermüller, M. Mosbach, W. Schuhmann, Electron-transfer mechanisms in amperometric biosensors, *Fresenius' journal of analytical chemistry*, 366 (2000) 560-568.
- [7] I. Ivanov, T. Vidaković-Koch, K. Sundmacher, Recent advances in enzymatic fuel cells: Experiments and modeling, *Energies*, 3 (2010) 803-846.
- [8] D. Leech, P. Kavanagh, W. Schuhmann, Enzymatic fuel cells: Recent progress, *Electrochimica Acta*, 84 (2012) 223-234.
- [9] J. Kim, H. Jia, P. Wang, Challenges in biocatalysis for enzyme-based biofuel cells, *Biotechnology Advances*, 24 (2006) 296-308.
- [10] T. Krieg, A. Sydow, U. Schröder, J. Schrader, D. Holtmann, Reactor concepts for bioelectrochemical syntheses and energy conversion, *Trends in Biotechnology*, 32 (2014) 645-655.
- [11] R. Basséguy, K. Délécouls-Servat, A. Bergel, Glucose oxidase catalysed oxidation of glucose in a dialysis membrane electrochemical reactor (D-MER), *Bioprocess and Biosystems Engineering*, 26 (2004) 165-168.
- [12] C. Bourdillon, R. Lortie, J.M. Laval, Gluconic acid production by an immobilized glucose oxidase reactor with electrochemical regeneration of an artificial electron acceptor, *Biotechnology and Bioengineering*, 31 (1988) 553-558.
- [13] B. Brielbeck, M. Frede, E. Steckhan, Continuous Electroenzymatic synthesis employing the electrochemical enzyme membrane reactor, *Biocatalysis*, 10 (1994) 49-64.
- [14] R. Devaux-Basséguy, P. Gros, A. Bergel, Electroenzymatic processes: A clean technology alternative for highly selective synthesis?, *Journal of Chemical Technology and Biotechnology*, 68 (1997) 389-396.

- [15] R. DiCosimo, C.H. Wong, L. Daniels, G.M. Whitesides, Enzyme-catalyzed organic synthesis: electrochemical regeneration of NAD(P)H from NAD(P) using methyl viologen and flavoenzymes, *The Journal of Organic Chemistry*, 46 (1981) 4622-4623.
- [16] C. Kohlmann, W. Märkle, S. Lütz, Electroenzymatic synthesis, *Journal of Molecular Catalysis B: Enzymatic*, 51 (2008) 57-72.
- [17] I. Bergel, M. Comtat, Electroenzymatic reactors with coenzyme regeneration: A theoretical approach, *Biotechnology and Bioengineering*, 28 (1986) 728-735.
- [18] H. Maeda, S. Kajiwara, Malic acid production by an electrochemical reduction system combined with the use of diaphorase and methylviologen, *Biotechnology and Bioengineering*, 27 (1985) 596-602.
- [19] I. Mazurenko, M. Etienne, G.W. Kohring, F. Lopicque, A. Walcarius, Enzymatic bioreactor for simultaneous electrosynthesis and energy production, *Electrochimica Acta*, 199 (2016) 342-348.
- [20] M. Varničić, T. Vidaković-Koch, K. Sundmacher, Gluconic Acid Synthesis in an Electroenzymatic Reactor, *Electrochimica Acta*, 174 (2015) 480-487.
- [21] McNeil, Archer, Giavasis, Harvey Microbial Production of Food Ingredients, *Enzymes and Nutraceuticals*, 1st Edition, Woodhead Publishing, 2013.
- [22] R.A.S. Luz, A.R. Pereira, J.C.P. de Souza, F.C.P.F. Sales, F.N. Crespilho, Enzyme biofuel cells: thermodynamics, kinetics and challenges in applicability, *ChemElectroChem*, 1 (2014) 1751-1777.
- [23] R.F. Taylor. A comparison of various commercially-available liquid chromatographic. Vols. supports for immobilization of enzymes, and immunoglobulins. *Analytica. Chimica.acta*, 172 (1985) 241–248.
- [24] R.J. Kazlauskas, U.T. Bornscheuer, Finding better protein engineering strategies, *Nature Chemical Biology* 5, (2009), 526 – 529.
- [25] D.J. Caruana, S. Howorka, Biosensors and biofuel cells with engineered proteins, *Molecular BioSystems*, 6 (2010) 1548-1556.
- [26] G. Güven, R. Prodanovic, U. Schwaneberg, Protein Engineering – An Option for enzymatic biofuel cell design, *Electroanalysis*, 22 (2010) 765-775.
- [27] A.J. Bard, M. Stratmann, G.S. Wilson, ed., *Encyclopedia of electrochemistry Volume 9: Bioelectrochemistry*, Wiley VCH: Weinheim, 2002.
- [28] D.I. Fried, F.J. Brieler, and M. Froba, Designing Inorganic Porous materials for enzyme adsorption and applications in biocatalysis. *Chemcatchem*, (5(4) 2013) 862-884.
- [29] Z. Zhou, M. Hartmann, Progress in enzyme immobilization in ordered mesoporous materials and related applications, *Chemical Society Reviews*, 42 (2013) 3894-3912.
- [30] M.E.G. Lyons, Transport and kinetics at carbon nanotube -redox enzyme composite modified electrode biosensors part 2. redox enzyme dispersed in nanotube mesh of finite thickness, *International Journal of Electrochemical Science*, 4 (2009) 1196-1236.

- [31] R. Baronas, J. Kulys, K. Petrauskas, J. Razumiene, Modelling carbon nanotubes-based mediatorless biosensor, *Sensors (Switzerland)*, 12 (2012) 9146-9160.
- [32] S. Calabrese Barton, Oxygen transport in composite mediated biocathodes, *Electrochimica Acta*, 50 (2005) 2145-2153.
- [33] D.-S. Chan, D.-J. Dai, H.-S. Wu, Dynamic Modeling of Anode Function in Enzyme-Based Biofuel Cells Using High Mediator Concentration, *Energies*, 5 (2012) 2524.
- [34] D.J. Glykys, S. Banta, Metabolic control analysis of an enzymatic biofuel cell, *Biotechnol Bioeng*, 102 (2009) 1624-1635.
- [35] S.W. Jeon, J.Y. Lee, J.H. Lee, S.W. Kang, C.H. Park, S.W. Kim, Optimization of cell conditions for enzymatic fuel cell using statistical analysis, *Journal of Industrial and Engineering Chemistry*, 14 (2008) 338-343.
- [36] E. Kjeang, D. Sinton, D.A. Harrington, Strategic enzyme patterning for microfluidic biofuel cells, *Journal of Power Sources*, 158 (2006) 1-12.
- [37] M.H. Osman, A.A. Shah, R.G.A. Wills, F.C. Walsh, Mathematical modelling of an enzymatic fuel cell with an air-breathing cathode, *Electrochimica Acta*, 112 (2013) 386-393.
- [38] V.Z. Rubin, L. Mor, Physical modeling of the enzymatic glucose-fuelled fuel cells, *Advances in Chemical Engineering and Science*(2013) 218-226.
- [39] K. Délécouls-Servat, A. Bergel, R. Basseguy, Design and modelling of a dialysis membrane electrochemical reactor (D-MER) for oxidoreductase-catalysed synthesis, *Journal of Applied Electrochemistry*, 34 (2004) 469-476.
- [40] R. Ruinatscha, V. Höllrigl, K. Otto, A. Schmid, Productivity of selective electroenzymatic reduction and oxidation reactions: theoretical and practical considerations, *Advanced Synthesis & Catalysis*, 348 (2006) 2015-2026.
- [41] M. Rasi, L. Rajendran, M.V Sangaranarayanan. Enzyme-catalyzed oxygen reduction reaction in biofuel cells: Analytical expressions for chronoamperometric current densities *Journal of the Electrochemical Society*, 162 (9) (2015) H671-H680.
- [42] R. Muthuramalingam, R. Lakshmanan. Theoretical analysis of the enzyme reaction processes within the multiscale porous biocatalytic electrodes, *Russian Journal of Electrochemistry*, 52 (2016) 143–153.
- [43] A.S. Bedekar, J.J. Feng, S. Krishnamoorthy, K.G. Lim, G.T.R. Palmore, S. Sundaram, Oxygen limitation in microfluidic biofuel cells, *Chemical Engineering Communications*, 195 (2008) 256-266.
- [44] B. Limoges, J. M. Savéant , and D. Yazidi and Surface, Quantitative Analysis of Catalysis and Inhibition at Horseradish Peroxidase Monolayers Immobilized on an Electrode, *J Am Chem Soc.*, 125(30) (2003) 9192-203.
- [45] O.R. Zaborisky, *Enzymes: Biological catalyst in: Advanced materials in catalysis*, Academic Press, (1977), 267-291.

- [46] E. Fischer, Einfluss der Configuration auf die Wirkung der Enzyme, Berichte der Deutschen Chemischen Gesellschaft, 27 (1894) 2985-2993.
- [47] D.E. Koshland, Application of a theory of enzyme specificity to protein synthesis, Proceedings of the National Academy of Sciences of the United States of America, 44 (1958) 98-104.
- [48] D. Mackey, A.J. Killard, A. Ambrosi, M.R. Smyth, Optimizing the ratio of horseradish peroxidase and glucose oxidase on a bienzyme electrode: Comparison of a theoretical and experimental approach, Sensors and Actuators B: Chemical, 122 (2007) 395-402.
- [49] M. Delvaux, A. Walcarius, S. Demoustier-Champagne, Bienzyme HRP-GOx-modified gold nanoelectrodes for the sensitive amperometric detection of glucose at low overpotentials, Biosensors and Bioelectronics, 20 (2005) 1587-1594.
- [50] G.T.R. Palmore, H. Bertschy, S.H. Bergens, G.M. Whitesides, . A methanol/dioxygen biofuel cell that uses NAD<sup>+</sup>-dependent dehydrogenases as catalysts: application of an electro-enzymatic method to regenerate nicotinamide adenine dinucleotide at low overpotentials, Journal of Electroanalytical Chemistry, 443 (1998) 155-161.
- [51] Z. Zhu, T. Kin Tam, F. Sun, C. You, Y.H. Percival Zhang, A high-energy-density sugar biobattery based on a synthetic enzymatic pathway, Nat Commun., 5 (2014) 5:3026.
- [52] R.A. Marcus, N. Sutin, Electron transfers in chemistry and biology, Biochimica et Biophysica Acta (BBA) - Reviews on Bioenergetics, 811 (1985) 265-322.
- [53] M. Falk, Z. Blum, S. Shleev, Direct electron transfer based enzymatic fuel cells, Electrochimica Acta, 82 (2012) 191-202.
- [54] A. Ramanavicius, A. Ramanaviciene, Hemoproteins in Design of Biofuel Cells, Fuel Cells, 9 (2009) 25-36.
- [55] A. Chaubey, B.D. Malhotra, Mediated biosensors, Biosensors and Bioelectronics, 17 (2002) 441-456.
- [56] P. Kavanagh, D. Leech, Mediated electron transfer in glucose oxidising enzyme electrodes for application to biofuel cells: recent progress and perspectives, Physical Chemistry Chemical Physics, 15 (2013) 4859-4869.
- [57] S. Shleev, A. Jarosz-Wilkolazka, A. Khalunina, O. Morozova, A. Yaropolov, T. Ruzgas, L. Gorton, Direct electron transfer reactions of laccases from different origins on carbon electrodes, Bioelectrochemistry, 67 (2005) 115-124.
- [58] P. Ramírez, N. Mano, R. Andreu, T. Ruzgas, A. Heller, L. Gorton, S. Shleev, . Direct electron transfer from graphite and functionalized gold electrodes to T1 and T2/T3 copper centers of bilirubin oxidase, Biochimica et Biophysica Acta (BBA) - Bioenergetics, 1777 (2008) 1364-1369.
- [59] H.Y. Zhao, H.M. Zhou, J.X. Zhang, W. Zheng, Y.F. Zheng, Carbon nanotube-hydroxyapatite nanocomposite: A novel platform for glucose/O<sub>2</sub> biofuel cell, Biosensors and Bioelectronics, 25 (2009) 463-468.

- [60] S.C. Wang, F. Yang, M. Silva, A. Zarow, Y. Wang, Z. Iqbal, Membrane-less and mediator-free enzymatic biofuel cell using carbon nanotube/porous silicon electrodes, *Electrochemistry Communications*, 11 (2009) 34-37.
- [61] X. Wu, F. Zhao, J.R. Varcoe, A.E. Thumser, C. Avignone-Rossa, R.C.T. Slade, A one-compartment fructose/air biological fuel cell based on direct electron transfer, *Biosensors and Bioelectronics*, 25 (2009) 326-331.
- [62] S.D. Minteer, P. Atanassov, H.R. Luckarift, G.R. Johnson, New materials for biological fuel cells, *Materials Today*, 15 (2012) 166-173.
- [63] A.A. Babadi, S. Bagheri, S.Bee A. Hamid, Progress on implantable biofuel cell: Nano-carbon functionalization for enzyme immobilization enhancement, *Biosensors and Bioelectronics*, 79 (2016) 850-860.
- [64] A. Zebda, S. Cosnier, J.P. Alcaraz, M. Holzinger, A. Le Goff, C. Gondran, F. Boucher, F. Giroud, K. Gorgy, H. Lamraoui, P. Cinquin, Single Glucose Biofuel Cells Implanted in Rats Power Electronic Devices, *Scientific Reports*, 3 (2013) 1516.
- [65] I. Ivanov, T. Vidaković-Koch, K. Sundmacher, Direct hybrid glucose–oxygen enzymatic fuel cell based on tetrathiafulvalene–tetracyanoquinodimethane charge transfer complex as anodic mediator, *Journal of Power Sources*, 196 (2011) 9260-9269.
- [66] H. Sakai, T. Nakagawa, Y. Tokita, T. Hatazawa, T. Ikeda, S. Tsujimura, K. Kano, A high-power glucose/oxygen biofuel cell operating under quiescent conditions, *Energy & Environmental Science*, 2(1), (2009), 133-138.
- [67] A. Heller, Potentially implantable miniature batteries, *Analytical and Bioanalytical Chemistry*, 385(3) (2005) 469-473.
- [68] R.A. Bullen, T.C. Arnot, J.B. Lakeman, F.C. Walsh, Biofuel cells and their development, *Biosensors & Bioelectronics*, 21(11) (2006) 2015-2045.
- [69] P. Cinquin, C. Gondran, F. Giroud, S. Mazabrard, A. Pellissier, F. Boucher, J.-P. Alcaraz, K. Gorgy, F. Lenouvel, S. Mathé, P. Porcu, S. Cosnier. A glucose biofuel cell implanted in rats. *PLoS one* 5, no. 5 (2010) e10476.
- [70] R. Basseguy, K. Delecouls-Servat, A. Bergel, Glucose oxidase catalysed oxidation of glucose in a dialysis membrane electrochemical reactor (D-MER), *Bioprocess Biosyst Eng*, 26 (2004) 165-168.
- [71] J.M. Obón, P. Casanova, A. Manjón, V.M. Fernández, J.L. Iborra, Stabilization of glucose dehydrogenase with polyethyleneimine in an electrochemical reactor with NAD(P)<sup>+</sup> regeneration, *Biotechnology Progress*, 13 (1997) 557-561.
- [72] A. Manjón, J.M. Obón, P. Casanova, V.M. Fernández, J.L. Iborra, Increased activity of glucose dehydrogenase co-immobilized with a redox mediator in a bioreactor with electrochemical NAD<sup>+</sup> regeneration, *Biotechnology Letters*, 24 (2002) 1227-1232.
- [73] R.W. Coughlin, M. Aizawa, B.F. Alexander, M. Charles, Immobilized-enzyme continuous-flow reactor incorporating continuous electrochemical regeneration of NAD, *Biotechnology and Bioengineering*, 17 (1975) 515-526.

- [74] A. Bergel, M. Comtat, Electroenzymatic reactors with coenzyme regeneration: A theoretical approach, *Biotechnology and Bioengineering*, 28 (1986) 728-735.
- [75] A.Z. Weber, J. Newman, Modeling transport in polymer-electrolyte fuel cells, *Chemical reviews*, 104 (2004) 4679-4726.
- [76] T. Vidakovic-Koch, R. Hanke-Rauschenbach, I. Gonzalez Martinez, K. Sundmacher, catalyst layer modeling for gas diffusion electrodes, C. Breitkopf, K. Swider Lyons (Eds.), *Springer Handbook of Electrochemistry*, Ch.9, Springer, 2014.
- [77] J. Justin Gooding, Elizabeth A. H. Hall and D. Brynn Hibbert, from thick films to monolayer recognition layers in Amperometric Enzyme Electrodes, *Electroanalysis* (1998) 1130-1136.
- [78] B.t. Limoges, J. Moiroux, J.-M. , Kinetic control by the substrate. and the cosubstrate in electrochemically monitored redox enzymatic immobilized systems.Savéant Catalytic responses in cyclic voltammetry and steady state techniques, *Journal of Electroanalytical Chemistry*, 521 (2002) 8-15.
- [79] P.N. Bartlett, K.F.E. Pratt: Theoretical treatment of diffusion and kinetics in amperometric immobilized enzyme electrodes Part I: Redox mediator entrapped within the film, *Journal of Electroanalytical Chemistry*, 397 (1-2) 1995 61-78.
- [80] S. Loghambal, L. Rajendran, Mathematical modeling in amperometric oxidase enzyme–membrane electrodes, *Journal of Membrane Science*, 373 (1-2) (2011) 20-28.
- [81] Q. Wu, G. D. Storrer, F. Pariente et al., A nitrite biosensor immobilized on an electropolymerized film of a pyrrole, *Anal Chem.* (1997) 4856-4863.
- [82] W.J. Albery and P. N. Bartlett, Amperometric enzyme electrodes. 1. Theory, *J. Electroanal. Chem.*, 194 (1985), 211–222.
- [83] W.J. Albery, P. N. Bartlett and D. H. Craston, Amperometric enzyme electrodes. 2. Conducting salts as electrode materials for the oxidation of glucose oxidase, *J. Electroanal. Chem.*, 194 (1985) 223–235.
- [84] T. Schulmeister and D. Pfeiffer, Mathematical-modeling of amperometric enzyme electrodes with perforated membranes, *Biosens. & Bioelectr.*, 8 (1993) 75–79.
- [85] B.W. Bequette. *Process dynamics: modeling, analysis and simulation*, Prentice Hall PTR, New Jersey 1998.
- [86] K. Yokoyama and Y. Kayanuma, Cyclic voltammetric simulation for electrochemically mediated enzyme reaction and determination of enzyme kinetic constants, *Anal. Chem.*, 70 (1998) 3368–3376.
- [87] M.E.G. Lyons, C. H. Lyons, C. Fitzgerald and P. N. Bartlett, Conducting-polymer-based electrochemical sensors -theoretical-analysis of the transient current response, *J. Electroanal. Chem.*, 365 (1994) 29–34.
- [88] W.J. Albery, P. N. Bartlett, B. J. Driscoll and R. B. Lennox, Amperometric enzyme electrodes. 5. The homogeneous mediated mechanism, *J. Electroanal. Chem.*, 323 (1992) 77–102.

- [89] J. Galceran, S. L. Taylor and P. N. Bartlett, Modelling the steady-state current at the inlaid disc microelectrode for homogeneous mediated enzyme catalysed reactions, *J. Electroanal. Chem.*, 506 (2001) 65–81.
- [90] P.N. Bartlett and K.F.E. Pratt, Theoretical treatment of diffusion and kinetics in amperometric immobilized enzyme electrodes .1. redox mediator entrapped within the film, *J. Electroanal. Chem.*, 397 (1995) 61–78.
- [91] W.H. Press, B. Flannery, S. A. Teukolsky and W. T. Vetterling, *Numerical recipes, the art of scientific computing*, 1st edn., Cambridge University Press, Cambridge, (1986).
- [92] J. L. Besombes, S. Cosnier and P. Labbe, Polyphenol oxidase-catechol: an electroenzymatic model system for characterizing the performance of matrices for biosensors, *Talanta*, 43 (1996) 1615–1619.
- [93] T. Nakaminami, S. Ito, S. Kuwabata and H. Yoneyama, A biomimetic phospholipid/alkanethiolate bilayer immobilizing uricase and an electron mediator on an Au electrode for amperometric determination of uric acid, *Anal. Chem.*, 71 (1999) 4278–4283.
- [94] D.E. Smith in *Electroanalytical Chemistry*, A.J. Bard, Ed., Dekker, New York, Vol. 1, 1966, p.1.
- [95] J. M. Le Canut, R. M. Abouatallah, and D. A. Harrington. Detection of membrane drying, fuel cell flooding, and anode catalyst poisoning on PEMFC stacks by electrochemical impedance spectroscopy. *J. Electrochem. Soc.*, 153(5) (2006) A857 A864.
- [96] M. Ciureanu and R. Roberge. Electrochemical impedance study of PEM fuel cells. experimental diagnostics and modeling of air cathodes. *J. Phys. Chem. B*, 105(17) (2001) 3531–3539.
- [97] B. Bensmann, M. Petkovska, T. Vidaković-Koch, R. Hanke-Rauschenbach, and K. Sundmacher. Nonlinear frequency response of electrochemical methanol oxidation kinetics: a theoretical analysis. *Journal of the Electrochemical Society*, 157(9) (2010) B1279-B1289.
- [98] T. R., Vidaković-Koch, V. V. Panić, M. Andrić, M. Petkovska, and K. Sundmacher. Nonlinear frequency response analysis of the ferrocyanide oxidation kinetics. Part I. A Theoretical analysis. *The Journal of Physical Chemistry C*, 115 (35) (2011) 17341-17351.
- [99] P. Vladimir V., T. R. Vidakovic-Koch, M. Andric, M. Petkovska, and K. Sundmacher. Nonlinear frequency response analysis of the ferrocyanide oxidation kinetics. Part II. Measurement routine and experimental validation. *The Journal of Physical Chemistry C* 115(35) (2011) 17352-17358.
- [100] T. Vidaković-Koch, V.K. Mittal, T.Q.N. Do, M. Varničić, K. Sundmacher, Application of electrochemical impedance spectroscopy for studying of enzyme kinetics, *Electrochimica Acta*, 110 (2013) 94-104.
- [101] F. Patolsky, M. Zayats, E. Katz, I. Willner, Precipitation of an Insoluble Product on Enzyme Monolayer Electrodes for Biosensor Applications: Characterization by Faradaic Impedance

Spectroscopy Cyclic Voltammetry, and Microgravimetric Quartz Crystal Microbalance Analyses, *Analytical Chemistry*, 71 (1999) 3171-3180.

- [102] H.Y. Gu, A.M. Yu, H.Y. Chen. Direct electron transfer and characterization of hemoglobin immobilized on Au colloid–cysteamine-modified gold electrode. *Journal of Electroanalytical Chemistry* 516(1) (2001) 119-126.
- [103] J.-J. Feng, G. Zhao, J.-J. Xu, H.-Y. Chen, Direct electrochemistry and electrocatalysis of heme proteins immobilized on gold nanoparticles stabilized by chitosan, *Analytical Biochemistry*, 342 (2005) 280-286.
- [104] E. Katz, I. Willner, Probing biomolecular interactions at conductive and semiconductive surfaces by impedance spectroscopy: Routes to impedimetric immunosensors, DNA-Sensors, and Enzyme Biosensors, *Electroanalysis*, 15 (2003) 913-947.
- [105] B. Bensmann, R. Hanke-Rauschenbach, E. Meißner, I. Koch, K. Sundmacher, Model simulation and analysis of proton incorporation into the positive active mass of a lead/acid battery, *Journal of The Electrochemical Society*, 157 (2010) A243-A253.
- [106] M.T. Stankovich, L.M. Schopfer, V. Massey, Determination of glucose oxidase oxidation-reduction potentials and the oxygen reactivity of fully reduced and semiquinoid forms, *The Journal of biological chemistry*, 253 (1978) 4971-4979.
- [107] C.J. Kay, M.J. Barber, L.P. Solomonson, CD and potentiometry of FAD, heme and molybdenum-pterin prosthetic groups of assimilatory nitrate reductase, *Biochemistry*, 27 (1988) 6142-6149.
- [108] P.W. Anderson, P.A. Lee, M. Saitoh, Remarks on giant conductivity in TTF-TCNQ, *Solid State Communications*, 13 (1973), 595–598.
- [109] D. Jaeger, A. J. Bard, Electrochemical behavior of donor-tetracyanoquinodimethane electrodes in aqueous media, *J. Am. Chem. Soc.*, 101 (1979) 1690-1699.
- [110] N.K. Čenas, J.J. Kulys, Biocatalytic oxidation of glucose on the conductive charge transfer complexes, *Journal of Electroanalytical Chemistry and Interfacial Electrochemistry*, 128 (1981) 103-113.
- [111] C. Bourdillon, C. Demaille, J. Moiroux, J.M. Savéant, . New insights into the enzymatic catalysis of the oxidation of glucose by native and recombinant glucose oxidase mediated by electrochemically generated one-electron redox cosubstrates, *Journal of the American Chemical Society*, 115 (1993) 1-10.
- [112] N. Anicet, C. Bourdillon, C. Demaille, J. Moiroux, J.M. Savéant,. Catalysis of the electrochemical oxidation of glucose by glucose oxidase and a single electron cosubstrate: Kinetics in viscous solutions, *Journal of Electroanalytical Chemistry*, 410 (1996) 199-202.
- [113] M.S. Freund, A. Brajter-Toth, M.D. Ward, Electrochemical and quartz crystal : s.n. microbalance evidence for mediation and direct electrochemical reactions of small molecules at tetrathiafulvalenete, *Journal of Electroanalytical Chemistry and Interfacial Electrochemistry*, 289 (1990) 127-141.



- [114] I. Ivanov, T. Vidaković-Koch, K. Sundmacher, Alternating electron transfer mechanism in the case of high-performance tetrathiafulvalene–tetracyanoquinodimethane enzymatic electrodes, *Journal of Electroanalytical Chemistry*, 690 (2013) 68-73.
- [115] P.N. Bartlett, V.Q. Bradford, Modification of glucose oxidase by tetrahydrofulvalene, *Journal of the Chemical Society - Series Chemical Communications*, (1990) 1135-1136.
- [116] T.Q.N. Do, M. Varničić, R.J. Flassig, T. Vidaković-Koch, K. Sundmacher, Dynamic and steady state 1-D model of mediated electron transfer in a porous enzymatic electrode, *Bioelectrochemistry*, 106, Part A (2015) 3-13.
- [117] T.Q.N. Do, M. Varničić, R. Hanke-Rauschenbach, T. Vidaković-Koch, K. Sundmacher, Mathematical modeling of a porous enzymatic electrode with direct electron transfer mechanism, *Electrochimica Acta*, 137 (2014) 616-626.
- [118] K. Kleppe, The effect of hydrogen peroxide on glucose oxidase from *Aspergillus niger*\*, *Biochemistry*, 5 (1966) 139-143.
- [119] N. Martens, E.A.H. Hall, Model for an immobilized oxidase enzyme electrode in the presence of two oxidants, *Analytical Chemistry*, 66 (1994) 2763-2770.
- [120] C. Bourdillon, J.P. Bourgeois, D. Thomas, Covalent linkage of glucose oxidase on modified glassy carbon electrodes. Kinetic phenomena, *Journal of the American Chemical Society*, 102 (1980) 4231-4235.
- [121] M. Yoshimoto, Y. Miyazaki, M. Sato, K. Fukunaga, R. Kuboi, and K. Nakao, Mechanism for high stability of liposomal glucose oxidase to inhibitor hydrogen peroxide produced in prolonged glucose oxidation. *Bioconjugate chemistry* 15(5) (2004) 1055-1061.
- [122] I. Willner, E. Katz, F. Patolsky, A.F. Buckmann, Biofuel cell based on glucose oxidase and microperoxidase-11 monolayer-functionalized electrodes, *Journal of the Chemical Society - Perkin Transactions 2*, (1998) 1817-1822.
- [123] A. Pizzariello, M. Stred'ansky, S. Miertus, A glucose/hydrogen peroxide biofuel cell that uses oxidase and peroxidase as catalysts by composite bulk-modified bioelectrodes based on a solid binding matrix, *Bioelectrochemistry*, 56(1-2) (2002) 99-105.
- [124] A.I. Iaropolov, V. Malovik, S.D. Varfolomeev, I.V. Berezin, Electroreduction of hydrogen peroxides on the electrode with immobilized peroxidase, *Doklady Akademii Nauk Sssr*, 249 (1979) 1399–1401
- [125] E.E. Ferapontova, Direct Peroxidase Bioelectrocatalysis on a variety of electrode materials, *Electroanalysis*, 16 (2004) 1101-1112.
- [126] T. Ruzgas, L. Gorton, J. Emnéus, G. Marko-Varga, Kinetic models of horseradish peroxidase action on a graphite electrode, *Journal of Electroanalytical Chemistry*, 391 (1995) 41-49.
- [127] A. Lindgren, M. Tanaka, T. Ruzgas, L. Gorton, I. Gazaryan, K. Ishimori, I. Morishima, Direct electron transfer catalysed by recombinant forms of horseradish peroxidase: insight into the mechanism, *Electrochemistry Communications*, 1 (1999) 171-175.

- [128] R. Andreu, E.E. Ferapontova, L. Gorton, J.J. Calvente, Direct electron transfer kinetics in horseradish peroxidase electrocatalysis. *The Journal of Physical Chemistry B* 111 (2007) 469-477.
- [129] B.t. Limoges, J. Moiroux, J.-M. Savéant, Kinetic control by the substrate and the cosubstrate in electrochemically monitored redox enzymatic immobilized systems. Catalytic responses in cyclic voltammetry and steady state techniques, *Journal of Electroanalytical Chemistry*, 521(2002) 8-15
- [130] E.E. Ferapontova, L. Gorton, Effect of proton donors on direct electron transfer in the system gold electrode–horseradish peroxidase, *Electrochemistry Communications*, 3 (2001) 767-774.
- [131] L. Gorton, G. Bremle, E. Csöregi, G. Jönsson-Pettersson, B. Persson, Amperometric glucose sensors based on immobilized glucose-oxidizing enzymes and chemically modified electrodes, *Analytica Chimica Acta*, 249 (1991) 43-54.
- [132] M. Varnicic, K. Bettenbrock, D. Hermsdorf, T. Vidakovic-Koch, K. Sundmacher, Combined electrochemical and microscopic study of porous enzymatic electrodes with direct electron transfer mechanism, *RSC Advances*, 4 (2014) 36471-36479.
- [133] M. Secanell, K. Karan, A. Suleman, N. Djilali, Optimal design of ultralow-platinum PEMFC anode electrodes, *Journal of The Electrochemical Society*, 155 (2008) B125-B134.
- [134] P.K. Das, X. Li, Z.-S. Liu, Analytical approach to polymer electrolyte membrane fuel cell performance and optimization, *Journal of Electroanalytical Chemistry*, 604 (2007) 72-90.
- [135] P. Gode, F. Jaouen, G. Lindbergh, A. Lundblad, G. Sundholm, Influence of the composition on the structure and electrochemical characteristics of the PEFC cathode, *Electrochimica Acta*, 48 (2003) 4175-4187.
- [136] D. MacAodha, M.L. Ferrer, P.O. Conghaile, P. Kavanagh, D. Leech, Crosslinked redox polymer enzyme electrodes containing carbon nanotubes for high and stable glucose oxidation current, *Physical chemistry chemical physics : PCCP*, 14 (2012) 14667-14672.
- [137] A.N. Bashkatov, E.A. Genina, Y.P. Sinichkin, V.I. Kochubey, N.A. Lakodina, V.V. Tuchin, Glucose and mannitol diffusion in human dura mater, *Biophysical Journal*, 85 (2003) 3310-3318.
- [138] A.M. Bond, K. Bano, S. Adeel, L.L. Martin, J. Zhang, Fourier-transformed large-amplitude AC voltammetric study of tetrathiafulvalene (TTF): Electrode kinetics of the  $TTF^0/TTF^+$  and  $TTF^+/TTF^{2+}$  Processes, *ChemElectroChem*, 1 (2014) 99-107.
- [139] R. Wilson, A.P.F. Turner, Glucose oxidase - an ideal enzyme, *Biosensors & Bioelectronics*, 7(3) (1992) 165-185.
- [140] S. Rengaraj, P. Kavanagh, D. Leech. A comparison of redox polymer and enzyme co-immobilization on carbon electrodes to provide membrane-less glucose/O<sub>2</sub> enzymatic fuel cells with improved power output and stability, *Biosensors and Bioelectronics*, 30 (2011) 294-299.

- [141] N. Mano, F. Mao, A. Heller, Electro-oxidation of glucose at an increased current density at a reducing potential, *Chemical Communications*, (2004) 2116-2117.
- [142] G. Grampp, A. Kapturkiewicz, W. Jaenicke, Homogeneous and heterogeneous electron transfer rates of the tetrathiafulvalene-system, *Berichte der Bunsengesellschaft für physikalische Chemie*, 94 (1990) 439-447.
- [143] Y. Hayashi, I. Yamazaki, Oxidation-reduction potentials of compound-I-compound-II and compound-II-ferric couples of horseradish peroxidases A<sub>2</sub> and C, *Journal of Biological Chemistry*, 254 (1979) 9101-9106.
- [144] B. He, R. Sinclair, B.R. Copeland, R. Makino, L.S. Powers, I. Yamazaki, The structure-function relationship and reduction potentials of high oxidation states of myoglobin and peroxidase, *Biochemistry*, 35 (1996) 2413-2420.
- [145] Z. Temocin, M. Yigitoglu, Studies on the activity and stability of immobilized horseradish peroxidase on poly(ethylene terephthalate) grafted acrylamide fiber, *Bioprocess Biosyst Eng*, 32 (2009) 467-474.
- [146] T. Tatsuma, K. Ariyama, N. Oyama, . Kinetic analysis of electron transfer from a graphite coating to horseradish peroxidase, *Journal of Electroanalytical Chemistry*, 446 (1998) 205-209.
- [147] D. Jung, M. Paradiso, M. Hartmann, Formation of cross-linked glucose oxidase aggregates in mesocellular foams, *J Mater Sci*, 44 (2009) 6747-6753.
- [148] S.A.M. van Stroe-Biezen, F.M. Everaerts, L.J.J. Janssen, R.A. Tacke, Diffusion coefficients of oxygen, hydrogen peroxide and glucose in a hydrogel, *Analytica Chimica Acta*, 273 (1993) 553-560.
- [149] S.C. Barton, H.-H. Kim, G. Binyamin, Y. Zhang, A. Heller, Electroreduction of O<sub>2</sub> to water on the "Wired" laccase cathode, *The Journal of Physical Chemistry B*, 105 (2001) 11917-11921.
- [150] C. Gomez, S. Shipovskov, E.E. Ferapontova, Peroxidase biocathodes for a biofuel cell development, *Journal of Renewable and Sustainable Energy*, 2 (2010) 013103.
- [151] Pizzariello, M. Stred'ansky, S. Miertuš, A glucose/hydrogen peroxide biofuel cell that uses oxidase and peroxidase as catalysts by composite bulk-modified bioelectrodes based on a solid binding matrix, *Bioelectrochemistry*, 56 (2002) 99-105.
- [152] M. Delvaux, A. Walcarius, S. Demoustier-Champagne, Bienzyme HRP-GOx-modified gold nanoelectrodes for the sensitive amperometric detection of glucose at low overpotentials, *Biosensors and Bioelectronics*, 20 (2005) 1587-1594.
- [153] S. Tsujimura, Y. Kamitaka, K. Kano, Diffusion-controlled oxygen reduction on multi-copper oxidase-adsorbed carbon aerogel electrodes without mediator, *Fuel Cells*, 7 (2007) 463-469.
- [154] Li, X., Zhang, L., Su, L., Ohsaka, T., Mao, L., A miniature glucose/O<sub>2</sub> biofuel cell with a high tolerance against ascorbic acid, *Fuel Cells*, 9(1) (2009) 85-91.

- [155] A.N. Bashkatov, E.A. Genina, Y.P. Sinichkin, V.I. Kochubey, N.A. Lakodina, V.V. Tuchin  
Glucose and mannitol diffusion in human dura mater. *Biophys. J.*, 85 (2003) 3310–3318.
- [156] I. Dencic, et al., From a Review of Noble Metal versus Enzyme Catalysts for Glucose  
Oxidation Under Conventional Conditions Towards a Process Design Analysis for  
Continuous-flow Operation. *Journal of Flow Chemistry*, 1(1) (2011)13-23.
- [157] D.Y. Murzin, and R. Leino, Sustainable chemical technology through catalytic multistep  
reactions. *Chemical Engineering Research & Design*, 86(9A) (2008) 1002-1010.
- [158] Y. Holade, et al., Highly Selective Oxidation of Carbohydrates in an Efficient  
Electrochemical Energy Converter: Cogenerating Organic Electrosynthesis. *Chemsuschem*,  
2016 9(3) 252-263.
- [159] H.G.J. Dewilt, Part I Oxidation of glucose to gluconic acid: survey of techniques. *Industrial  
& Engineering Chemistry Product Research and Development*, 11(4) (1972) 370-373.
- [160] S. Velizarov, and V. Beschkov, Biotransformation of glucose to free gluconic acid by  
*Gluconobacter oxydans*: substrate and product inhibition situations. *Process  
Biochemistry*, 33(5) (1998) 527-534.

## Appendix 1: Derivation of the reduced 1-D model

Balances	Model reduction step
For the electron-conducting phase	$0 = \int_{z=0}^{z=L} \frac{\partial}{\partial z} \left( \kappa_E^{CL} \frac{\partial \phi_E^{CL}(z,t)}{\partial z} \right) dz + \int_{z=0}^{z=L} a \iota(z,t) dz \quad \text{A1.1}$
	$0 = \kappa_E^{CL} \frac{\partial \phi_E^{CL}(t)}{\partial z} \Big _{z=L} - \kappa_E^{CL} \frac{\partial \phi_E^{CL}(t)}{\partial z} \Big _{z=0} + a \iota(t)L \quad \text{A1.2}$
	<p>Applying a boundary condition (Eq. (10)) and simplifying further, we obtain</p> $0 = -\kappa_E^{CL} \frac{\phi_E^{CL}(t) - \phi_E^{LB}(t)}{L/2} + j(t) \quad \text{A1.3}$
For the ion conducting phase	$0 = \int_{z=0}^{z=L} \frac{\partial}{\partial z} \left( \kappa_I^{CL} \frac{\partial \phi_I^{CL}(z,t)}{\partial z} \right) dz - \int_{z=0}^{z=L} a \iota(z,t) dz \quad \text{A1.4}$
	$0 = \kappa_I^{CL} \frac{\partial \phi_I^{CL}(z,t)}{\partial z} \Big _{z=L} - \kappa_I^{CL} \frac{\partial \phi_I^{CL}(z,t)}{\partial z} \Big _{z=0} - a \iota(z,t)L \quad \text{A1.5}$
	<p>Applying boundary condition (Eq. (13)) and having further simplification, one can get</p> $0 = \kappa_I^{CL} \frac{\phi_I^{RB}(t) - \phi_I^{CL}(t)}{L/2} - j(t) \quad \text{A1.6}$
At the interface	$C_{dl} \frac{dE(t)}{dt} aL = -j(t) + nFr_e aL \quad \text{A1.7}$
Mass balance	<p>The mass balance of substance <math>\alpha</math> in the CL</p> $\int_{z=0}^{z=L} \varepsilon \frac{\partial C_\alpha^{CL}(z,t)}{\partial t} dz = \int_{z=0}^{z=L} \frac{\partial}{\partial z} \left( D_\alpha^{CL} \frac{\partial C_\alpha^{CL}(z,t)}{\partial z} \right) dz + \int_{z=0}^{z=L} a \sum_k \nu_{\alpha,k} r_k(z,t) dz \quad \text{A1.8}$
	$\varepsilon \frac{\partial C_\alpha^{CL}(t)}{\partial t} L = D_\alpha^{CL} \frac{\partial C_\alpha^{CL}(t)}{\partial z} \Big _{z=L} - D_\alpha^{CL} \frac{\partial C_\alpha^{CL}(t)}{\partial z} \Big _{z=0} + aL \sum_k \nu_{\alpha,k} r_k(t) \quad \text{A1.9}$
	<p>Applying the boundary condition (Eq. (32)) and making a further simplification</p> $\frac{dC_\alpha^{CL}(t)}{dt} L = D_\alpha^{CL} \frac{C_\alpha^{RB}(t) - C_\alpha^{CL}(t)}{L/2} - aL \sum_k \nu_{\alpha,k} r_k(t) \quad \text{A1.10}$

## Appendix 2: Derivation of steady state expressions of the interface model

- Derivation of Eq. (190) and Eq. (191)

The mass balance for CPI is defined as

$$\frac{d\Gamma_{CPI}(0,t)}{dt} = k_1 C_{S1}(0,t) \Gamma_{E1red}(0,t) - |r_{e1}(0,t)| \quad A2. 1$$

And at pseudo steady state (ss)

$$\frac{d\Gamma_{CPI}(0,t)}{dt} = 0 \quad A2. 2$$

Therefore, the concentration of the reduced form of enzyme is expressed as

$$\Gamma_{E1red,ss} = \frac{|r_{e1,ss}|}{k_1 C_{S1,ss}} \quad A2. 3$$

and the balancing for CPII is

$$\frac{d\Gamma_{CPII}(0,t)}{dt} = |r_{e1}(0,t)| - |r_{e2}(0,t)| \quad A2. 4$$

At the pseudo steady state, the reaction rates of the two electrochemical steps are equal.

$$r_{e1,ss} = r_{e2,ss} \quad A2. 5$$

$$k_{e1} e^{\left(-\frac{\alpha_1 F}{RT} \eta_1\right)} \Gamma_{CPI,ss} C_{H^+,ss} = k_{e2} e^{\left(-\frac{\alpha_2 F}{RT} \eta_2\right)} \Gamma_{CPII,ss} C_{H^+,ss} \quad A2. 6$$

Assuming only one effective over-potential  $\eta_1 = \eta_2 = \eta_{SS}$  and  $\alpha_1 = \alpha_2 = \alpha$

$$\Gamma_{CPII,ss} = \frac{k_{e1}}{k_{e2}} \Gamma_{CPI,ss} \quad A2. 7$$

the total electrochemical reaction rate is defined as

$$|r_e(0,t)| = |r_{e1}(0,t)| + |r_{e2}(0,t)| \quad A2. 8$$

At steady state condition, we get

$$|r_{e,ss}| = |r_{e1,ss}| + |r_{e2,ss}| = k_{e1} e^{\left(-\frac{\alpha F}{RT} \eta_{ss}\right)} \Gamma_{CPI,ss} C_{H^+,ss} + k_{e2} e^{\left(-\frac{\alpha F}{RT} \eta_{ss}\right)} \Gamma_{CPII,ss} C_{H^+,ss} \quad A2. 9$$

$$|r_{e,ss}| = k_{e1} e^{\left(-\frac{\alpha F}{RT} \eta_{ss}\right)} \Gamma_{CPI,ss} C_{H^+,ss} + k_{e2} e^{\left(-\frac{\alpha F}{RT} \eta_{ss}\right)} \frac{k_{e1}}{k_{e2}} \Gamma_{CPI,ss} C_{H^+,ss} \quad A2. 10$$

$$|r_{e,ss}| = 2k_{e1} \Gamma_{CPI,ss} C_{H^+,ss} e^{\left(-\frac{\alpha F}{RT} \eta_{ss}\right)} \quad A2. 11$$

The total concentration of enzyme is conservative

$$\Gamma_t = \Gamma_{CPI,ss} + \frac{k_{e1}}{k_{e2}} \Gamma_{CPI,ss} + \Gamma_{Ered,ss} = \left(\frac{k_{e2} + k_{e1}}{k_{e2}}\right) \Gamma_{CPI,ss} + \Gamma_{Ered,ss} \quad A2. 12$$

$$\Gamma_{CPI,ss} = \left(\Gamma_t - \Gamma_{Ered,ss}\right) \frac{k_{e2}}{k_{e2} + k_{e1}} \quad A2. 13$$

Replacing Eq. (A2.13) in to Eq. (A2.11)

$$|r_{e,ss}| = 2 \frac{k_{e2}k_{e1}}{k_{e2}+k_{e1}} \left( \Gamma_t - \frac{|r_{e1,ss}|}{k_1 C_{S1,ss}} \right) C_{H^+,ss} e^{\left( -\frac{\alpha F}{RT} \eta_{ss} \right)} \quad \text{A2. 14}$$

$$|r_{e,ss}| = 2 \frac{k_{e2}k_{e1}}{k_{e2}+k_{e1}} \left( \Gamma_t - \Gamma_{Ered,ss} \right) C_{H^+,ss} e^{\left( -\frac{\alpha F}{RT} \eta_{ss} \right)} \quad \text{A2. 15}$$

$$|r_{e,ss}| = 2 \frac{k_{e2}k_{e1}}{k_{e2}+k_{e1}} \Gamma_t C_{H^+} e^{\left( -\frac{\alpha F}{RT} \eta_{ss} \right)} - 2 \frac{k_{e2}k_{e1}}{k_{e2}+k_{e1}} \frac{|r_{e,ss}|}{2k_1 C_{S1,ss}} C_{H^+,ss} e^{\left( -\frac{\alpha F}{RT} \eta_{ss} \right)} \quad \text{A2. 16}$$

$$\text{With } k_e = \frac{k_{e2}k_{e1}}{k_{e2}+k_{e1}} \quad \text{A2. 17}$$

$$|r_{e,ss}| k_1 C_{S1,ss} + k_e |r_{e,ss}| C_{H^+,ss} e^{\left( -\frac{\alpha F}{RT} \eta_{ss} \right)} = 2k_e \Gamma_t C_{H^+} + k_1 C_{S1,ss} e^{\left( -\frac{\alpha F}{RT} \eta_{ss} \right)} \quad \text{A2. 18}$$

$$|r_{e,ss}| \left( k_1 C_{S1,ss} + k_e C_{H^+,ss} e^{\left( -\frac{\alpha F}{RT} \eta_{ss} \right)} \right) = 2k_1 k_e \Gamma_t C_{H^+} C_{S1,ss} e^{\left( -\frac{\alpha F}{RT} \eta_{ss} \right)} \quad \text{A2. 19}$$

$$|r_{e,ss}| = \frac{2k_1 k_e \Gamma_t C_{H^+} C_{S1,ss} e^{\left( -\frac{\alpha F}{RT} \eta_{ss} \right)}}{k_1 C_{S1,ss} + k_e C_{H^+,ss} e^{\left( -\frac{\alpha F}{RT} \eta_{ss} \right)}} \quad \text{A2. 20}$$

For the cathodic electrochemical, the reaction rate at the interface is

$$r_{e,ss}(0, \eta_{ss}) = - \frac{2k_1 \Gamma_t C_{H^+,ss}(0, \eta_{ss}) C_{S1,ss}(0, \eta_{ss}) k_e e^{\left( -\frac{\alpha F}{RT} \eta_{ss} \right)}}{k_1 C_{S1,ss}(0, \eta_{ss}) + k_e e^{\left( -\frac{\alpha F}{RT} \eta_{ss} \right)} C_{H^+,ss}(0, \eta_{ss})} \quad \text{A2. 21}$$

- **Derivation of Eq. (213)**

The mass balance for the enzyme substrate (ES) complex is defined as

$$\frac{dC_{E1S1}(0,t)}{dt} = k_1 C_{S1}(0,t) \Gamma_{E1red}(0,t) - k_{-1} C_{E1S1}(0,t) - k_{cat} C_{E1S1}(0,t) \quad \text{A2. 22}$$

At pseudo steady state condition, one can get

$$k_1 C_{S1,ss} \Gamma_{E1red,ss} - k_{-1} C_{E1S1,ss} - k_{cat} C_{E1S1,ss} = 0 \quad \text{A2. 23}$$

$$\Gamma_{E1red,ss} = \frac{(k_{-1} + k_{cat}) C_{E1S1,ss}}{k_1 C_{S1,ss}} = K_m \frac{C_{E1S1,ss}}{C_{S1,ss}} \quad \text{A2. 24}$$

where

$$K_m = \frac{(k_{-1} + k_{cat})}{k_1} \quad \text{A2. 25}$$

The balance for CPI is

$$\frac{dC_{CPI}(0,t)}{dt} = k_{cat} C_{E1S1}(0,t) - |r_{e1,ss}(0,t)| \quad \text{A2. 26}$$

At steady state condition, Eq. (A2.26) becomes:

$$k_{cat} C_{E1S1} - |r_{e1,ss}| = 0 \quad \text{A2. 27}$$

$$C_{E1S1} = \frac{|r_{e1,ss}|}{k_{cat}} = \frac{|r_{e,ss}|}{2k_{cat}} \quad \text{A2. 28}$$

Inserting Eq. (A2.28) in to Eq. (A2.24), one can get

$$\Gamma_{E1red,ss} = \frac{(k_{-1} + k_{cat}) C_{ES,ss}}{k_1 C_{S1,ss}} = K_m \frac{|r_{e1,ss}|}{C_{S1,ss} k_{cat}} = K_m \frac{|r_{e,ss}|}{2C_{S1,ss} k_{cat}} \quad \text{A2. 29}$$

For CPlI, similar steps follow from Eq. (A2.29) to Eq. (A2.26)

$$\frac{d\Gamma_{CPlI}(0,t)}{dt} = |r_{e1}(0,t)| - |r_{e2}(0,t)| \quad \text{A2. 30}$$

$$|r_{e,ss}| = 2k_{e1}\Gamma_{CPl,ss}C_{H^+,ss}e^{\left(-\frac{\alpha}{RT}\eta_{ss}\right)} \quad \text{A2. 31}$$

The total concentration of enzyme is conservative

$$\Gamma_t = \Gamma_{CPl,ss} + \Gamma_{CPlI,ss} + \Gamma_{ES,ss} + \Gamma_{Ered,ss} = \Gamma_{CPl,ss} + K_m \frac{|r_{e,ss}|}{2C_{S1,ss}k_{cat}} + \frac{|r_{e,ss}|}{2k_{cat}} \quad \text{A2. 32}$$

$$\Gamma_{CPl,ss} = \Gamma_t - K_m \frac{|r_{e,ss}|}{2C_{S1,ss}k_{cat}} - \frac{|r_{e,ss}|}{2k_{cat}} \quad \text{A2. 33}$$

Replacing Eq. (A2.33) to Eq. (A2.31), one gets

$$|r_{e,ss}| = k_{e1}\Gamma_{CPl,ss}C_{H^+,ss} \left( \Gamma_t - K_m \frac{|r_{e,ss}|}{2C_{S1,ss}k_{cat}} - \frac{|r_{e,ss}|}{2k_{cat}} \right) e^{\left(-\frac{\alpha}{RT}\eta_{ss}\right)} \quad \text{A2. 34}$$

With rearrangement, we get

$$|r_{e,ss}| = \frac{2k_{cat}\Gamma_t C_{H^+,ss} C_{S1,ss} k_e e^{\left(-\frac{\alpha F}{RT}\eta_{ss}\right)}}{k_{cat} C_{S1,ss} + k_e e^{\left(-\frac{\alpha F}{RT}\eta_{ss}\right)} C_{S1,ss} C_{H^+,ss} + K_m k_e e^{\left(-\frac{\alpha F}{RT}\eta_{ss}\right)} C_{H^+,ss}} \quad \text{A2. 35}$$

The cathodic electrochemical reaction rate is

$$r_{e,ss} = - \frac{2k_{cat}\Gamma_t C_{H^+,ss} C_{S1,ss} k_e e^{\left(-\frac{\alpha F}{RT}\eta_{ss}\right)}}{k_{cat} C_{S1,ss} + k_e e^{\left(-\frac{\alpha F}{RT}\eta_{ss}\right)} C_{S1,ss} C_{H^+,ss} + K_m k_e e^{\left(-\frac{\alpha F}{RT}\eta_{ss}\right)} C_{H^+,ss}} \quad \text{A2. 36}$$



## Appendix 3: The derivation of electrochemical impedance spectroscopy of Model 3

The EIS model is defined in section 3.1.4.2; here, a detailed approximation is presented for  $M_3$ . The other two simpler models ( $M_1$ ,  $M_2$ ) should follow in the same logic.

The input potential definition applied for the cathode is

$$\Delta E_{input}(0, t) = E_{input}(0, t) - E_{input,ss} = A \cos \omega t = \frac{A}{2} (e^{i\omega t} + e^{-i\omega t}) \quad A2. 37$$

$$\Delta j(0, t) = j(0, t) - j_{ss}(0, t) = \frac{A}{2} (H_1(\omega) e^{i\omega t} + H_1(-\omega) e^{-i\omega t}) + \left(\frac{A}{2}\right)^2 H_2(\omega, \omega) e^{2i\omega t} + \dots \quad A2. 38$$

$$E(0, t) = \frac{A}{2} (H_{1,E}(\omega) e^{i\omega t} + H_{1,E}(-\omega) e^{-i\omega t}) + \left(\frac{A}{2}\right)^2 H_{2,E}(\omega, \omega) e^{2i\omega t} + \dots \quad A2. 39$$

$$\Delta \Gamma_{E1S1}(0, t) = \frac{A}{2} (H_{1,E1S1}(\omega) e^{i\omega t} + H_{1,E1S1}(-\omega) e^{-i\omega t}) + \left(\frac{A}{2}\right)^2 H_{2,E1S1}(\omega, \omega) e^{2i\omega t} + \dots \quad A2. 40$$

$$\Delta \Gamma_{E1red}(0, t) = \frac{A}{2} (H_{1,E1red}(\omega) e^{i\omega t} + H_{1,E1red}(-\omega) e^{-i\omega t}) + \left(\frac{A}{2}\right)^2 H_{2,E1red}(\omega, \omega) e^{2i\omega t} + \dots \quad A2. 41$$

$$\Delta \Gamma_{CPI}(0, t) = \frac{A}{2} (H_{1,CPI}(\omega) e^{i\omega t} + H_{1,CPI}(-\omega) e^{-i\omega t}) + \left(\frac{A}{2}\right)^2 H_{2,CPI}(\omega, \omega) e^{2i\omega t} + \dots \quad A2. 42$$

$$\Delta \Gamma_{CPII}(0, t) = \frac{A}{2} (H_{1,CPII}(\omega) e^{i\omega t} + H_{1,CPII}(-\omega) e^{-i\omega t}) + \left(\frac{A}{2}\right)^2 H_{2,CPII}(\omega, \omega) e^{2i\omega t} + \dots \quad A2. 43$$

$$\Delta \Gamma_{S1}(0, t) = \frac{A}{2} (H_{1,S1}(\omega) e^{i\omega t} + H_{1,S1}(-\omega) e^{-i\omega t}) + \left(\frac{A}{2}\right)^2 H_{2,S1}(\omega, \omega) e^{2i\omega t} + \dots \quad A2. 44$$

$$\Delta \Gamma_{H^+}(0, t) = \frac{A}{2} (H_{1,H^+}(\omega) e^{i\omega t} + H_{1,H^+}(-\omega) e^{-i\omega t}) + \left(\frac{A}{2}\right)^2 H_{2,H^+}(\omega, \omega) e^{2i\omega t} + \dots \quad A2. 45$$

where  $H_1(\omega)$ ,  $H_{1,E}(\omega)$ ,  $H_{1,S1}(\omega)$ ,  $H_{1,CPI}(\omega)$ ,  $H_{1,CPII}(\omega)$ ,  $H_{1,H^+}(\omega)$ ,  $H_{1,E1S1}(\omega)$ , and  $H_{1,E1red}(\omega)$  are the 1<sup>st</sup> order auxiliary FRFs, while  $H_{2,E}(\omega, \omega)$ ,  $H_{1,S1}(\omega, \omega)$ ,  $H_{2,CPI}(\omega, \omega)$ ,  $H_{2,CPII}(\omega, \omega)$ ,  $H_{2,H^+}(\omega, \omega)$ ,  $H_{2,E1S1}(\omega, \omega)$ , and  $H_{2,E1red}(\omega, \omega)$  are the second order auxiliary FRFs, and so on.

### Taylor approximation of the non-linear terms

In this step, all the terms in the electrochemical reaction rate are expressed in a polynomial form by applying Taylor expansion. Generally, if the output is analyzed up to  $n^{\text{th}}$  order FRFs, then in the Taylor series the terms up to  $n^{\text{th}}$  order need to be taken into consideration. In this study, we derive the 1<sup>st</sup> FRF, and therefore it is sufficient to write only the terms up to the 1<sup>st</sup> order. Substituting the Taylor approximation into all the reaction rates and BCs, one can obtain:

- For the electrochemical reaction rate

$$\begin{aligned} \Delta r_e(0, t) = & \underbrace{\left. \frac{\partial r_{1e}(0, t)}{\partial \Gamma_{CPI}} \right]_{SS}}_{P_1} \Delta \Gamma_{CPI}(0, t) + \underbrace{\left. \frac{\partial r_{1e}(0, t)}{\partial C_{H^+}} \right]_{SS}}_{P_2} \Delta C_{H^+}(0, t) + \underbrace{\left. \frac{\partial r_{1e}(0, t)}{\partial E} \right]_{SS}}_{P_3} \Delta E(0, t) + \\ & \underbrace{\left. \frac{\partial r_{2e}(0, t)}{\partial \Gamma_{CPII}} \right]_{SS}}_{P_4} \Delta \Gamma_{CPII}(0, t) + \dots \end{aligned} \quad \text{A2. 46}$$

- For the boundary conditions for proton  $H^+$

$$D_{H^+} \left. \frac{\partial C_{H^+}(z, t)}{\partial z} \right|_{z=0} = \Delta r_{1e}(0, t) + \Delta r_{2e}(0, t) \quad \text{A2. 47}$$

$$D_{H^+} \left. \frac{\partial C_{H^+}(z, t)}{\partial z} \right|_{z=0} = P_1 \Delta \Gamma_{CPI}(0, t) + P_2 \Delta C_{H^+}(0, t) + P_3 \Delta E(0, t) + P_4 \Delta \Gamma_{CPII}(0, t) + \dots \quad \text{A2. 48}$$

- For the charge balance

$$C_{dl} \left. \frac{dE(0, t)}{dt} \right|_{z=0} = i(t) - F P_1 \Delta \Gamma_{CPI}(0, t) + P_2 \Delta C_{H^+}(0, t) + P_3 \Delta E(0, t) + P_4 \Delta \Gamma_{CPII}(0, t) + \dots \quad \text{A2. 49}$$

The next step is the substitution of the inputs and outputs and application of the method of harmonic probing.

- For the substrate mass balance

$$\left. \frac{\partial^2 (H_{1,S1}(z, \omega))}{\partial z^2} \right|_{z=0} - \frac{i\omega}{D_S} H_{1,S1}(0, \omega) = 0 \quad \text{A2. 50}$$

With boundary conditions

$$\left. \frac{\partial (H_{1,S1}(z, \omega))}{\partial z} \right|_{z=0} = k_1 \Gamma_{E1red,ss} H_{1,S1}(\omega) + k_1 C_{S1,ss} H_{1,E1red}(\omega) - k_{-1} H_{1,E1S1}(\omega) \quad \text{A2. 51}$$

And

$$H_{1,S1}(\delta_{D,S}, \omega) = 0 \quad \text{A2. 52}$$

The solution to the equation system (Eq. (A2. 50) to (A2. 52)) is

$$H_{1,S1}(\omega) = T_1 H_{1E1red} + T_2 H_{1E1S1} \quad \text{A2. 53}$$

- For proton  $H^+$  mass balance

$$D_{H^+} \frac{\partial^2 (H_{1,H^+}(z,\omega))}{\partial z^2} - (k_{a-1}C_{A^-} + i\omega)H_{1,H^+}(z,\omega) = 0 \quad A2. 54$$

- With boundary condition

$$D_{H^+} \frac{\partial (H_{1,H^+}(z,\omega))}{\partial z} \Big|_{z=0} = P_1 H_{1,CPI}(\omega) + P_2 H_{1,H^+}(\omega) + P_3 H_{1,E}(\omega) + P_4 H_{1,CPII}(\omega) + \dots \quad A2. 55$$

And

$$H_{1,H^+}(\delta_{D,H^+}, \omega) = 0 \quad A2. 56$$

The solution to equation system from Eq. (A2.54) to Eq. (A2.56) is

$$H_{1,H^+}(\omega)(1 - T_3 P_2) - T_3 P_1 H_{1,CPI}(\omega) - T_3 P_3 H_{1,E}(\omega) - T_3 P_4 H_{1,CPI}(\omega) = 0 \quad A2. 57$$

- For the charge balance

$$H_1(\omega) = (C_{dl}i\omega - FP_3)H_{1,E}(\omega) - xF \left( P_1 H_{1,CPI}(\omega) + P_2 H_{1,H^+}(\omega) + P_4 H_{1,CPII}(\omega) \right) \quad A2. 58$$

- For the input potential

$$H_{1,E}(\omega) = 1 - S_a R_\Omega H_1(\omega) \quad A2. 59$$

- For the total surface concentration of the enzyme

$$H_{1,CPI}(\omega) + H_{1,E1red}(\omega) + H_{1,E1S1}(\omega) + H_{1,CPII}(\omega) = 0 \quad A2. 60$$

- For the intermediate compound (CPII) of electrochemical step

$$H_{1,CPII}(\omega) = \frac{P_1}{i\omega + P_4} H_{1,CPI}(\omega) \quad A2. 61$$

- For the oxidized form of enzyme from CPI

$$H_{1,CPI}(\omega)(i\omega + P_1) + \frac{P_2}{2} H_{1,H^+}(\omega) + \frac{P_3}{2} H_{1,E}(\omega) - k_{cat} H_{1,E1S1}(\omega) = 0 \quad A2. 62$$

- For the enzyme substrate complex

$$(i\omega + k_{-1} + k_{cat})H_{1,E1S1}(\omega) = k_1 C_{S1,ss} H_{1,E1red}(\omega) + k_1 C_{E1red,ss} H_{1,S1}(\omega) \quad A2. 63$$

Solving the system of Eq. (A2. 53) and Eqs. (A2. 57-A2. 63), the expression of  $H_1(\omega)$  of  $M_3$  can

be obtained as follows

$$H_1(\omega) = \frac{2FR_4 R_1 - R_3 C_{dl} i \omega}{2F(R_4 R_2 - R_3 R_5)} \quad A2. 64$$

In which all the abbreviations are listed in table A2. 2.

Table A2. 1: Expression of coefficients and related groups appearing in electrochemical admittance  $H_1(\omega)$

Group	Expression
R <sub>1</sub>	$\frac{C_{dl}i\omega - FP_3}{P_2F} [1 - T_3P_2] - T_3P_3$
R <sub>2</sub>	$\frac{1 + (C_{dl}i\omega - FP_3)S_aR_{\Omega}}{P_2F} [1 - T_3P_2] - T_3P_3S_aR_{\Omega}$
R <sub>3</sub>	$-\frac{P_1i\omega + 2P_4P_1}{P_2(i\omega + P_4)}$
R <sub>4</sub>	$\frac{i\omega(i\omega + P_4 + \frac{P_1}{2})S_aR_{\Omega}}{(i\omega + P_4)} + \frac{k_{cat}(i\omega + P_4 + P_1)(C_{S1,SS} + \Gamma_{Ered1,SS}T_1)}{(\frac{i\omega}{k_1} + K_m - \Gamma_{Ered1,SS}(T_2 - T_1) + C_{S1,SS})(i\omega + P_4)}$
R <sub>5</sub>	$\frac{1 + S_aR_{\Omega}C_{dl}i\omega}{2F}$
P <sub>1</sub>	$-k_{e1}e^{\left(-\frac{\alpha_1F}{RT}(E_{SS}-E_{r1})\right)}C_{H+,SS}$
P <sub>2</sub>	$-k_{e1}e^{\left(-\frac{\alpha_1F}{RT}(E_{SS}-E_{r1})\right)}C_{CPI,SS}$
P <sub>3</sub>	$k_{e1}\frac{\alpha_1F}{RT}e^{\left(-\frac{\alpha_1F}{RT}(E_{SS}-E_{r1})\right)}C_{CPI,SS}C_{H+,SS}$
P <sub>4</sub>	$-k_{e2}e^{\left(-\frac{\alpha_2F}{RT}(E_{SS}-E_{r2})\right)}C_{H+,SS}$
P <sub>5</sub>	$-k_{e2}e^{\left(-\frac{\alpha_2F}{RT}(E_{SS}-E_{r2})\right)}C_{CPII,SS}$
P <sub>6</sub>	$k_{e2}\frac{\alpha_2F}{RT}e^{\left(-\frac{\alpha_2F}{RT}(E_{SS}-E_{r2})\right)}C_{CPII,SS}C_{H+,SS}$
T <sub>1</sub>	$\frac{-\tanh(a_1\delta_{D,red}\sqrt{\omega})k_1C_{S1,SS}}{a_1D_{S1}\sqrt{\omega} + \tanh(a_1\delta_{D,red}\sqrt{\omega})k_1\Gamma_{E1red,SS}}$
T <sub>2</sub>	$\frac{\tanh(a_1\delta_{D,red}\sqrt{\omega})k_{-1}}{a_1D_{S1}\sqrt{\omega} + \tanh(a_1\delta_{D,red}\sqrt{\omega})k_1\Gamma_{E1red,SS}}$
T <sub>3</sub>	$\frac{-\tanh(a_2\delta_{D,H+})}{D_{H+}a_2}$
$\alpha_1$	$\sqrt{\frac{i}{D_{S1}}}$
$\alpha_2$	$\sqrt{\frac{k_{-a1}C_{A-} + i\omega}{D_{H+}}}$

-The end-